Development and characterization of sensors for human health

Doctoral Dissertation
Doctoral Program in Metrology (32^{nd} cycle)

Development and characterization of sensors for human health

Luca Lombardo
* * * * * *

Supervisors
Prof. Marco Parvis, Supervisor
Prof. Sabrina Grassini, Cosupervisor

Doctoral Examination Committee:
Prof. Anna Maria Lucia Lanzolla, Referee, Politecnico di Bari
Prof. Panayota Vassiliou, Referee, National Technical University of Athens

Politecnico di Torino
December 17, 2019

I hereby declare that, the contents and organization of this dissertation constitute my own original work and does not compromise in any way the rights of third parties, including those relating to the security of personal data.

. . . . . .

Luca Lombardo
Turin, December 17, 2019

Summary

This thesis focuses on the development of sensors for human health. Several different factors impacts people live and health. Among them surely pollution and health care are extremely important.

First part of the thesis deals with the pollution topic and, in particular with the atmospheric particulate matter. Atmospheric pollution due to the particulate is nowadays a serious issue and it turns out in severe effects on human health. Many studies demonstrated the correlation between high aerosol concentrations and the presence of several diseases in the exposed subjects. Transitory diseases of respiratory system, such as bronchitis, asthma and inflammations, are very common even though lung cancer and cardiovascular problems were registered as well. Atmospheric particulate is also correlated with different negative consequences on climate. Among them, the most worrying one is surely the direct climate forcing due to the high light absorption coefficient of the particulate and, consequently, the increasing of local atmospheric temperature. This has significant secondary effects on cloud formation and on wet precipitations as well.

The effects of atmospheric particulate matter are related to several properties of the particles, such as size, chemical composition and morphology. Such characteristics can largely change according to aerosol source and environment conditions. Therefore, a suitable monitoring of the concentration of particulate matter is mandatory both for assuring safe life conditions to people and to better understand the processes involved in formation, transformation and deposition of aerosols.

Unfortunately, available monitoring devices employs detection approaches which provide only a partial characterization of the aerosol. Furthermore, they are typically very expensive and not suitable to be employed in a capillary monitoring of the territory. This turns out in the necessity of developing small low-cost monitoring nodes to be employed in smart wireless sensor networks. With this aim, a new detection approach based on a small digital camera able to detect the single particles captured on a standard glass fibre filter was developed. Three different prototypes, employing such an approach but differing in filter management, were realized and characterized with several tests. In particular, preliminary tests were carried out to assess the feasibility of the proposed approach and the characteristics of the air pumping system employed to sample a specified volume of air and the effective resolution achieved by the camera optical system. Further characterizations were carried out to investigate the blocking

capability of the selected filters and the principal properties of the captured particles. Eventually, a comparison of the proposed system towards a commercial laser-scattering station was carried out. The results achieved are very promising even though a significant difference is still present between the two instruments.

Second part of the thesis, instead, deals with health care and the employment of breath analysis as alternative to conventional diagnostic methods. Breath analysis is based on the detection of specific gaseous species, called biomarkers, in exhaled breath. Such biomarkers, when present at abnormal concentrations, are indicative of specific diseases.

Breath analysis has several advantages such as non-invasiveness, quick response and virtually low-cost. Unfortunately, still nowadays, there are many limitations to an effective employment of such a technique. In particular, biomarkers are present in human breath at extremely low concentration. Furthermore, being the exhaled breath a complex mixture as several different gaseous species is very difficult to distinguish between them and accurately detect specific biomarkers. Therefore, high sensitivity and selectivity are required features of any device employed in breath analysis. This turns out in expensive equipment which partially deprives the advantages of such a method. A possible solution to such issues is the employment of cheap and small gas sensors able to achieve suitable sensitivity and selectivity.

In such a framework, several conductometric gas sensors based on thin film of niobium oxide were deposited on small alumina substrates by using reactive magnetron sputtering deposition in a RF capacitively-coupled parallel-plate plasma reactor. Several different combinations of deposition parameters were tested and many sensor prototypes were realized and fully characterized with the aim to develop effective sensors for acetone, a recognized biomarker of diabetes.

Preliminary characterization were performed in order to assess film structure and morphology by means of an electron scanning microscope. Subsequently, the chemical composition of deposited films was investigated employing the x-ray photo-electron spectroscopy which revealed a deposited film mainly composed by Nb_2O_5.

Sensing performance of prototypes were investigated and compared in order to find the optimal deposition parameters. Dedicated tests were carried out with an experimental measurement setup in order to assess sensitivity, selectivity, stability and response times of the realized prototypes. In particular, one of them revealed good sensitivity suitable for detecting acetone at concentrations lower than 1 ppm. Quick response times and an excellent selectivity were assessed as well.

Such sensing performance together with a low-cost and a low power consumption pave the way for the development of small breath analyzers able to non-invasively monitoring diabetes patients by means of an effortless sampling of exhaled breath.

Acknowledgements

The author thanks Prof. Carmine Lubritto of Università della Campania, and Dr. A. Spagnuolo, Dr. C. Vetromile and Dr. A. Maisello of ENERGREENUP for the possibility to access the commercial laser-scattering station employed during the characterization of the particulate monitoring system and for their support during the measurement campaign carried out in the city of Caserta.

The author also thanks Prof. N. Donato, Prof. G. Neri and Dr. K. Moulaee of University of Messina for their invaluable support during the development and the characterization of the conductometric gas sensors for acetone.

Contents

List of Tables

List of Figures

Chapter 1

Introduction

This chapter partially contains materials from previously published works of the author [1–5]

Since ancient times people all around the world put efforts to improve quality and duration of their life. Among the factors that more affects life and human health, there are surely environmental conditions and medical care. The significant improvements achieved till now have been mainly due to scientific and social progress, and to the development of innovative technologies. Many diseases, which were a serious limit to human life until few years ago, can now be healed or kept under control thanks to the introduction of new effective medical treatments and drugs, and to the development of early diagnostic methods. Several are sources or causes of diseases or sickness for the human beings, among these environment and life conditions are of primary importance.

The work described in this thesis focus on two aspects related to health improvement: environmental monitoring of atmospheric pollution and non-invasive diagnosis by the breath-analysis method.

In particular, a monitoring system for the atmospheric particulate matter based on a novel optical approach and of high-performance conductometric sensors for the assessment of the acetone level in the human breath have been designed and characterized by comparing their output with other commercial systems.

This first chapter is an introduction on the topic. Moreover, a short description of the proposed particulate monitoring system and the gas sensor is provided together with a summary of the achieved results. Chapter 2 provides a much more detailed material on the pollution related with the atmospheric particulate matter and on the most frequently employed equipment and measurement methodologies. The proposed monitoring system is described in details in chapter 3, where are also reported the test performed for validating the proposed system and the achieved results.

Similarly, chapters 4 and 5 deal with the breath-analysis and the realized acetone gas sensors providing details on the film deposition, chemical characterization and achieved performance.

1.1 A novel approach for monitoring the atmospheric particulate matter

Nowadays, one of the most critical problems connected with pollution is the atmospheric particulate matter. The particulate is a mixture of small solid and liquid particles suspended in the atmosphere which derives both from natural and anthropogenic activities. The particles have very different sizes ranging from few nanometer to hundreds of micrometers and they are characterized by several different properties (composition, shape, surface morphology, etc.) from which depend the lifetime and the effects of the particulate itself. The particulate chemical composition is very heterogeneous including mineral dust, inorganic salts, carbonaceous and organic compounds [6–9]. Particulate matter, or aerosol, is naturally present in the atmosphere and it is produced mainly by earth crust erosion, sea spray and volcanic activities. However, nowadays, a significant part of the particulate present in the atmosphere is derived by anthropogenic activities: mainly combustion of fossil fuels, biomass, industry and mining, only to cite few of them. The properties of the anthropogenic aerosol differ significantly from the natural one and, unfortunately, its effects on the climate and the human health are much more severe [10–14]. Anthropogenic particulate contains large quantities of carbonaceous compounds which in general are characterized by an high absorption of the solar radiation. As consequence, the increasing aerosol concentration is responsible of the *direct atmospheric forcing*: a significant part of the incident solar radiation is absorbed by the suspended aerosol and transformed in heat with the effect of an increasing of atmospheric temperature. An effect similar to the one of greenhouse gases [9]. The presence of particulate in the atmosphere has negative effects on the cloud lifetime and when it deposits on high-albedo surfaces, such as snow and glaciers, it decreases their albedo accelerating their melting process [15–19].

Furthermore, anthropogenic particulate contains compounds which are well known to be harmful for the human health or carcinogenic (polycyclic aromatic hydrocarbons, polychlorinated biphenyls, etc.). When the particles are inhaled by humans, according to their size, they enter the respiratory system and can reach the alveoli or enter the blood stream. It has been proved how high concentration of aerosols, which usually occurs in industrial areas and cities, can increase the incidence of several diseases such as bronchitis, inflammation of the first respiratory tracts, asthma, intoxication and cancer [20–24]. It has been estimated that every year more than two million of deaths are caused by aerosol pollution [25, 26].

In order to understand the processes involved in the aerosols life and its geographical distribution, and to assure safe life conditions it is mandatory to continuously monitor the concentration of atmospheric particulate matter and to effectively characterize its properties in the most accurate and widespread way as possible. Unfortunately, aerosol instrumentation is nowadays quite bulky and expensive and this represents a limit for capillary monitoring the atmospheric particulate. Moreover, results provided

from these instruments present significant uncertainties (which can reach also the 40%) due to the different measurement methods employed and the wide range of possible interferent which can affect this type of measurement [27].

The reference method recommended in the regulations is the gravimetric method. It employs a sampling filter to accumulate the particulate [28,29]. The filter is weighted before and after the deposition and the weight difference allows one to calculate the average concentration of particulate. However, this approach, even thought very accurate, requires complex filter conditioning, very expensive equipment and cannot work in realt-time. It does not provide information about the size distribution on the particles and does not perform any further analysis such as chemical composition or light absorption. Other measurement methods are available which are able to provide more information about the particulate, but they are in general less accurate than the gravimetric approach and still quite expensive.

The developed monitoring system, even thought still in a prototyping state, tries to overcome some of these limitations in order to provide a valid alternative to the classic approaches for the aerosol monitoring. It has been designed to be compact, portable and not expensive in order to make it possible to arrange a distributed monitoring network which can provide a more complete information on the particulate typology and geographical distribution. This is useful both because it can better assess the air quality for people safety, and help to better understand many factors and processes about the life and evolution of aerosol in the atmosphere which are still not well known. Furthermore, the developed monitoring system is able to operate in real-time providing the size distribution of the aerosol with a quite good resolution and, at the same time, exploiting a kind of simple spectral analysis to give information of the particulate typology and chemical composition. Several versions of the system have been realized and tested [30, 31]. They share the same sensing approach but differ according to the filter typology employed in the measurement (more details on the realized prototypes are provided in chapter 3).

A simplified block diagram of the monitoring system is shown in figure 1.1. The system employs two different sampling chambers, the inlet and outlet chambers, respectively connected with flexible tubes to the inlet head and to the exhausted air output. A small air pump installed downstream the sampling filter forces a known air flux throughout the system from the inlet to the outlet. The pump placement prevents any possible contamination and measurement alterations due to the pump operation because the pump deals with already filtered clean air and there is no possibility that either aerosol particles stick inside the pump or particles from the pump reach the filter. The sampling filter is placed between the two chambers and the outlet chamber motion system seals the filter by using two o-rings in order to avoid any air loss during the sampling. Aerosol particles deposit on the top surface of the filter. A back-lighting system, installed in the outlet chamber, provides illumination for the filter and a small high-resolution digital camera, installed in the inlet chamber, periodically takes images of the exposed filter surface. This way the particles deposited on the filter appear as

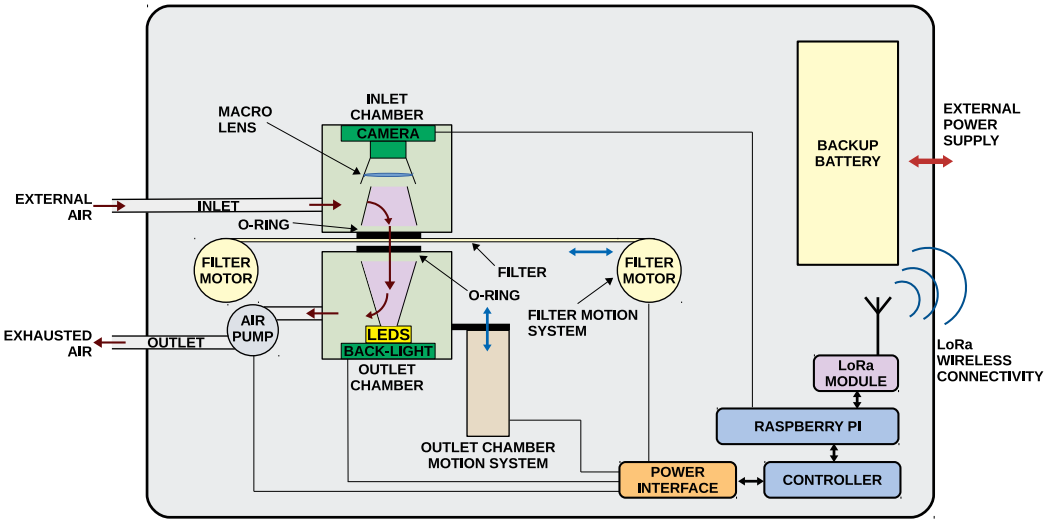

Figure 1.1: Simplified block diagram of the particulate monitoring system.

small dark spots on the whitish filter surface. The camera is connected to a RaspberryPI, a small and cheap single-board computer, which analyzes the images and detects the single particles estimating their size. A filter motion system, which depends on the type of filter employed, move or change the filter when it becomes saturated. The system also includes a real-time microcontroller employed for all the time-critical operations, and a power interface which is responsible for properly controlling the motion system motors. A LoRa module adds a long range wireless connectivity to the monitoring system which can be used to remotely control the measurement process and to arrange a distribute wireless sensing network for atmospheric aerosol. Eventually, a rechargeable backup battery allows the system to operate for short time periods even without a continuous main power supply (as in case of blackouts or employment in recessed locations). The system features very small size ranging from 10 cm × 10 cm × 7 cm, for the simplified portable version, to 20 cm × 30 cm × 12 cm for the complete tape filter automatic version. It can be easily installed inside water-proof enclosures in order to perform long-time outdoor measurement campaigns. Figure 1.2 shows one of the realized prototypes featuring a semi-automatic filter replacement system. Almost all of the mechanical parts have been realized by a 3D printer in PLA.

The back-lighting system employs five LEDs working at five different wavelengths from the near IR to the UV spectrum (940 nm/880 nm, 625 nm, 528 nm, 470 nm and 375 nm). Each LED can be individually controlled by the real-time controller and the RaspberryPI board so that it is possible take the filter images at different wavelengths.

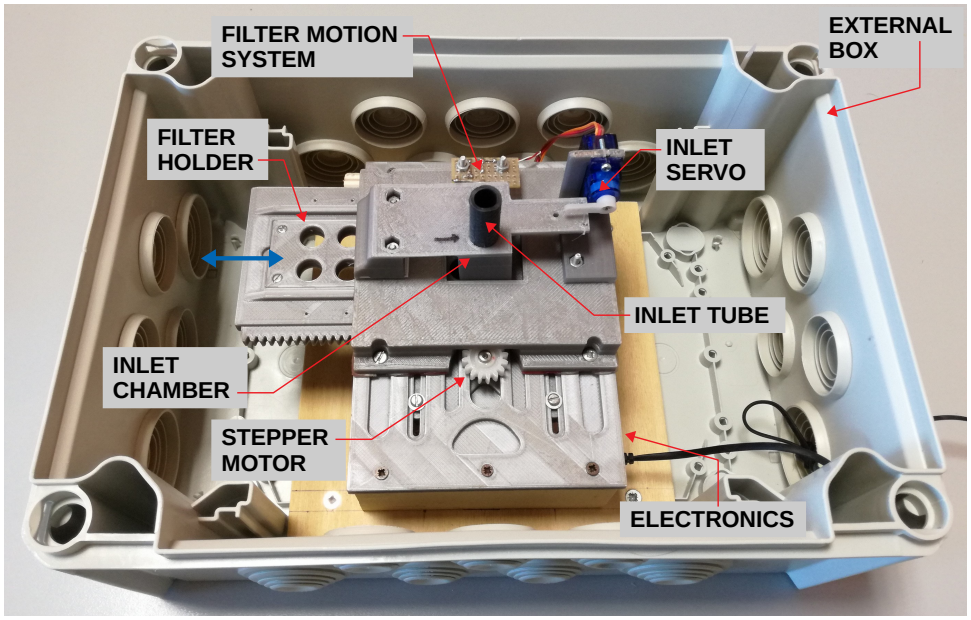

Figure 1.2: One of the realized particulate monitoring prototypes.

This permits to retrieve more detailed information on the captured particulate by implementing a simple spectral analysis. In fact, the light absorption coefficient of the atmospheric particulate matter changes with the light wavelength and the resulting spectrum is a characteristic of the aerosol chemical composition and the particle surface morphology. A suitable classification of these spectra can provide additional information on the chemical composition of the particulate. The detection camera employed in the system is the RaspberryPI Camera NoIR version 2, based on the IMX219 camera sensor manufactured by Sony. This camera has been selected because of its low cost, good performance and direct compatibility with the RasberryPI board. Anyway, other camera models can be employed as well. This specific model features a resolution of 3280×2464 pixels with a spectral response starting from the IR and reaching the UV. The different response sensibility at the different wavelengths can be compensated by acting on the back-lighting LED current and by software image processing. In order to achieve a suitable resolution and magnification a 20× macro lens has been added in the inlet sampling chamber. This allows the system to achieve an effective resolution on the filter surface of about 1 µm/pixel. The system features an automatic filter replacement system (tape filter): when the filter saturates by due to the particle deposition, the system changes the filter measurement spot with a new one and restart the measurement process. This operation is performed by opening the outlet chamber, moving the filter

tape and closing again the chamber. This ensures an automatic virtually non-stop measurement for months. The filter employed in the system is a standard GF10 glass fibre mesh filter. For the manual version of the system a circular 47 mm filter can be used, instead the automatic version uses a tape filter of the same grade.

All the image processing is performed on-board by the RaspberryPI by a custom software developed in the Python language by using the OpenCV library [32]. The software selects the back-light wavelength and takes images of the filter with the camera. The images are processed converting them to gray-scale. After this, the image is filtered with a selective gaussian blurring and with a kernel mask which increases the sharpness of the particle spots. Then, the software detects the single spots by using a globe and a contour detection algorithm, both available in the software and selectable according to the specific type of measurement. Eventually, the software classifies the collected spots according to their equivalent size. From this classification it is possible to estimate the particle concentration in a specified size range by using the following formula:

$$C_{PM} = \frac{\sum_{PM_{min}}^{PM_{max}} M_x \cdot N_x}{\phi_{air} \cdot t_s} \tag{1.1}$$

where PM_{min} and PM_{max} define the size range, M_x is the equivalent mass of a particle of size x, N_x is the number of particles of size x, ϕ_{air} is the air flux generated by the pump and t_s is the sampling time.

Additionally, it is virtually possible to implement on the proposed system the measurement method employed by classical aethalometers. These instruments basically measure the transmissivity of the sampling filter in order to calculate the aerosol absorption coefficient, and from this one, to estimate the aerosol concentration. In the proposed system this can be easily implemented employing the digital camera as a sensor for light intensity without any additional hardware requirement. This secondary approach might be very useful in order to characterize the fraction of the aerosol whose size is less than the camera resolution (1 μm for the developed prototype). Furthermore, the software is able to compare images of the same area taken at the different wavelengths trying to estimate the particle amount according to their spectral response.

Preliminary measurements have been carried out in laboratory in order to asses the performance of the system. A characterization of the air flux generated by two pumps has been performed by using a flow meter for recording the air flux as function of supply voltage. These measurements have been used for calibrating the pump air flux when used for sampling the air. Subsequently, the digital camera together with the selected macro lens have been characterized in terms of resolution achieved on the filter surface by taking pictures of a printed calibration grid. After these preliminary steps, the system has been used to sample air in different locations in North of Italy. The aerosol collected on the filters has been characterized by a Field-Emission Scanning Electron Microscope (FE-SEM) and a first chemical characterization of some of the collected particles have carried out by Energy Dispersive X-ray Spectrometry (EDS). Figure 1.3 shows an area of

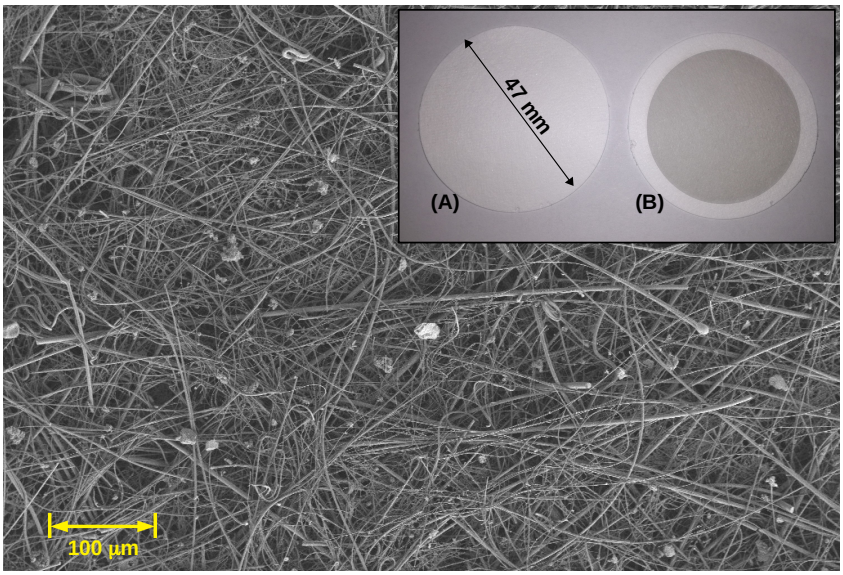

Figure 1.3: Micrography of a glass fibre filter exposed for 24 h in a polluted environment. Inset (A) and (B): filter before and after the exposition.

about 800 µm × 540 µm, obtained using the electron microscope from a glass fibre filter (GM10) exposed for 24 h in a urban polluted environment. In the same figure, images of the filter before (A) and after (B) the exposition are reported. It is clearly visible how the color of the filter changes after the exposition to polluted air and the particles of several sizes and morphology captured by the filter. The aim of these tests was to assess the retention capability of the selected filters and to provide a first morphological and chemical characterization of the sampled aerosol particles.

After this preliminary characterization, a prototype of the system has been tested on the field in the city of Caserta (in South of Italy), where it was available a commercial particulate monitoring station featuring a laser-beam particle counter. A sampling of one day has been carried out by both the instruments, and the results compared. Because of the quite low aerosol concentration in the location (typically about 5 $\mu g/m^3$), an high air flux of 0.5 l/min has been selected in order to increase the system sensitivity. Figure 1.4 shows a filter image taken by the prototype after a sampling of 24 h (A) and the relative map as processed by the detection software (B). The particles captured by the filter have been properly detected and classified according their size. Figure 1.5 reports the size distribution histogram showing how the size peak is centered on about 8 µm. By applying the formula 1.1 to the acquired data the particulate concentration in the range 2.5 µm to 10 µm has been calculated for a final estimation of 0.36 $\mu g/m^3$.

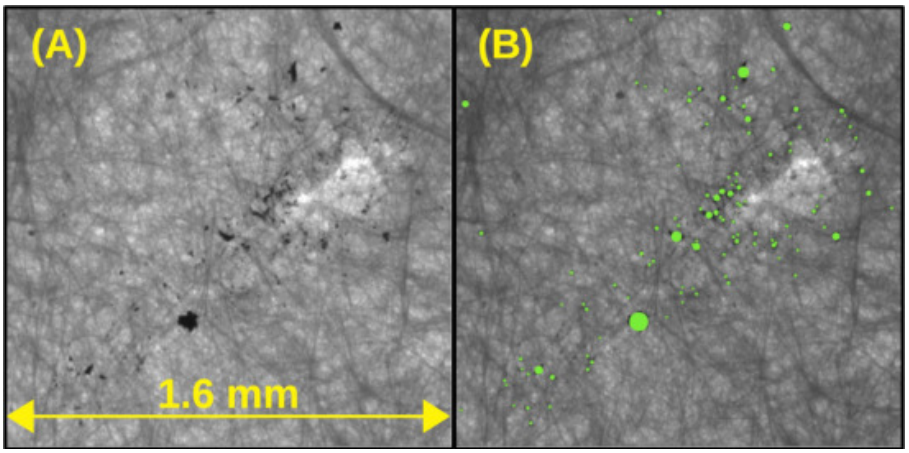

Figure 1.4: Image of the filter exposed for 24 h in the city of Caserta (A), and the relative particulate classification map as evaluated by the prototype software (B).

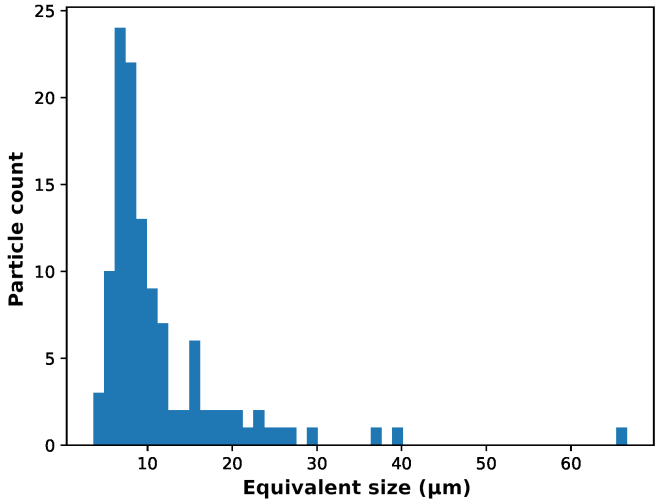

Figure 1.5: Histogram obtained by the classification of aerosol sampled in Caserta showing the particle size distribution.

The obtained data were compared with the values provided by the commercial station. The laser-beam counter provided a concentration of 4.98 µg/m^3 for the PM10 and a concentration of 4.83 µg/m^3 for the PM2.5. Thus, the concentration in the size range of 2.5 µm to 10 µm results in 0.15 µg/m^3, obtained by simple subtraction between the concentrations of PM10 and PM2.5. The results are compared in table 1.1.

The difference of values between the commercial station and the prototype is quite

Table 1.1: Results of the Caserta measurement campaign as provided by the commercial particle counter and by the proposed prototype.

Commercial Station				Prototype
PM10	PM2.5	PM1	PM(10-2.5)	PM(10-2.5)
4.98 $\mu g/m^3$	4.83 $\mu g/m^3$	4.25 $\mu g/m^3$	0.15 $\mu g/m^3$	0.36 $\mu g/m^3$

large. Anyway, the two values are still comparable and it should be taken into account that the nominal accuracy of the commercial station can be also in the order of 20% $\sim$ 30%, according to the particle type and environmental conditions. Thus, results provided by the prototype are reasonably similar to the results of the commercial station but at a lower cost and with more detailed information on the particulate type. Further tests should be performed in order to better assess the performance and the accuracy of the proposed monitoring system. Unfortunately, at this time, it was not possible to find a calibrated device available for performing such additional tests. Additional details on the operation of the proposed system and the results obtained are provided in chapter 3.

1.2 Breath analysis and acetone gas sensing

Gas sensors find application in several fields going from industry, public security and environmental monitoring, for detecting harmful gases, to medical treatment and diagnosis. Many of these applications require very sensible sensors because typical gas concentrations can be of few ppm or ppb [33–35]. Also, it is often required to have low power consumption and small dimension in order to have measurement systems that can be portable and easily usable on the field. Nowadays, great research efforts are carried out in order to reduce the invasiveness of medical tests and diagnosis, and in this framework, the breath analysis is one of the most promising technique for revealing and monitoring a wide set of diseases. It is well known that human breath contains hundreds of gaseous species and compounds which evaporates from the blood stream in the alveoli during exhalation of the breath. Thus, by measuring the concentration of these species it is possible to detect their concentration in the blood of the patient and to gather information which can be similar to a classic blood analysis. Several of these gaseous compounds, called biomarkers, are characteristic of specific diseases and their presence in the human breath can be sufficient to perform a preliminary diagnosis or to monitor the state of a specific disease. Key factors for a breath analysis gas sensor are the sensitivity and the selectivity, because the human breath is a very complex mixture of gases and the biomarkers are typically found in traces [36–39]. Thus, high performance gas sensors tailored for a specific volatile compound are required for this application. Several typologies of gas sensors has been exploited with different results in the past

few years [40–47], but the most promising for breath analysis are surely the *metal oxide semiconductor sensors*, the *electrochemical gas sensors* and the *optical sensors*, because of their high sensitivity, good selectivity, quite low-power consumption and small size. They can be easily arranged in arrays in order to increases gas selectivity and achieve a so called *electronic nose*, a sensing system able to discriminate between several gaseous compounds and measure their concentrations [48].

Metal oxide conductometric gas sensors base their working on reversible adsorption reactions occurring in vacancies and broken bonds present on the sensing surface, typically made by a metal oxide [49–52]. This sensing layer has a semiconducting behavior which can be either N-type or P-Type according to the vacancy type. The gas molecules present in the air are adsorbed by weak bonds to these vacancies and this changes the electronic band structure of the sensing film with the creation of new states. As consequence, the conductivity of the sensor changes in function of the gas concentration reacting on the surface. The relative variation of the sensor resistance, usually taken as output response, is defined as ratio between the resistances of the sensor R_a and R_g respectively measured in absence and presence of the target gas:

$$\begin{aligned} S &= R_a/R_g \quad \text{(for reducing gases)} \\ S &= R_g/R_a \quad \text{(for oxidizing gases)} \end{aligned} \tag{1.2}$$

The sensor sensing performance, basically, depends on the surface reactions between the sensing film and the gases, and these reactions depend mainly by the sensing film material and by its surface morphology [53]. In particular, the material defines which gases can be detected by the sensor, and the morphology defines the sensitivity. As an example, increasing the surface-to-volume ratio of the sensing layer involves a significant increasing in the sensor response and sensitivity towards the target gases because of the increasing number of the vacancy number. For these reasons, nowadays, most of the research in this topic is focusing on developing new materials and new deposition techniques in order to achieve nanostructured sensing films featuring high surface-to-volume ratios together with good reactivity and selectivity towards specific gases. Composite materials obtained by mixing different metal oxides or metal oxides with metals or non-metals nanomaterials, such as gold and silver nanoparticles, graphene or carbon nanotubes, have been exploited with success [53–57]. Another important factor impacting the sensor response is the working temperature. In fact, for a given material and gas, the balance between surface adsorption and desorption processes is controlled by the temperature. In particular, increasing the working temperature has a first effect to enhance the surface reactivity and as consequence the sensor response increases. However, increasing the temperature also increases the desorption processes, being the thermal energy the principal cause to the breaking of adsorption bonds. Thus, the sensor response typical features a bell-shaped characteristic curve in

function of temperature, with an optimal working temperature typically in the range between 100 °C and 600 °C [58], even thought some study reported about highly performing sensors based on nanostructured materials working at room temperature [59, 60].

There are hundreds of works proposing novel conductometric gas sensors based on metal oxides, such as ZnO, SnO_2, WO_3 and many others, but only few of them studied or employed the Nb_2O_5 as sensing material, even thought its sensing properties are quite interesting [61–63]. In this framework, several conductometric gas sensors, based on a niobium oxide thin film, have been developed and tested with the goal to develop a high-performance sensor for medical and industrial application with a specific interest in the breath analysis technique. Those sensors demonstrated very good sensitivity and selectivity towards acetone, a volatile organic compound found in human breath, and a possible biomarker for diabetes [64]. Several studies put in evidence how acetone concentration in human breath greater than about $1 \sim 2$ ppm are indicative of diabetes in the subject [65, 66].

Figure 1.6 shows one of the realized sensor prototypes. In the figure are visible:

- The alumina substrate with dimensions of 6 mm×3 mm and a thickness of 1 mm. This substrate with the screen-printed electrodes is available off-the-shelf ready to be deposited.
- The platinum interdigitated electrodes (IDEs) and the deposited Nb_2O_5 sensing film, on the top side of the substrate. The interdigitated structure helps to achieve a lower base resistance of the sensor. The sensing thin film, visible as a opalescent darker square, is deposited upon the IDEs and has an active area of about 3 mm $\times$ 3 mm.
- The platinum heater, on the back side. This heater is employed to set the working temperature of the sensor.
- The contacts, on both sides, which are used to connect the sensor to the read-out electronic system. The read-out system has to drive the heater in order to properly control the working temperature of the sensor and, at the same time, to measure the sensor resistance for evaluating the actual gas concentration.

The Nb_2O_5 thin film has been deposited by *reactive magnetron sputtering* in the laboratory-scale plasma reactor shown in figure 1.7. The reactor has a stainless steel vacuum chamber with two asymmetric parallel-plate capacitively-coupled electrodes. The cathode electrode, made of the target metal, is connected to an an RF power generator working at 13.56 MHz. An impedance matching network allows one to properly adapt the power supply output impedance to the reactor one in order to maximize the power transfer. The substrates are placed on the ground electrode (anode) which is provided with a dedicated cooling system for stabilizing the deposition temperature. Because of the plasma generated between the two plates, the target is etched by sputtering and,

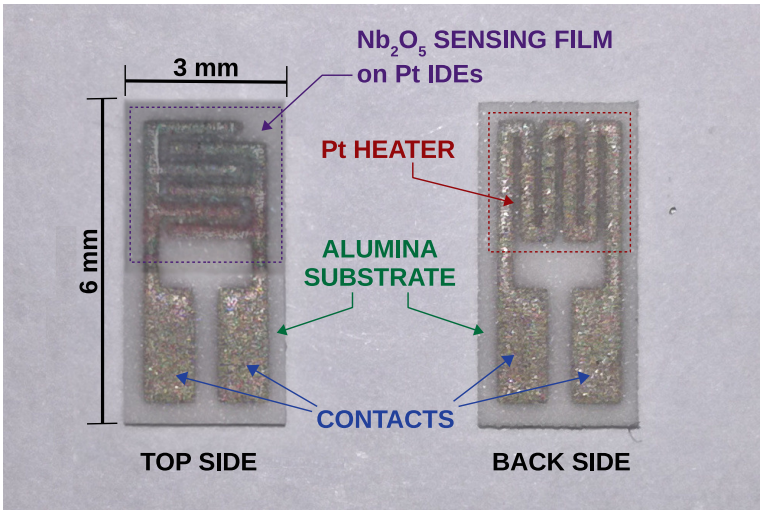

Figure 1.6: One of the sensor prototypes realized by plasma sputtering.

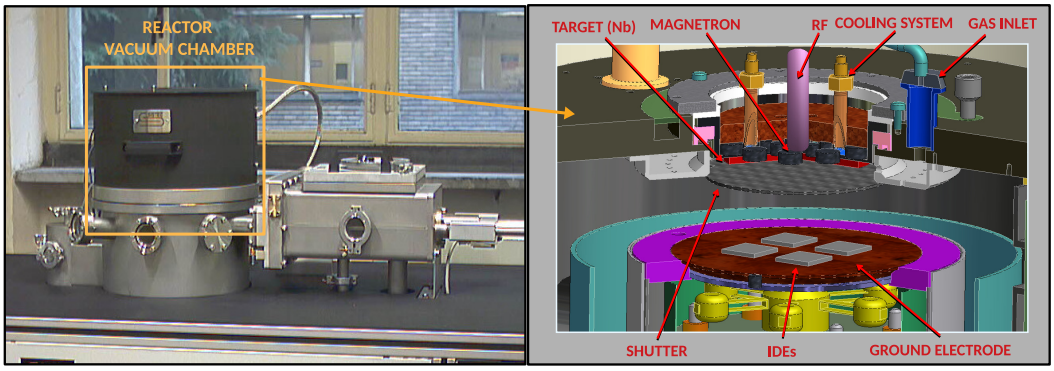

Figure 1.7: Plasma reactor employed for the deposition of the sensor prototypes.

after reacting with the gases present in the reaction chamber, finally deposits on the anode and, thus, on the substrates. All the depositions have been performed employing a target of Nb (99.99% purity) attached on the cathode, and a controlled mixture of Ar (99.99% purity) and O_2 (99.99% purity) at the plasma floating temperature ($T < 60$ °C) with a total pressure of 100 mTorr.

Several different combinations of the deposition parameters (O_2/Ar flux rate ratio, RF power and deposition time) have been tested and the most promising prototypes have been fully characterized. Table 1.2 reports, for each one of the characterized sensors, the deposition parameters and the resulting film thickness.

A preliminary characterization of the chemical composition and surface morphology has been carried out for each prototype. The Field Emission Scanning Electron Microscopy (FESEM) has been employed to characterize the structure and the morphology

Table 1.2: Deposition parameters of four of the realized prototypes and the resulting film thickness.

Prototype	O_2 (sccm)	Ar (sccm)	RF Power (W)	Dep. Time (min)	Thickness (nm)
#1	50	20	150	60	160
#2	50	20	250	30	200
#3	50	20	500	30	500
#4	50	20	500	60	900

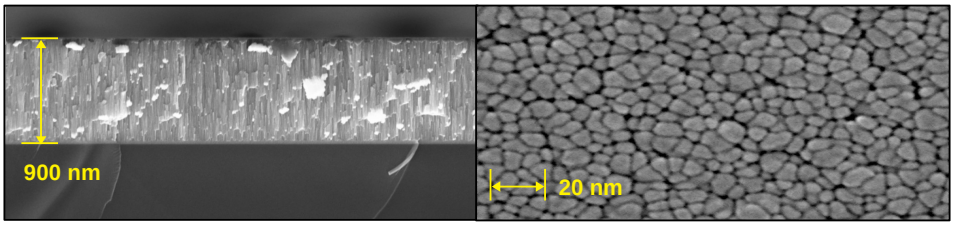

Figure 1.8: Image showing the section (left) and surface morphology (right) of the film deposited on prototype #4.

of the deposited films. Several images of the films were taken with a Supra 40 FESEM (Zeiss) and revealed two different cases. Thin films (#1 and #2) feature a quite compact structure with a smooth surface. Thick films (#3 and #4), instead, have a porous structure mainly composed of thin vertically aligned nano-rods with diameters ranging from 10 nm to 20 nm. It is possible to note that the film thickness increases with the power and the deposition time. As an example, figure 1.8 shows the film section and its surface morphology for the prototype #4.

The X-ray Photoelectron Spectroscopy analysis (XPS), performed with a PHI Model 5000 equipped with an aluminum anode monochromatic source (1486 eV energy) and operating at a pressure below 5×10^{-8} mbar, a power of 25 W and an high-resolution scan pass energy of 11.75 eV, revealed for all the samples that the deposited film is mainly composed by niobium oxide with an oxidation state corresponding to Nb_2O_5(V). As an example, in figure 1.9 it is reported the XPS spectrum for the sample #3, corrected using as reference energy the C 1s line (284.6 eV). The C 1s, O 1s and Nb 3d lines are clearly visible. In particular, the two peaks at 207.1 eV and 209.8 eV, representing respectively the doublet of Nb $3d_{5/2}$ and of Nb $3d_{3/2}$, confirm that the principal component of the deposited film is Nb_2O_5.

Subsequently, a characterization of the sensing performance for the four prototypes

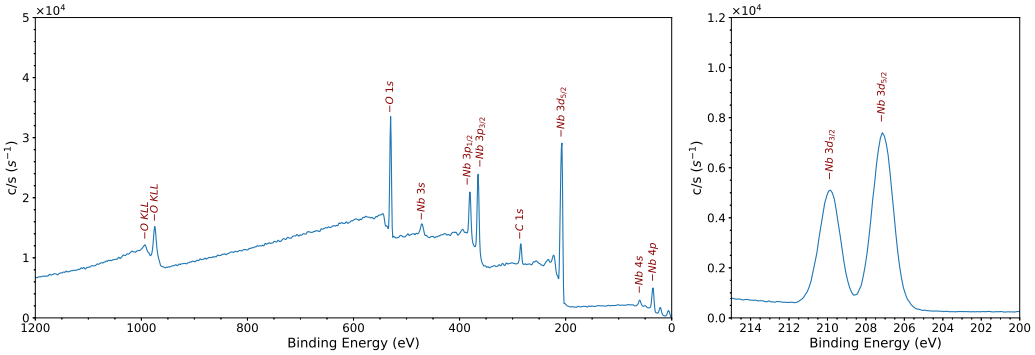

Figure 1.9: The XPS spectrum acquired on the prototype #3 (left) and the detail of the Nb_2O_5 characteristic peaks (right).

was performed. A lab-scale measurement setup, specifically designed for the characterization of gas sensors, was used. The setup, shown in figure 1.10, employs certified gas bottles and mass flow controllers to generate an accurate gas mixture. The sensor under measurement is placed inside a small chamber, where the generated gas mixture is made to flow at a specified flow rate. A digitally controlled power supply (Agilent E3632A) is used together with a software application to set the working temperature of the sensor by modulating current and voltage passing in the sensor heater and measuring its resistance. The sensor resistance is measured by using a source meter Keithley 6487 and acquired by a computer application. Before starting the characterization, each sensor was conditioned in air at a temperature of 400 °C for 2 h in order to remove any possible contaminants and to stabilize the Nb_2O_5 film. Then the sensing performance were characterized by using synthetic dry air (80% N_2 and 20% O_2) as carrier gas and a variable amount of the target gas.

First characterization evaluated the dependence of the sensor sensitivity as function of the working temperature. Measurements were performed on the prototypes #1, #2 and #4 with 5 ppm of acetone at five different temperatures in the range of 200 °C to 400 °C. Experimental data are shown in figure 1.11. It is possible to see how the tested prototypes have a quite different temperature dependence. In fact, sensors #1 and #2 exhibit maximum sensitivity at a working temperature of 350 °C. Instead, best response of sensor #4 is achieved at a temperature of 300 °C. Furthermore, it is possible to note how the sensitivity of sensors #2 is much higher than the other two.

This characterization allowed one to assess the best working temperature for the prototypes: 350 °C and 300 °C respectively for sensor #2 and #4. Such temperatures were employed for all the subsequent tests. Also response and recovery times of both sensors where assessed and the data are shown in figure 1.12. It is possible to note how sensor #2 is characterized by an extremely fast response and recovery time, respectively in the order of 5 s and 40 s. Moreover, such times are almost independent from working

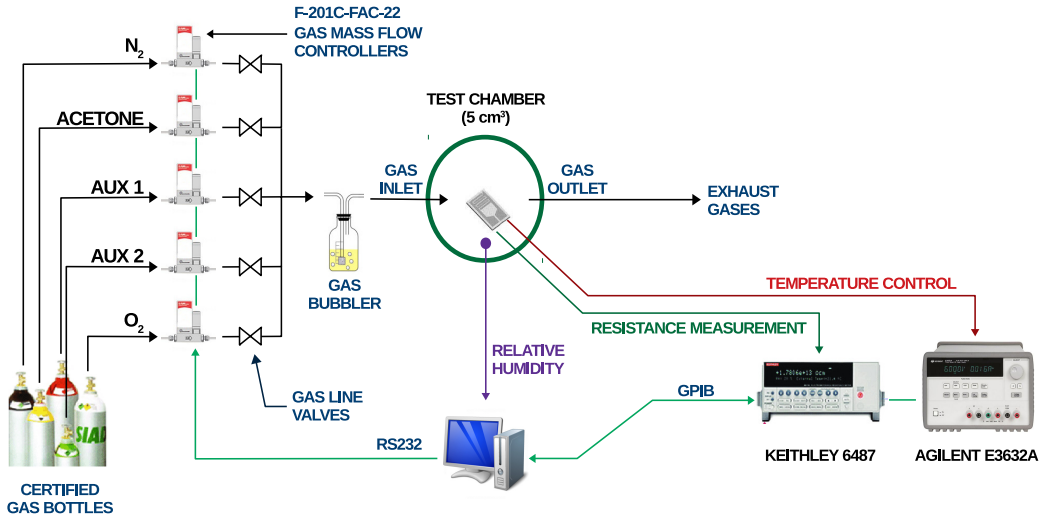

Figure 1.10: Block diagram of the measurement setup employed for the characterization of the prototypes sensing performance.

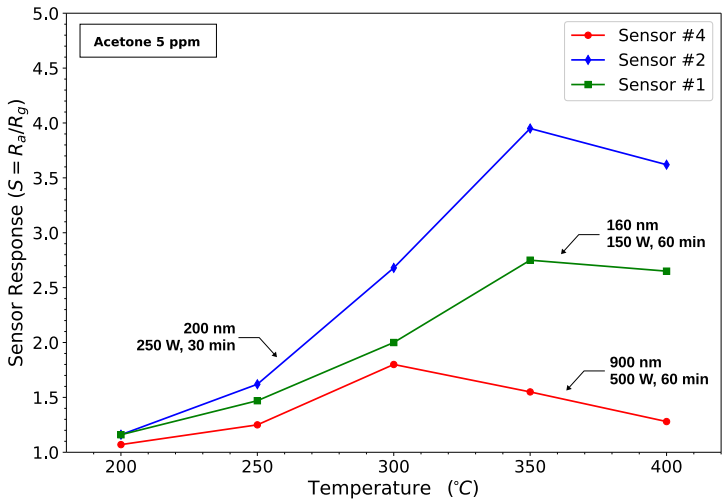

Figure 1.11: Dependence of the sensor sensitivity towards working temperature in the range of 200 °C to 400 °C.

temperature. Instead, sensor #4 exhibits much higher response and recovery times in the order of 120 s with a strong dependence from the working temperature. This difference can be explained taking in account the different morphology and thickness of the two sensing films: acetone interaction with the sensor #2 does not involve any significant

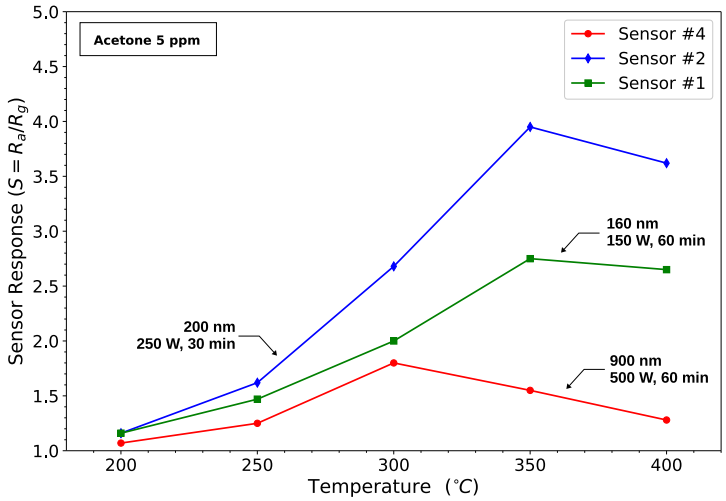

Figure 1.12: Response and recovery times obtained with 5 ppm of acetone for both sensors #2 and #4.

diffusion process due to its low thickness and high compactness.

Subsequently, the response of the sensors #2 and #4 were evaluated at different acetone concentrations. Results of this characterization are shown in figure 1.13 and 1.14, respectively, for sensor #2 and #4. Here, it is evident the significant difference in sensitivity between the two prototypes. Sensor #2 has a much higher sensitivity but a lower saturation limit. In particular, its response can be considered linear up to a concentration of 3 ppm. At higher concentrations its response saturates quickly up to reaching a complete saturation at about 12 ppm. In contrast, sensor #4 exhibits a lower sensitivity but with a much higher saturation limit. Its response is almost linear up to 10 ppm and still does not reach a complete saturation at 50 ppm.

Linear and quadratic fittings of the experimental data were performed with the aim of determining a mathematical relation able to model the sensor sensitivities in the tested ranges. This allowed one to find the following relations:

$$\begin{aligned}
&\text{Sensor } \#2 \\
&\qquad X = 4.16 \cdot (S-1) \quad (\mathrm{X} \leqslant 3\,\mathrm{ppm}) \\
&\qquad X = 13.1 - \sqrt{206 - 35.1 \cdot S} \quad (\mathrm{X} \leqslant 12\,\mathrm{ppm}) \\
&\text{Sensor } \#4 \\
&\qquad X = 1.5 \cdot (S-1) \quad (\mathrm{X} \leqslant 10\,\mathrm{ppm}) \\
&\qquad X = 122 - \sqrt{15900 - 1000 \cdot S} \quad (\mathrm{X} \leqslant 50\,\mathrm{ppm})
\end{aligned} \tag{1.3}$$

where X is the acetone concentration and $S = R_a/R_g$ is the measured sensor response

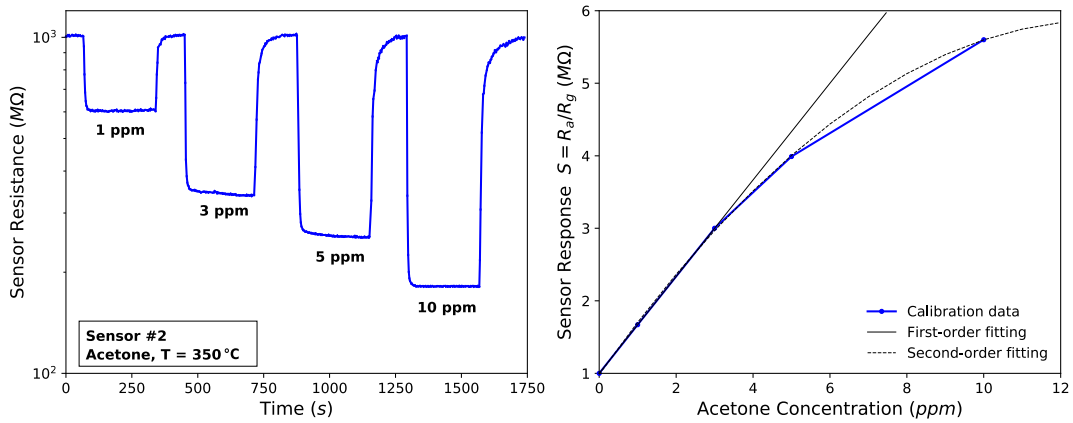

Figure 1.13: Sensitivity of sensor #2 towards acetone in a concentration range of 1 ppm to 10 ppm and the calibration curves obtained from the experimental data.

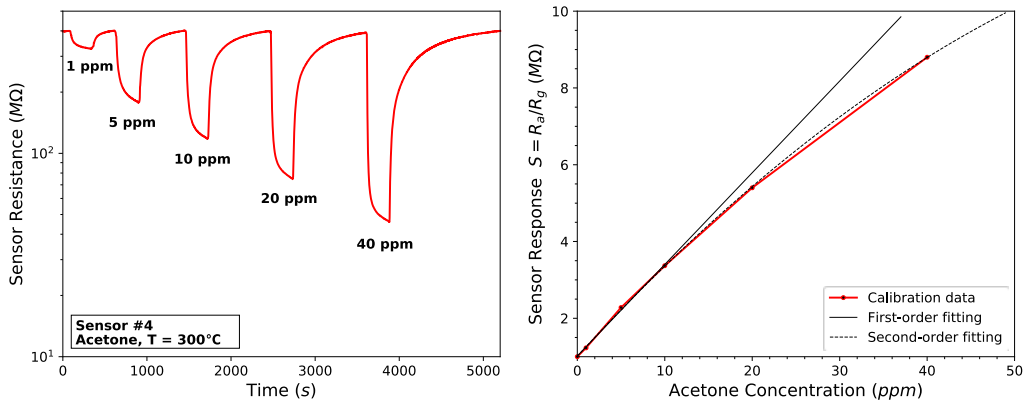

Figure 1.14: Sensitivity of sensor #4 towards acetone in a concentration range of 1 ppm to 40 ppm and the calibration curves obtained from the experimental data.

as defined in equation 1.2. Thus, by using these relations it is possible determine the acetone concentration from the measurement of the sensor resistance.

Next characterization performed on the sensors was the selectivity test. The response of both sensors were acquired using different target gases and compared with the response to acetone in order to assess how much these interferent gas can affect the measurement of acetone. Figure 1.15 reports the acquired normalized responses. It is visible how all the tested gases have a response that is significantly lower than the acetone one, especially for sensor #4. In particular, the response to CO_2 and to O_2, which are typically present in the human breath in large concentration, are negligible. The only significant interferent gas detect was ethanol. Anyhow, this does not represent a

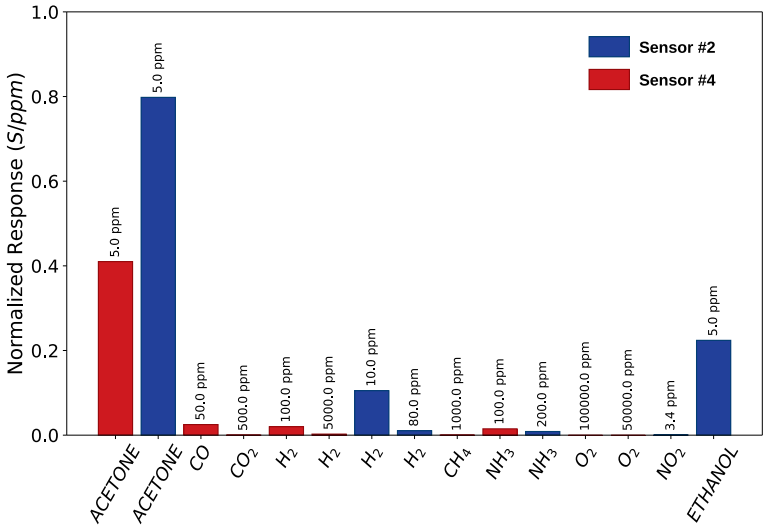

Figure 1.15: Normalized responses to acetone and principal interferent gases for both sensors #2 and #4.

significant issue for the employment of the proposed sensor in the breath analysis of diabetes. In fact, ethanol is present in the exhaled breath at significant concentrations only after the intake of alcohol. Therefore, avoiding any alcohol assumption before the acetone test is enough to avoid such an interference. The quite good response of sensor #2 towards ethanol suggested to perform additional tests in order to better assess the sensing performance towards this gas. These additional tests are demonstrating good performance also towards ethanol at concentration up to hundreds ppm. By taking advantage of such response it is possible to employ such sensors for the detection of ethanol as well.

Eventually, sensor stability and recovery capability were also assessed with a dedicated test. The response to several repeated acetone pulses at a concentration of 5 ppm was acquired for both sensors. As an example, figure 1.16 shows five repeated pulses: no significant offset or hysteresis in the sensor responses can be observed. Moreover, both sensors recover after each acetone pulse to their respective reference resistance. This highlights the reversibility of the reactions occurring on the sensor sensing surface.

In conclusion, the proposed sensors demonstrated very good sensing performance towards acetone. The sensitivity of both sensors #2 and #4 is suitable for the detection of acetone at the ppm level with operative temperatures between 300 °C and 350 °C. Sensor #2, thanks to its high sensitivity, is particularly suitable in applications where a very low acetone concentration is expected, also below the ppm level. In contrast, sensor #4 is more suitable in applications where the expected acetone concentration is higher, because of its larger saturation level. Both sensors exhibits a very good stability with negligible drift also after repeated interactions with many interferent gases,

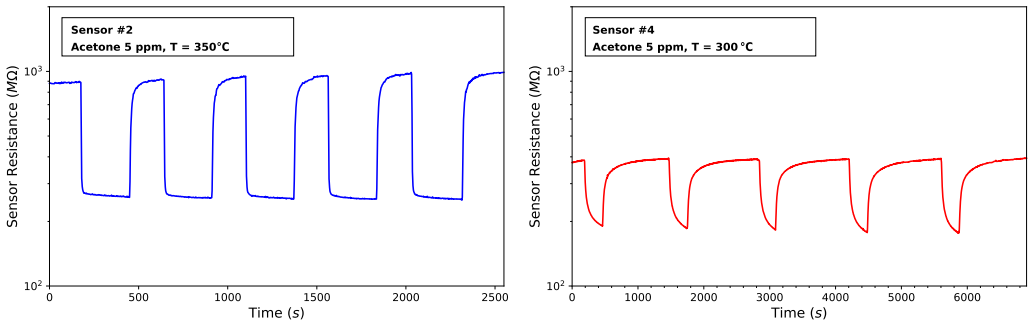

Figure 1.16: Response to five repeated acetone pulses at a concentration of 5 ppm respectively for sensor #2 (left side) and sensor #4 (right side).

including very aggressive ones such as NO_2 and NH_3. Furthermore, sensor #2 demonstrated extremely fast response time, in the order of few seconds. This is a characteristic not always easy to obtain with MOX sensors and very desirable in many fields, such as the breath analysis: a fast response of the sensor can reduce the patient effort and stress during a breath sample. Selectivity of both sensors is excellent towards acetone with only ethanol as possible interferent gas. Additional details and data are reported in chapter 5 both for acetone and ethanol tests.

Chapter 2

Atmospheric particulate matter

Atmospheric particulate matter, or aerosol, is one of the most dangerous pollutants for human health and climate. It is composed by tiny solid and liquid particles suspended in the atmosphere with sizes ranging from few nanometers to several hundreds micrometers. Its effects on human health are well known: transitory inflammation of the respiratory system, lung cancer, intoxication and cardiovascular diseases, just to name few of them. Particulate has also several effects on climate and among them there are direct and indirect climate forcing.

Monitoring of the atmospheric particulate matter is, therefore, mandatory in order to safeguard human health and assess its geographical and temporal distribution. Unfortunately, the instruments available nowadays are typically expensive and bulky, and this limits their employment in several applications such as the capillary monitoring of particulate in urban areas. Such a monitoring is extremely important because of the high particulate concentration and the high population density reached in big cities.

With the aim of finding an alternative to conventional particulate monitoring systems, a low-cost portable solution for the aerosol monitoring based on an novel optical approach was developed and characterized.

This chapter introduces the topic providing in section 2.1 some generic information of the atmospheric particulate matter, its principal characteristic, sources and effects. Section 2.2 gives a summary on the current state-of-art equipment employed in the aerosol measurements. The proposed solution is described in chapter 3, where advantages and drawbacks in respect to the conventional methods are also highlighted. Eventually, section 3.2 reports the achieved results and the characterizations performed in order to validate the performance of the proposed monitoring system.

2.1 Atmospheric aerosol basics

Atmospheric particulate matter, or aerosol, is a mixture of minute solid or liquid particles suspended in the atmosphere. The characteristics of these particles is highly variable, but they are usually classified according to their mechanical, physical and chemical properties, and according to their origin. Basically, particulate matter can be composed by carbonaceous particles, including elemental carbon and organic compounds, mineral dust and inorganic salts, with size ranging from tens of nanometers to hundreds of micrometers [6, 7]. Harmful particulate matter is mostly produced by human activities and its geographical distribution is very variable in space and time, and strongly affected by the local weather conditions [67].

2.1.1 Main properties of particulate matter

Even though many efforts have been carried out in last years in order to achieve a standard classification or nomenclature about the particulate matter, till now there is no one common agreement on the topic [8]. However, the effects of atmospheric particulate matter are strongly related with its properties. Thus, it is very important to accurately define the most important ones.

- Size and morphology – The term *size* refers to the dimension of the single particles composing the aerosol. These dimensions are usually in the range of about 10 nm (such as ultra-fine particulate produced by combustion of fossil fuels) to 100 μm (like mineral dust generated by natural erosion). However, these particles are characterized by an highly variant *morphology*: spherules, wired-shaped particles, conglomerates, fractal-like chains and many others. Size of particles can be evaluated after deposition by using optical and electronic microscopes. Because morphology strongly affects the aerodynamic behavior of the particle and the way they interact mechanically with the environment, it is of common use, especially within the framework of legislative regulations, to refer to the *equivalent aerodynamic size* of particles using the "PM Scale". An arbitrary-shaped particle having an aerodynamic equivalent size of x μm behaves into the air in the same way as a spherical particle having a diameter of x μm and a density of 1 kg/dm^3. According to the PM Scale, for example, PM10 refers to the amount of particles having an average aerodynamic equivalent size less than or equal to 10 μm. Commonly used standard sizes for monitoring particulate matter in urban environments are PM10, PM2.5 and PM1. Often, regarding the particulate size, the terms *coarse particles*, *fine particles* and *ultra-fine particles* refer respectively to particles having an equivalent diameter greater than 2 μm, less than 2 μm but greater than 200 nm and less than 200 nm. The term *aerosol* is commonly used for fine and ultra-fine particulates which are characterized by a longer lifetime [7].

- Microstructure – The *microstructure* of an aerosol particle is both a superficial and bulk property and refers to the way atoms or molecules are arranged in the particle. Microstructure strongly affects thermal and chemical interaction between particles and environment, and the light absorption coefficient. Microstructure depends mainly on chemical composition of the particle and its source (i.e. the processes involved in its production). As an example, porosity of a particle depends on its microstructure. Particles characterized by an high porosity can have larger light absorption or can be more reactive than less porous particles even with the same chemical composition.

- Chemical composition – *Chemical composition* refers to the elements contained in the particles. They can be very different according to the aerosol source and the processes the particle has seen during its lifetime. As reported in section 2.1.2, the most common compositions of atmospheric particulate matter are: carbonaceous materials, inorganic salts and mineral dust [7–9]. Chemical composition is a very important property of particulates because it affects other properties like light absorption, chemical and thermal stability, and solubility. Moreover, several harmful effects, such as toxicity and carcinogenicity, depend on the chemical compounds present in the particles. Chemical composition can change during the aerosol lifetime by reaction with the atmosphere and other particulates, or degradation by thermal and radiative processes. Often particulate matter is characterized by a mixed composition or conglomerates featuring different types of particles, and this makes more difficult achieve a reliable characterization.

- Light absorption – *Light absorption* is directly linked to the effects of particulate on the climate. With light absorption is intended the capability of particles to absorb the incident light transforming electromagnetic energy into thermal energy. It is well known that, when light interacts with the matter, or in this specific case with an aerosol, part of incident energy is transmitted, part is reflected (or scattered) and the remaining part is absorbed and transformed in thermal energy inside the particles. This process depends mainly from the specific material (chemical composition), its microstructure and surface morphology, and the wavelength of the incident light. Several types of aerosol have quite specific absorption spectra which can be used to identify their species. Regarding the particulate species and their light absorption it is possible to identify three main categories: *mineral dust*, *black carbon* and *brown carbon* [9] which are discussed in more detail in section 2.1.2.

- Solubility – *Solubility* refers to the capability of a specified type of atmospheric particulate to dissolve in the atmosphere or in water. Solubility in the atmosphere occurs by reaction of the particles with gases normally present in the atmosphere, instead, solubility in water mainly occurs in clouds with the dissolution of the

particles in the droplets. Solubility of aerosols depends mainly on chemical composition, morphology and microstructure of the particles. Black carbon, for example, is almost insoluble in any solvent, instead inorganic salts are usually highly soluble in water [68].

- Thermal and chemical stability – The term *chemical stability* expresses the ability of a given atmospheric particulate to do not chemically react with the environment and other particles. Such a kind of aerosol can remain into the atmosphere for long time without changing its chemical properties. Instead, the term *thermal stability* refers to the capability of a particulate to sustain heat (high temperatures) without degrading or changing its mechanical, physical, and chemical properties. For example, elemental carbon aerosols are know to have a very high thermal and chemical stability [8, 69, 70].

- Lifetime – *Lifetime* of atmospheric particulate matter refers to the average time a given particulate specie remains suspended in the atmosphere before depositing on the earth or degrading chemically or thermally. Even though these removal processes are till now not well understood [71], deposition by wet precipitations can be considered the dominant process of removal [72]. In this process, the particles acts as nucleation for condensation in the clouds or are captured by cloud droplets and deposit with the precipitations. From direct observations and modeling, lifetimes of atmospheric particulate matter range from few days to some month [71], with an high variability due to size, chemical composition and local weather conditions but, in general, finer particles have longer lifetimes than coarse one.

It is extremely difficult to provide a comprehensive classification of the different types of aerosols due to the high variability of their characteristics. The section 2.1.2 discusses in detail the most important types of atmospheric particulate matter.

2.1.2 Widespread particulate types

Among all different types of aerosols, the most important for their amount in the atmosphere and their effects surely are: inorganic salts, mineral dust and carbonaceous materials, especially black carbon and brown carbon [7–9].

Inorganic salts – Inorganic salts are usually highly soluble in water and, among them, the most widespread is in the form of mixture of various sulfate and nitrate compounds (especially ammonium sulfate, sodium chloride, sodium sulfate and sodium nitrate). Their solubility depends from several factors, size, shape, morphology and the possible coverage of particles with insoluble nanometric particles [68]. They can also react chemical producing secondary aerosols with formation of acids and insoluble compounds, especially when naturally originated aerosols react in polluted areas [73–75]. Partially, these aerosol are naturally originated by sea sprays, but a non-negligible part

of them derives from combustion of fossil fuels and industrial process. Due to the highly solubility, these aerosols dissolve in the cloud droplets precipitating on earth through wet deposition. Their lifetime is quite small, from days to one week according to weather conditions and processes they are subjected to. Generally, inorganic salts exhibit an high scattering of light with quite low absorption, but high-absorbing secondary aerosols can be generated by interaction with other species [13, 75, 76].

Mineral dust – Mineral dust is the most abundant particulate matter present in the atmosphere. Mineral dust are primary produced by natural sources (earth crust erosion, soil dust, volcanic activities) but also human activities, such as mining, deforestation and forest fires, contribute to increase its concentration in the atmosphere [7, 13]. The mineral content includes silicates, quartz, hematite, clay minerals, calcite, gypsum just to cite few of them. Moreover, these mineral are usually present as a mixture in the aerosol. Thus, due to their highly variable properties (size, composition, morphology), it results quite difficult to accurately characterize this kind of particulate and its effects on the climate. Typical sizes range from 100 nm to 100 μm with shapes which are usually non-spherical. Deposition is usually dominated by gravitational settlement for coarse particles and by wet deposition for fine aerosols with highly variant lifetimes. The absorption spectra can largely change in dependence of the mineral content, but typically they exhibit a non-constant absorption with large variations in the near IR and UV regions of the solar spectrum. Quartz aerosol are very abundant in the atmosphere and they are characterized by a strong absorption in the near IR and almost no absorption in the visible and UV regions of the solar spectrum. Hematite and clay minerals exhibit a strong absorption in the visible and UV regions. There is not a general agreement about the effects of mineral dust aerosols. Some studies show that their absorption and scattering balance can have a significant effect on the atmosphere heating enhanced by their abundance [13, 77, 78].

Black carbon – Black carbon is an extremely important aerosol type due to its severe effects on climate and human health. It is a carbonaceous particulate matter characterized by a deep black appearance and an absorbing coefficient which is inversely proportional to the wavelength of the incident light (the imaginary part of its refractive index is almost independent from wavelength) [9, 79, 80]. This large absorption of solar radiation makes the black carbon one of the main causes of radiative forcing of atmosphere. Black carbon is produced by combustion of fossil fuels and biomass and its emission is in the order of 10 Tg/year [81]. The processes involved in its generation are quite complex. They start from the pyrolysis of the fuel with generation of small molecules mainly composed by polycyclic aromatic hydrocarbons. These molecules grow up producing small particle nuclei which start absorbing gas molecules or conglomerating with other particles. Particles are usually hydrophobic with a low solubility in atmospheric water, even though it is reported that part of them can react in the atmosphere and become hydrophilic. Deposition can occur by several processes but dry and wet ones are dominant with a typical lifetime of one week [82, 83]. Terms as *soot*, *insoluble carbon*, *elemental carbon* or *graphitic carbon* are often referred to black carbon aerosols,

because of their black appearance and strong absorbing coefficient. However, they differ for chemical composition, microstructure and thermal stability from what is commonly considered black carbon. In particular, elemental and graphitic carbon contain only carbon. They are characterized by an high thermal stability (refractory material) and usually a low chemical reactivity with other species (insoluble in almost every solvent) [84].

Brown carbon – Brown carbon, in analogy with black carbon, is a carbonaceous particulate which appearance is brownish. It is composed mainly by organic carbonaceous compounds, especially the water soluble fraction, and humic substances. It is characterized by an strong light absorption in the higher part of visible spectrum and in the UV [85–88]. Its origin is still not well understood, but smoldering combustion of the biomass seems to be its main source [89]. Brown carbon acts in a way similar to black carbon with a radiative forcing effect. Furthermore, the organic compounds composing brown carbon can be extremely harmful for human health.

2.1.3 Primary and secondary sources of atmospheric particulate matter

In the previous sections several sources for the atmospheric particulate matter have been presented. Actually, the processes at the base of the particulate production are quite complex and typically more processes can coexist in the formation of an aerosol. Identifying the source a specific aerosol is very important because most of the particle properties, lifetime and geographical distribution depend on its production processes. The sources, which directly emits the particulate in the atmosphere, are called *primary sources* and are responsible for the emission of the larger part of total atmospheric matter. However, particulate can be generated in several other ways. A part of the primary particulate can react with other species in the atmosphere generating other particulate types, or new particles can be produced by chemical reactions directly in the atmosphere (*airborne aerosol*) [14, 90]. Such sources are, therefore, called *secondary sources* and their contribution to the total particulate amount and to local and global effects are surely not negligible. In particular, airborne particulates are strictly depending on the local atmospheric composition (which can change with time and space) and by weather conditions. Thus, the production of airborne particulate is extremely difficult to study. As already partially discussed, not all the atmospheric particulate matter is introduced into the atmosphere by anthropogenic activities. A significant part is generated by *natural sources*, and it can enhance or contrast the effects of the anthropogenic part. Many studies have tried to estimate the global emission of particulate (especially the carbonaceous one). Of course, such estimations cannot accurately describe the actual situation, but they can provide a qualitative indication of the amount of particulate yearly introduced in the atmosphere. Table 2.1 summarizes the results of a model which tries to simulate the particulate behavior on a global scale [67], dividing the emission by source. Some interesting considerations can be done on these data:

Table 2.1: Global emissions of fine carbonaceous aerosols as estimated by [67].

source	black carbon aerosol (Tg/year)	organic carbon aerosol (Tg/year)
fossil fuels	6.64	28.5
biomass	5.63	44.6
natural sources	0	7.8

1. The largest part of carbonaceous aerosol is of organic.
2. The dominant source is the combustion of biomass (burning of tropical forests and savannas, agriculture, home heating, etc.).
3. Natural sources (photochemical oxidation of terpeni emitted by vegetation) are responsible with the least amount, but they not negligible. The only electrophilic gases present in the atmosphere in concentrations high enough to photochemically produce oxidization are *hydroxyl radicals* (OH), *ozone* (O_3) and *nitrate radicals* (NO_3). The concentration of these gases change according to the hour of the day (day or night) and to the incident radiation. In order to have condensation or nucleation of the oxidized species with the formation of new particles it is required that the oxidation reaction has a sufficient speed and that the product has a vapor pressure higher than the source gases [90].
4. The main source of black carbon is the combustion of fossil fuels with properties depending on the temperature, oxygen level and fuel type employed during the combustion (transportation, industries, electricity generation).
5. No black carbon is introduced naturally in the atmosphere.

Beside the classical particulate sources, which have been already discussed, there are some that are usually underestimated. One of them is the natural degradation of bulk vegetables which involves the emission of quite large organic particles that can be transported very far by source due to wind circulation (i.e. aeolian dust on the Atlantic Ocean) [91]. The vegetation also introduces other types of particles: pollen and spores. A part of atmospheric particulate is composed by living beings: viruses and bacteria are found ubiquitously in air. Other natural source of organic particulate is the sea. Sea bubbles breaking on the sea surface emit large quantities of particulate mainly composed by soluble salts. However, many studies have proved which part of these particulates includes organic compounds as coating of the salt nuclei [92, 93]. Lastly, a small part of atmospheric particulate is radioactive for direct emission by radioactive material (nuclear reactors, nuclear weapons, natural erosion of radioactive materials) and for contamination of already emitted particles [94–96].

2.1.4 Main effects of atmospheric particulate matter

Atmospheric particulate matter, or aerosol, has several severe effects both on climate and human health [10–14, 25, 26]. The harmful effects of atmospheric particulate matter on human health are well known and the World Health Organization (WHO) estimated in more than two millions the deaths by year due to atmospheric pollution and particulate [25]. Health risks for humans derive by direct inhalation of aerosols, which can contains several very toxic and carcinogenic compounds. Particles enter the first respiratory system inducing transitory respiratory problems: inflammations, allergies, reduction of the respiratory capability and bronchitis [20,21]. Particle whose size is less the few micrometers can enter the secondary respiratory system (bronchi and alveoli). Such particles are responsible of acute diseases such as chronic asthma, emphysema and lung cancer [21, 22].

Toxic compounds and finer particles (nanometric scale) can enter the blood stream generating cardiovascular diseases, cancer and intoxication [21, 23, 24]. Among all the highly toxic organic compounds commonly found in the aerosol, both in bulk and absorbed forms, there are: *polycyclic aromatic hydrocarbons* (PAHs), and organoclorine compound including *polyclorinated biphenyls* (PCBs). These compounds are produced in the incomplete combustion of fossil fuels, biomass and organic materials (combustion engines, industrial activities and petroleum refineries) [7, 97] and, subsequently, they are absorbed on other particles produced in the same activities. Thanks to the atmospheric matter transport processes these compounds have been detected in significant amount also in remote region of the earth (arctic snows, seawater), where no one of their sources is present [98]. In particular, PAHs are extremely toxic and their mutagenic and carcinogenic properties have been proved even at very low concentrations. These compounds are easily absorbed by mammals and accumulate in their tissues (especially the fat ones) [97, 99]. Thus, they can enter in human body directly or indirectly by ingestion of meat.

Regarding the climate it is possible to distinguish between direct and indirect effects: atmosphere radiative forcing, cloud formation, snow and glacial melting are only few of them [9]. It is well known how part of the atmospheric particulate matter is characterized by having an high absorption coefficient in the solar spectrum (300 nm $\sim$ 2500 nm) [100]. Thus, particulate suspended in the atmosphere absorbs electromagnetic energy from the solar radiation and transform it in heat. This increases the temperature of the surrounding atmosphere and, at the same time, reduces the amount of light reaching the earth surface [101]. The consequences of such a phenomenon, called *atmosphere radiative forcing*, are manifold: changing in the atmospheric temperature and humidity, modification of cloud formation and lifetime and, as consequence, indirect effects on the precipitation amount [102, 103]. Particles suspended in the atmosphere, independently from their absorption coefficient, are actively involved in the humidity nucleation process which stand at the basis of cloud formation and evolution [104]. Moreover, the effects are enhanced by the absorption of the indirect radiation reflected

back by the earth [12].

There are also indirect radiative forcing effects on the atmosphere. It is well known how clouds have a negative forcing effect due to the high scattering of incident solar radiation towards the space. Thus, cloud reduce the amount of radiation reaching the earth surface and absorbed by the atmosphere [105, 106]. The presence of aerosols in the atmosphere directly affects the reflectivity of clouds and change their lifetime and distribution [107, 108]. Therefore, the presence of aerosols indirectly affects the amount of light scattered by clouds providing a secondary climate forcing that is still not well understood and quantified [109].

Acidification of rainwater is another effect of atmospheric particulate matter. Even though this problem has been partially contrasted by the introduction of restrictions on the quality of fossil fuels, till nowadays, sulfuric and nitric acids are present in variable concentrations in rainwater, especially in very polluted urban and industrial areas. Other types of acids have also been detected in rain samples (formic and acetic acids) [110].

Atmospheric aerosol, according to its size, has a lifetime from few hours, for particles greater than 10 μm, to several weeks for nanometric ones. Part of it interacts chemically or mechanically in the atmosphere in several, still not well known, processes creating secondary particulate [90], or depositing on the earth surface at distances from the source that can be very large. This deposition has the secondary effect to reduce the reflective index of snow and ice surfaces (which is normally high) with the consequence of increasing ice melting process with indirect effects on the climate [15–19].

Other effect to be mentioned is the direct reduction of visibility due to the absorption and scattering of light, especially when it is accumulated in the lowest layer of the atmosphere [111–113]. In some specific weather conditions (stagnant air with no wind or precipitations) the concentration of aerosol can increase at so high levels to dramatically affect the visibility also at short distances. In many industrial cities, this situation is not rare and occurs quite frequently [114].

Many other effects, not here included for brevity, are known to be dependent on the aerosol presence in the atmosphere, and many of them are still not well understood. In order to increase the understanding of all these processes and mitigate their effects it is of paramount importance acquiring reliable information on the particulate properties, lifetime, transport and geographical distribution, and this requires an intense and widespread monitoring of the atmospheric particulate matter.

2.2 Metering techniques for the atmospheric particulate matter

Nowadays, there are several different approaches employed for detecting the presence of atmospheric particulate matter and to measure its concentration or its properties. According to the specific application and to the environment, a proper approach

should be adopted in order to achieve reliable and accurate results. In fact, several interferents and artifacts, which in general depends on the application and the specific measurement setup, can affect a particulate measurement. The following sections provide a brief description of some basic equipment and measurement approach typical employed in the particulate detection.

2.2.1 Size segregation of aerosols

As described in the previous sections, effects of atmospheric particulate matter depends of several of properties and especially on its size (equivalent aerodynamic size, section 2.1.1). Thus, it is very important that the monitoring systems are selective in size. Unfortunately, many approaches cannot discriminate particles by their size (gravimetric method, etc.). In such cases, it is required to employ some tool able to filter the input particles by size allowing only a specific size range to reach the measuring system. Such a process is called *segregation* and it is performed by *size filters* which exploit the aerodynamic behavior of particles to select them. Most common tools are: *impactors* and *cyclone filters* [7,115]. In general, a segregation filter allows the particles which size is lower than a specified size to pass, cutting out the others. The critical size for which the filter reaches a 50% of efficiency is called *upper cutpoint*. Instead, the *slew rate* of the profile determines the filter selectivity.

Impactors are the reference segregation tools usually employed in the governmental regulations. Classic impactors are shown in figure 2.1-A. A controlled flux of air is forced in the inlet which conduces to a well chamber. On the well bottom there is a porous filter, maintained wet by a non-volatile oil (or other sticky surfaces con be used). Coarse particles cannot easily deviate their trajectory because of their high inertia. Therefore, such particles impact on the well bottom remaining attached on the wet filter. Fine particles, instead, follow the air flux and go out the impactor reaching the metering system. Some concern exists because of the possible contamination of the sampled particles with the oil [116].

Cyclone filters, shown in figure 2.1-C, exploit the centrifugal force for selecting particles according to their aerodynamic size: coarse particles cannot follow the air flux and are expelled out the filter, while fine particles can reach the outlet. It is possible to design cyclone filters which are more selective than impactors and, in general, they do not present contamination problems [116].

Typical segregation sizes are PM10 and PM2.5. Some problem occurs when it is required to evaluate the particulate in the range PM10 − PM2.5 (particles which size is greater than 2.5 µm but less than 10 µm). In such a case, it is possible to use a *dichotomous sampler* which employs two separate channels, one for PM10 particles and another one for PM2.5 ones. Concentrations are measured separately and the amount of PM10 − PM2.5 is calculated by difference between the two channels: $C_{PM10–2.5} = C_{PM10} - C_{PM2.5}$.

Basically, such a measurement is performed by two different instruments and even

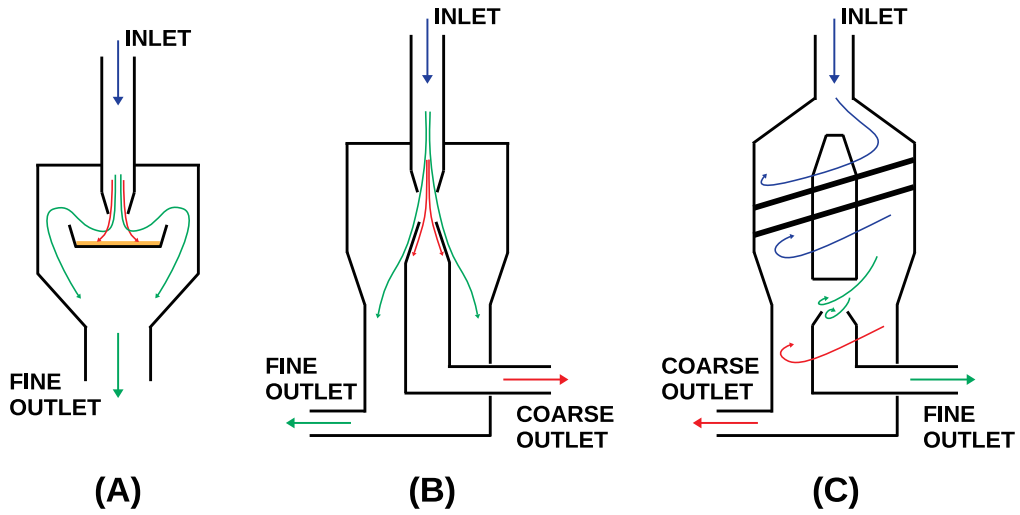

Figure 2.1: Working principle for different types of segregation filters: (A) impactor, (B) virtual impactor, and (C) cyclone filter. Blue arrows refer to the input unfiltered air, green and red ones, respectively, to fine and coarse particle air fluxes.

small differences between them (air flux, humidity, etc.) can generate significant errors in the evaluation of the PM10 − PM2.5 [117].

Multi-stage and virtual impactors can partially alleviate this problem performing the sampling with a single instrument. A multi-stage impactor employs several impactors arranged in cascade which sequentially segregate particles of different sizes.

Virtual impactors, shown in figure 2.1-B, do not have an impacting surface, but a hole. The air flux is forced in the inlet and in a nozzle. Fine particles deviate and follow the main air stream. Coarse particles cannot deviate and are collected in the hole with a secondary air flux. Virtual impactors are not affected by contamination problems, but usually their selectivity is not very high. The selection of the proper segregation filter depends on the application and the measuring method employed.

2.2.2 Sampling filters

Many aerosol measurement methods require the sampling and the accumulation of particulate matter on a sampling medium in order to achieve a suitable sensibility. Porous filters are the most commonly employed sampling medium and, in general, they are characterized by a low cost and a high efficiency. Nowadays, several type of filters are available on-the-shelf: *glass fiber filters*, *quartz fiber filters*, *teflon filters*, *membrane filters* and *polyurethane foams*. They features different characteristics (mesh size, thermal stability, light absorbing spectrum, mechanical strength, differential aerodynamic pressure, loading capability). Therefore, in order to achieve reliable measurements, a

suitable filter type has to be selected and calibrated for each specified application, also considering the post-sampling analysis requirements [118].

Glass fiber filters – Glass fiber filters are the most used, especially with the gravimetric method, and generally the cheapest ones. They are composed by very thin glass fibers compacted together, and optionally bound with an organic binder. They are available with several standard grades of filtration referring to average mesh size and blocking efficiency. Such a type of filters is called *deep filter* because they block the particles both on the surface and in the first layers. They have good mechanical and aerodynamic properties, the higher loading capability, and feature an high thermal stability making them suitable for thermal-optic and thermal-chemical post-sampling analysis. However, they can present several contaminants (especially metals or organic compounds in the binder) which should be considered for chemical analysis.

Quartz fiber filters – Quartz fiber filters are basically identical to the glass fiber filters, but use quartz fibers. They have similar properties but present a wider pass-band spectrum which make them especially suitable for light absorption measurements that include the UV range.

Teflon filters – These filters are produced with fluoroplastic materials, which make them very resistant to organic solvents and acids. They are surface filters capturing the aerosol particles only on their surface, which results very porous with highly controlled mesh size. Such a type of filters has good thermal stability and a low content of contaminants. For these reasons, they are very suitable for chemical analysis, but usually they are more expensive than other filter types.

Membrane filters – These filter can be produced by several materials which are arranged in the form of a very thin and porous membrane. Common materials are based on cellulose compounds and typically they are hydrophobic. Such filters have a low loading capability, but very low content of contaminants.

Polyurethane foams – Even though not so commonly used as sampling medium, polyurethane foam presents good characteristics: large range of porosity, high purity and high loading capability.

2.2.3 Gravimetric methods

The gravimetric method is the measurement approach recommended in most the governmental regulations [28, 29]. It is able to provide accurate measurements on the total amount of particulate within a specific aerodynamic size range (typical ranges are PM10 and PM2.5) averaged along the sampling time. Unfortunately, such a method does neither provide any detailed information on the size distribution of particles nor a real-time amount of particulate. Furthermore, the characterization of aerosol is only partial because such a method, when employed alone, cannot detect any other property such as composition, morphology and light absorption. A schematic gravimetric sampler and conditioning steps are shown in figure 2.2-A. Basically, an air pump generates an accurate air flux. A segregation filter, placed on the head of the sampling system,

cuts off the particle whose size is greater than the specified range. The air flux is forced in the deposition filter which captures the aerosol. The difference of the filter weight before and after the sampling represents the total amount of particles deposited on the filter during the sampling time. Thus, it is possible to calculate the average particulate concentration C_{PM}, usually expressed in $\mu g/m^3$, as:

$$C_{PM} = \frac{W_1 - W_0}{\phi_{air} \cdot t_s} \tag{2.1}$$

where W_0 and W_1 are respectively the filter weight before and after the sampling expressed in μg, ϕ_{air} is the air flux expressed in m^3/min and t_s is the sampling time expressed in minutes.

However, the filter can absorb a significant amount of humidity during the sampling process. Thus, in order to reduce the measurement uncertainty, the filters are conditioned before each weighting for a fixed amount of time with specified environmental conditions (typically 6 h at 20 °C and 50% RH). This turns out in additional costs and possible errors due to the filter transportation.

Such an approach, even though very accurate, results expensive, requires bulky equipment and a preconditioning and a post-sampling analysis in a specialized laboratory. Only after the filter weighting it is possible to employ analytical methods in order to detect chemical composition, size, morphology and absorption coefficient of the deposited particulate.

Some alternatives have been proposed to partially overcome such limitations. They basically try to embed a weighting system inside the sampler in order to achieve a real-time measurement and avoid the expensive and time-consuming conditioning setup.

One possibility is the Tapered Element Oscillating Microbalance (TEOM) [119]. These systems use a sampling surface (it can be a standard sampling filter) oscillating at a specified frequency which is continuously measured by a dedicated electronic front-end. Particles deposit on the surface changing its mass and its inertia. As consequence, the oscillation frequency changes proportionally to the deposited mass. The surface is heated at a specified temperature (typically 50 °C) in order to avoid errors due to condensation of humidity or effects of the environmental temperature.

Unfortunately, this produces the evaporation of semi-volatile compounds present in the aerosol. A possible solution to this problem is employing an oscillating microbalance operating on a filter sandwich: a first teflon filter collects the solid particulate and a second filter, which is coated with charcoal, capture the volatile species [120]. Some other studies report about the employment of quartz microbalances monitoring systems where the particles deposit on a quartz resonator by impact or by thermal/electrostatic precipitation [121]. Another approach is the measurement of pressure drop across the deposition filter, which is function of the filter loading [122].

A different approach is employed by the *beta attenuation meters* [123]. Such instruments measure the attenuation of beta-particles throughout the deposition filter. A block diagram of a beta attenuation sampler working on two particle sizes is reported in

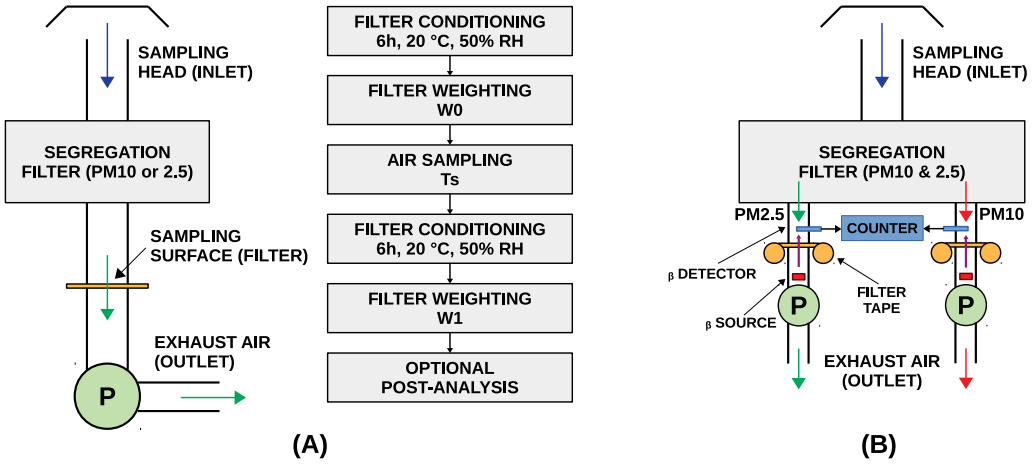

Figure 2.2: (A) Block diagram of a gravimetric particulate sampler and basic steps required to properly conditioning and analyzing the filter. (B) Block diagram of a two-size beta-attenuation meter.

figure 2.2-B. Beta-particle attenuation results proportional to the aerosol mass (or thickness) deposited on the sampling filter. Such a system requires one or more beta-particle sources and the relative particle counters. The method is characterized by an high sensitivity and is able to perform real-time measurements using filter tapes. However, it still suffer by the humidity interferent and the equipment is very expensive.

In general, all the gravimetric alternative methods suffer of a reduced accuracy in respect to the reference method due to the effects of the atmospheric humidity and the evaporation of the volatile compounds when an heating is employed to reduce the humidity effects.

2.2.4 Alternative measurement approaches

Several other techniques are, nowadays, available for the detection of atmospheric particulate matter. Most of them are based on optical approaches and, in particular, on particle light scattering and absorption.

A very accurate method is the photoacoustic spectroscopy which allows one to measure the light absorption coefficient of aerosols with high sensitivity and accuracy. The photoacoustic effect is based on the generation of acoustic waves when particles are heated by a modulated light source. In order to make the measurement insensible to external noise and vibrations, the system is mounted inside an acoustic resonator which is tuned on a specific frequency. Figure 2.3-A shows a simplified block diagram of such a device. A laser modulated at the resonance frequency is employed as light source. Aerosol particles, when struck by the laser beam, heat because the absorption of incident light. Hot particles transmit such an heat to the surrounding air which expand

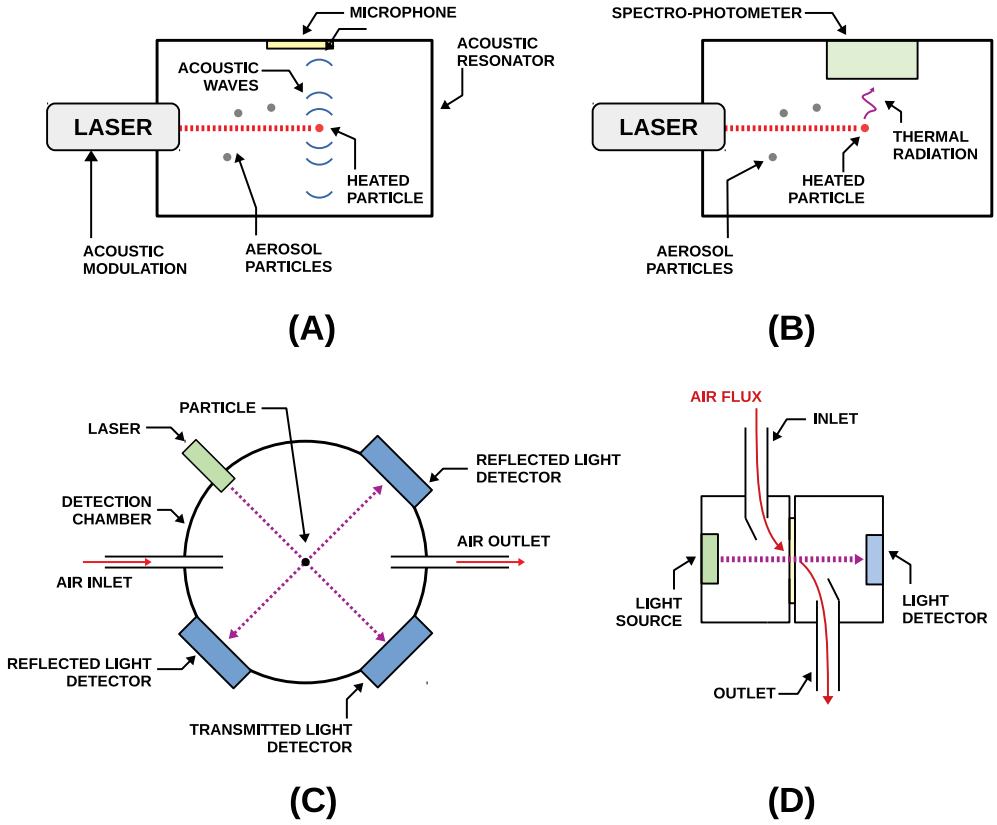

Figure 2.3: (A) Photoacoustic detector. (B) Incandescent particle detector. (C) Laser-scattering detector. (D) Aethalometer.

accordingly, generating acoustic waves at the laser modulation frequency, whose amplitude is related to their light absorption coefficient. A microphone, placed inside the resonator, is employed to detect such acoustic waves. Another similar approach is based on the measurement of the refractive index of air surrounding the heated particles by means of an interferometer.

Another technique, shown in figure 2.3-B, is the incandescence spectroscopy which is especially useful in case of high-absorbing aerosols composed by refractory carbonaceous compounds. A high-power laser is used to heat the particles at temperatures as high as they start to emit thermal radiation in the visible spectrum. A spectrophotometer is employed to detect such a thermal radiation and, from it, to evaluate the light absorption coefficient and also the aerosol mass.

Unfortunately, all these approaches employ very expensive equipment and they are not practical in low-cost applications. An alternative to such methods, which is characterized by lower cost, is the laser-scattering particle counter. Figure 2.3-C shows a schematic diagram of such a device. Particles are forced to flow inside the detection

chamber, where there are a low-power laser and several light detectors. One detector is placed in-line with the laser beam in order to detect the transmitted light. One or more other detector are placed around the chamber for detecting the scattered light. When a particle crosses the laser beam, an attenuation of transmitted light is detected by the first detector. At the same time, part of the incident light is scattered back by the particle and detected by the other detectors. Therefore, each particle is counted by revealing the peaks of the detector output signals. Moreover, by measuring the peak duration it is possible to achieve information on the particle size. Such a method is quite simple and does not require any expensive equipment. Unfortunately, several are the uncertainty sources for this method. As an example, particle dimension is affected by large uncertainty: such a measurement depends on how light hits the particle and on the surface characteristics.

Eventually, aethalometers are instruments able to provide reliable results at a quite low cost. Such instruments employ a sampling filters for capturing the aerosol particles. Then, aerosol light absorption coefficient is measured by evaluating the light attenuation across the loaded filter, as shown in figure 2.3-D. Main advantages of such an approach are: high-sensitivity due to the accumulation on the filter, real-time measurement, quite low-cost and the possibility to miniaturize the instrument. However, sometimes these instruments feature a poor accuracy which depends on the environmental parameters and on the particulate type itself. For such reasons, aethalometers typically requires periodic calibrations. Moreover, they are not able to provide any information of the particle size.

There are several other approaches which can be employed for the detection of the atmospheric particulate matter. Unfortunately, such approaches have always significant drawbacks, or they are able to provide only a partial characterization of the aerosol. Therefore, the development of new measurement approaches in this field is mandatory in order to assess the effective health risk of people and, at the same time, to improve the knowledge about the atmospheric particulate matter.

Chapter 3

A novel camera-based approach for real-time monitoring of atmospheric aerosol

This chapter partially contains materials from previously published works of the author [1–4]

As explained in detail in chapter 2, atmospheric particulate matter is a complex mixture of particles suspended in the atmosphere. Such particles, produced at different levels both by human activities and natural processes, are responsible of several different effects both on human health and climate. In particular, aerosol effects on human health can be very severe, according to particle type, chemical composition, size and concentration. Transitory diseases of the respiratory system as well as lung cancer and cardiovascular diseases have been correlated with high concentration of atmospheric particulate matter.

Zones characterized by high concentration of particulate are surely large cities and industrial areas, where there are large emissions of such dangerous particles due to the widespread combustion of fossil fuels. Unfortunately, such areas are also the ones featuring the highest population density. Therefore, in such areas the problems connected with the presence of the particulate are extremely critical and an effective monitoring of the aerosol is mandatory in order to assure safe conditions for people. Furthermore, in cities, the concentration of atmospheric particulate matter is quite variable with time and space due to the local weather conditions, such as ventilation, or to the presence of local emissions. Therefore, a capillary monitoring is required with many sampling points spread on all the territory, especially in the more populated areas. In such an application, the establishment of a wireless sensor network featuring many small low-cost particulate monitoring systems distributed on the territory would be extremely beneficial. Unfortunately, even thought several approaches are available for monitoring the concentration of aerosol in the atmosphere (gravimetric methods, photoacustic

detecton, particle counters, just to cite few of them) they usually employ quite expensive and bulky devices with cost that can be in the order of several thousand dollars for each single sampling point. Moreover, such methods typically provide only partial information on specific characteristics of the particulate, such as concentration and light absorption coefficient, and often they are not able to provide a real-time measurement. This severely limits their employment of such an application.

With the aim to partially solve the several drawbacks of available approaches, a novel optical method for the detection of the atmospheric particulate matter, based on a low-cost digital camera and standard glass fibre sampling filters, was developed and some prototypes employing such method were realized and tested with several measurement campaigns. Next section will describe in details the proposed approach and the realized prototypes. Eventually, section 3.2 describes the characterizations performed in order to validate the proposed approach.

3.1 The proposed monitoring system and the analysis software

Several are the measuring approaches employed nowadays for the detection and the monitoring of the atmospheric particulate matter. Unfortunately, they present several limitations and employ quite expensive equipment. For such reasons a capillary monitoring of particulate over large areas is still a challenging issue.

A new detection approach is, therefore, proposed with the aim to partially overcome the discussed limitations. The new approach employs a standard glass fibre filter for sampling the air and capturing the aerosol particles. A low-cost high-resolution digital camera takes pictures of the filter surface and a dedicated detection software provides to detect the single particles and to estimate their equivalent size in order to evaluate the total amount of particulate and its size distribution.

Section 3.1.1 describes the structure and the working principle of the realized prototypes providing details on their implementation. Eventually, achieved results are discussed in section 3.2.

3.1.1 The monitoring system

The proposed sampling system employs a sampling mechanism which is similar to the one employed by the standard gravimetric method, but with a quite different detection approach based on the optical detection of the single captured particles by means of a digital camera. Figure 3.1 shows the basic diagram of the proposed system.

An air pumping system is employed to force a known air flux through a glass fibre filter. External air enters from a inlet tube (sampling head) and goes in the inlet sampling chamber and, from it, directly through the sampling filter. Aerosol particles suspended in the air are captured on the filter surface. The flux is generated by means of a small DC

pump connected downstream to the outlet sampling chamber. Such a placement avoids any possible contamination of the sampled air. Eventually, exhausted air goes out from the outlet tube. The pump is controlled by a power interface and a controlling system so as to force an accurate flux of air through the sampling filter. Such a flux can be, therefore, changed according to the specific application and the pollution level. In particular, a low rate pumping is employed in high polluted areas in order to avoid a quick filter saturation. Instead, higher pumping rates are required when the pollution level is low so that the system can achieve a suitable sensitivity. A dedicated backlighting system is hosted in the outlet sampling chamber. Such a system illuminates the sampling filter so that the digital camera, placed in the inlet chamber, is able to take high-resolution pictures of the sampling filter surface. In such a condition, the captured particles appear as small dark spots over the bright filter surface. In order to achieve a suitable magnification and resolution of the filter surface, a macro lens with a magnification of 20x was mounted together with the digital camera by means of an holding structure which allows one to focus the filter by adjusting the lens-to-camera distance. The backlighting system is composed by five LEDs featuring different wavelengths from the IR to the UV spectrum: 940 nm/880 nm, 625 nm, 528 nm, 470 nm and 375 nm (with the red, green and blue wavelengths implemented by using a single RBG LED). Such LEDs can be individually controlled in order to obtain a proper illumination of the filter. In fact, the light transmission coefficient of the aerosol particles depends by the chemical composition and the surface morphology of the particles themselves. Therefore, by properly selecting the backlighting wavelength, it is possible to retrieve additional information of the particulate type. All the processing and control are performed by a RaspberryPI board (model ZeroW). This small computer-on-single-board has dimensions of about 65 mm × 30 mm and employs a ARM 32-bit processor with 512 MB of RAM. A small real-time microcontroller (Teensy 3.2) was added to the system in order to perform low-level operations such as motor and LED control. The RaspberryPI ZeroW features also a Bluetooth 4.0 a WiFi connectivity so that the system can be easily interfaced to the Internet or to any Bluetooth-capable device, such as smartphones and laptops. A small low-power LoRa module (RF Solution, model: RF-LORA-868-SO) is connected to the controller in order to add a long-range wireless connectivity to the monitoring system so that it is possible to easily establish a long-range sensor network for monitoring the atmospheric particulate matter. Eventually, the system is able to work for short time periods also without an external power supply (blackouts) thanks to a LiPo rechargeable battery.

A RaspberryPI Camera NoIR, Version 2 was selected as detection camera because of its good performance and the possibility to connect it directly to the RaspberryPI. Such a camera features a resolution of 3280 px × 2464 px, and a quite wide optical spectrum which makes possible to get pictures from the near-IR to the near-UV spectrum.

A dedicated software, written in Python, runs on the RaspberryPI and provides control to the main functions of the system. Moreover, by using the OpenCV library, such a software is able to process the camera pictures and detecting the captured particles

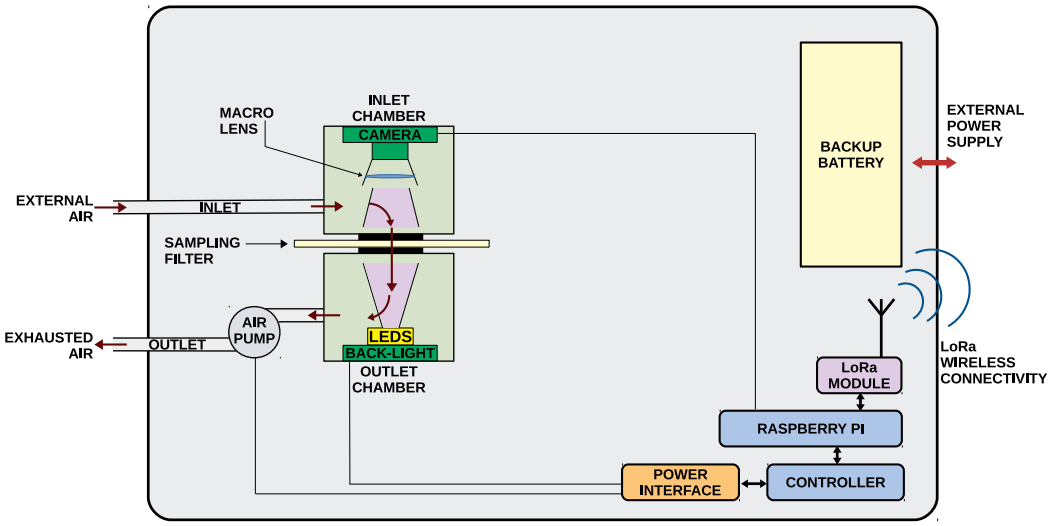

Figure 3.1: Basic diagram of the proposed system.

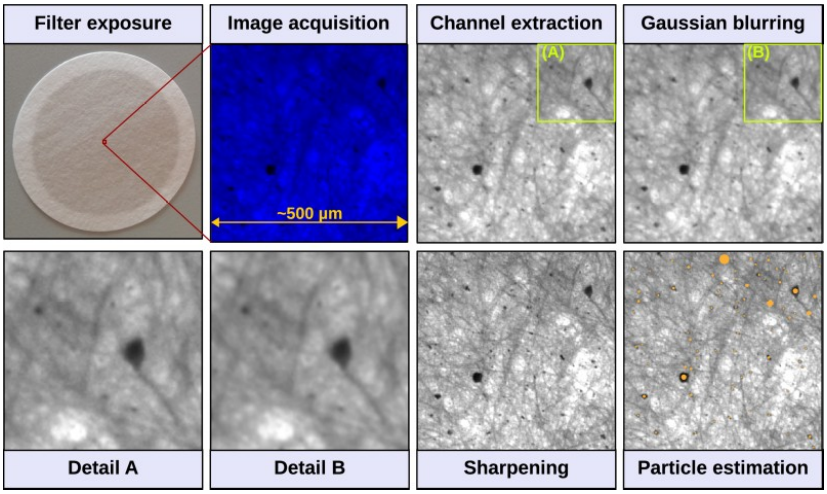

Figure 3.2: Measurement and image processing steps: filter exposure, image acquisition, channel extraction, selective gaussian blurring, sharpening and particle detection. Details (A) and (B) highlight the blurring effect on the filter fibers.

by means of a blob detection algorithm.

The measurement steps performed by the software are schematically shown in figure 3.2. The filter is firstly exposed by sampling a known volume of external air. The control system allows one to set a specified air flux by adjusting the supply of the pump.

If ϕ_a is the selected air flux and t_s is the sampling time, the total volume of air sampled through the filter is:

$$V_a = \phi_a \cdot t_s \tag{3.1}$$

Aerosol particles suspended in the sampled air are captured by the filter. After the exposure it is clearly visible the change in color of the filter. Periodically, the backlighting system is enabled and a specific wavelength is selected by turning on the correspondent LED. The digital camera takes pictures of the filter surface that are acquired by the RaspberryPI board using the Camera Serial Interface (CSI). The detection software performs several image processing in order to enhance the contrast of the particle spots and increase their sharpness. The original camera image is decomposed in its RGB channels and, subsequently, it is converted in a gray-scale mode by selecting the most appropriate channel according to the selected backlighting wavelength. As an example, if the picture is taken with a red backlighting, the red channel is selected. Table 3.1 reports the selected channel for each of the available wavelengths. Subsequently, a selective gaussian blurring is applied to the whole image with the aim to reduce the effects of the filter fibers. Such a selective blurring acts selectively preserving the contours of the spots and slightly blurring the other parts of the image. The blurring effect can be observed in the figure 3.2, details (A) and (B). Then, a sharpening of the image is performed by applying to the image a 2D kernel filter. The selected kernel is a 5×5 matrix defined as:

$$K = \begin{bmatrix} K_0 & K_0 & K_0 & K_0 & K_0 \\ K_0 & K_1 & K_1 & K_1 & K_0 \\ K_0 & K_1 & K_2 & K_1 & K_0 \\ K_0 & K_1 & K_1 & K_1 & K_0 \\ K_0 & K_0 & K_0 & K_0 & K_0 \end{bmatrix} \tag{3.2}$$

being K_0, K_1 and K_2 the three kernel parameters determining the amount of sharpening performed on the image. Eventually, the blob detection algorithm is applied to the image in order to detect the single spots due to the captured particles. Such an algorithm, implemented in the OpenCV library, is based on binary matching at progressive thresholds. This algorithm is quite flexible and features several filters which allows one to select the blobs according to their shape, size, and color. The application of the blob detection results in a list of detected particles with the associated equivalent size. Such detected blobs are mapped on the original image and are employed to evaluate the particulate size distribution by means of an histogram.

The total amount of particulate can be, therefore, calculated by considering the total exposed area of the filter A_{ex} and the effective analyzed image area A_{ef}. A_{ex} depends on the mechanical system holding the filter during the air sampling and acting as a mask. A_{ef}, instead, depends on the effective area of the captured image that is analyzed by the detection software. In fact, the original image taken by the camera is cropped slightly

in order to eliminate the border distortions introduced by the additional macro lens. Therefore:

$$A_{ef} = X \cdot Y \cdot r^2 \tag{3.3}$$

where r is the effective camera resolution expressed in μm/pixel, X and Y are the dimensions in pixel of the analyzed image. Thus, the effective sampled air volume is given by:

$$V_{ef} = V_a \frac{A_{ef}}{A_{ex}} \tag{3.4}$$

Taking in consideration that the mass of an aerosol particle can be expressed as:

$$m_p = \gamma \frac{\pi}{6} \cdot d^3 \tag{3.5}$$

where d is the equivalent size of the particle (diameter) and γ its density which is usually assumed equal to 1 kg/dm^3. Therefore, it is possible to estimate the total particulate amount C_P in the range between d_{min} to d_{max} as:

$$C_P = \frac{\sum_{d_{min}}^{d_{max}} m_x \cdot N_x}{V_{ef}} \tag{3.6}$$

where m_x is the mass of one particle of size x and N_x is the number of captured particles whose size is x.

Of course, such an approach has several limitations. Among them there is surely the effect of the filter mesh size: the blocking efficiency of the filter depends on the average mesh size and, therefore, only particle whose size is larger than the mesh size are effectively captured by the filter. This involves a limitation on the detectable size range of particulate. Furthermore, very small particles cannot be detected by the camera because of the limited effective resolution achieved by the optical system. In the performed tests, a GF10 glass fibre filter was used with an average mesh size of about 3 μm which result compatible with the effective resolution of the camera system which was estimated in 1.25 μm/pixel. Therefore, the realized prototypes cannot detect particles with size lower than about 3 μm. Another possible issue which can occur is the overlapping of particles during the sampling process. In fact, when two or more particles are captured very close one to the other, the optical system is not able to distinguish among them and an error both in terms of total particulate amount and of size distribution is, therefore, committed. In order to minimize such an issue, the filter should be replaced when its coverage starts to be significant. In such a way, the probability of particle overlapping is reduced to negligible values. In the performed tests, the maximum coverage was limited to 2% $\sim$ 5% of the total exposed filter area.

Eventually, another different approach can be implemented with the same hardware with virtually no additional cost. In particular, the camera can be employed as light

Table 3.1: Channel selection according to the backlighting wavelength.

Wavelength	Selected RGB channel
IR (940 nm/880 nm)	RED CHANNEL
RED (625 nm)	RED CHANNEL
GREEN (528 nm)	GREEN CHANNEL
BLUE (470 nm)	BLUE CHANNEL
UV (375 nm)	BLUE CHANNEL

sensor for implementing a sensing approach that is similar to the one of aethalometers. In fact, the global light absorption coefficient can be calculated from the difference of the light transmitted through the filter before and after the air sampling. This might be useful to taking into account the part of captured particles which cannot be detected because their size is under the resolution of the optical camera system.

The first realized prototype employs a manual filter management system. Such a prototype is characterized by an very small dimension of about 100 mm × 100 mm × 60 mm. The prototype, shown in figure 3.3, is enclosed inside a small plastic box and almost all its mechanical parts were printed by means of a 3D printer. In such a system, whose block diagram is shown in figure 3.4, air sampling and filter image processing are performed in two separate stages called *sampling stage* and *analysis stage*. Initially, the filter is mounted in the sampling chamber where aerosol particles are captured for a specified amount of time thanks to the pumping system described above. Subsequently, the filter is manually moved to the analysis chamber where the digital camera provides to take filter pictures. Thus, the system is not able to perform a real-time monitoring but, thanks to the removal of mechanical parts and motors required for an automatic filter management, such a system features very small size and power consumption, characteristics very important in portable applications.

A second prototype was subsequently realized in order to add a semi-automatic filter management. Figures 3.5 and 3.6, respectively, show the prototype and its block diagram. In such a prototype three motors were added in order to enable an automatic change of the filter measurement spot when it becomes saturated by the captured particles. The mobile filter holder features seven measurement spots and it is connected to a stepper motor which accurately moves it with the aid of an optical alignment system employed to keep track of the holder position. Two small servo motors were also added to inlet and outlet sampling chambers in order to move the chambers up and down. Such a way, when the measurement spot needs to be changed the servo motors open the sampling chamber to allow the filter holder to move properly. When the new spot has been aligned the sampling chamber are again closed to seal the air path by means of small o-rings. This way, any possible lack of air is avoided. All motors are controlled by the real-time controller through the power interface. This semi-automatic prototype features an identical optical camera system but, in respect to the first prototype,

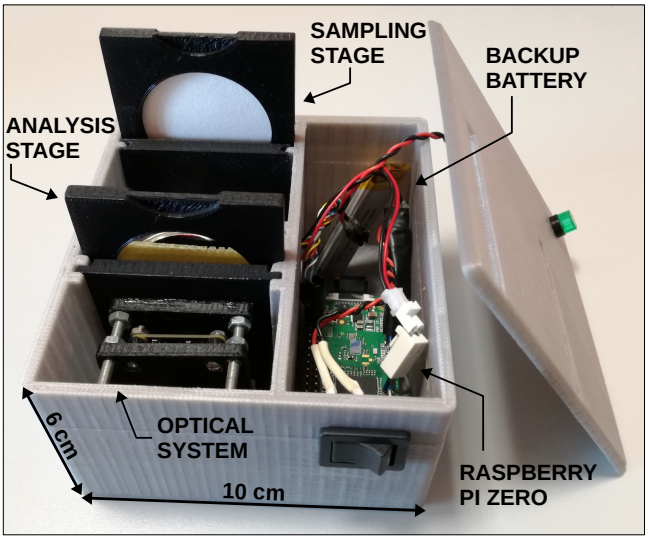

Figure 3.3: First prototype employing a manual filter management.

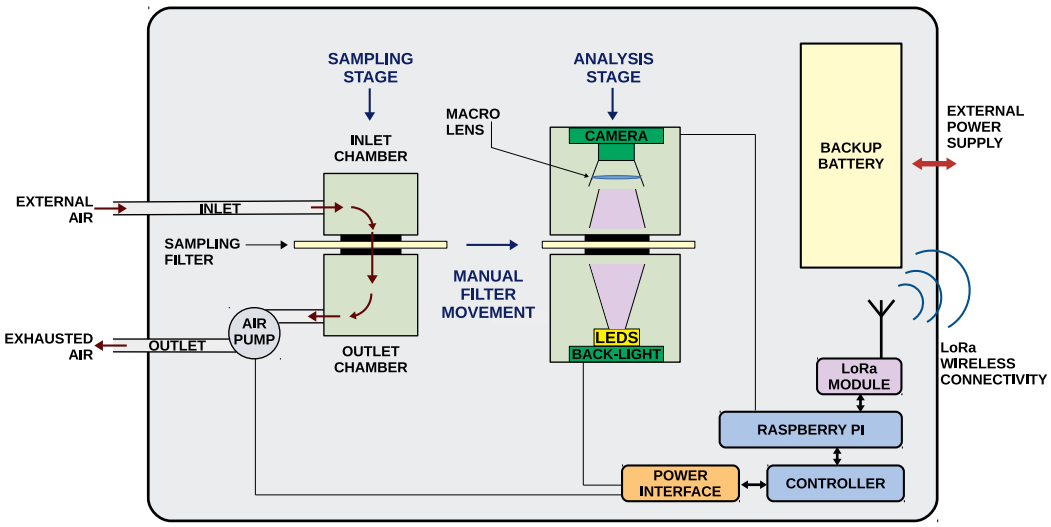

Figure 3.4: Basic diagram of the first prototype.

it allows one to perform measurement for approximately one week (one measurement spot per day). Of course, the several motors employed to move the mechanical parts increases system size and its power consumption, making it less suitable for portable applications.

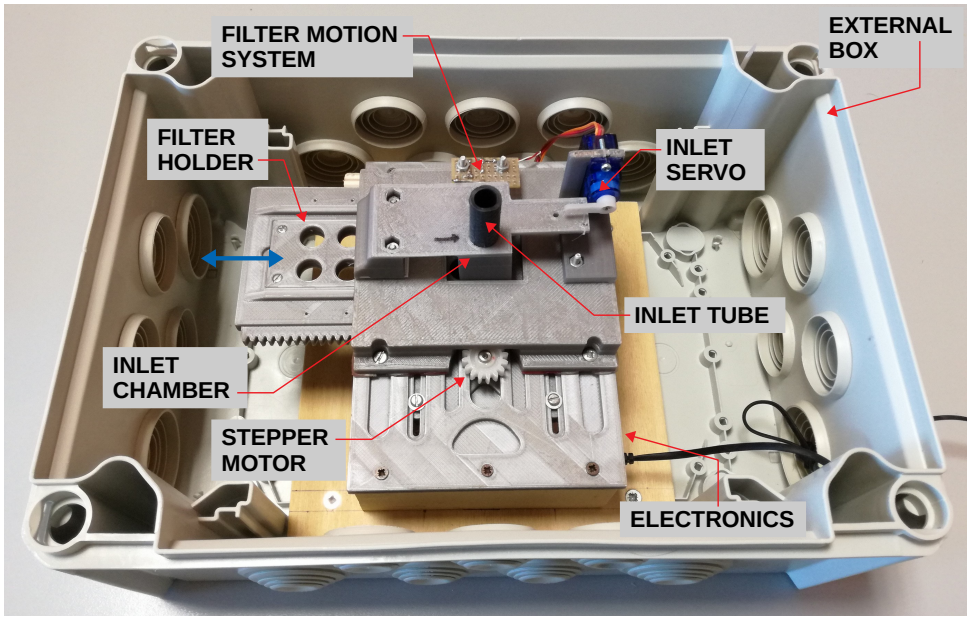

Figure 3.5: New prototype employing an automatic filter management.

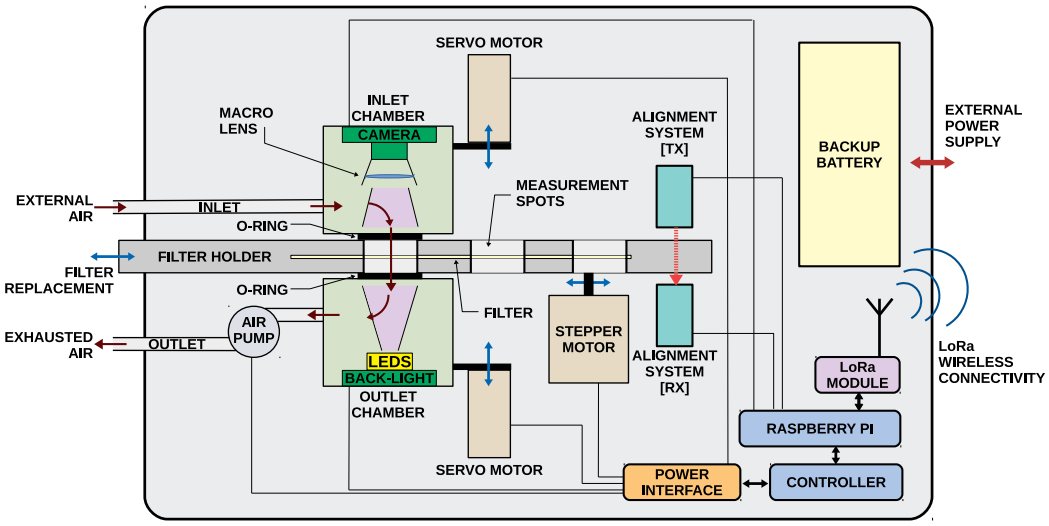

Figure 3.6: Basic diagram of the new prototype.

Eventually, a third prototype was developed and realized which employs a similar approach but allows one to perform continuous measurement for months. In such a

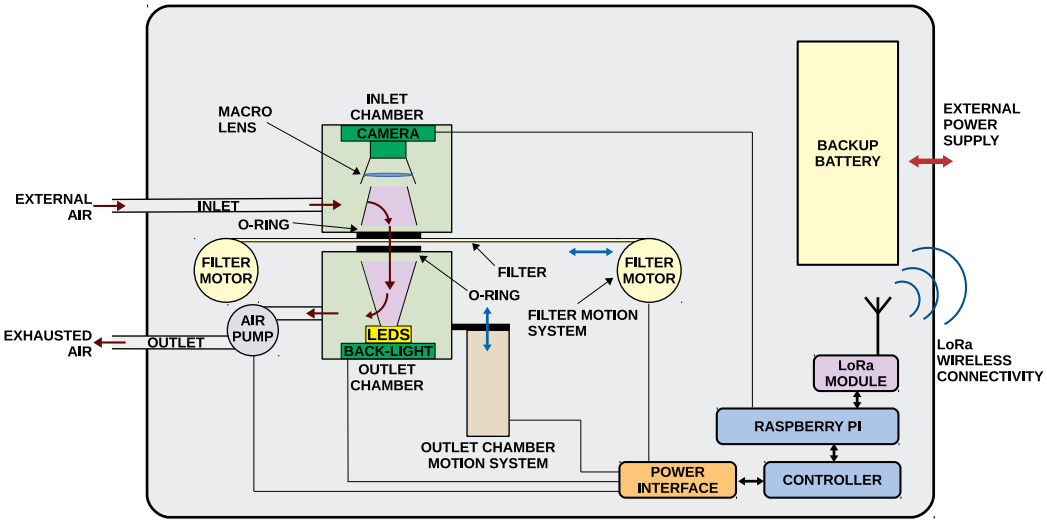

Figure 3.7: Basic diagram of the fully automatic prototype.

prototype the filter holder was replaced with a filter tape roll connected to the stepper motor. The filter tape roll features a total length of 30 m which is enough to provide up to 1000 measurement spots. The working principle is similar to the previous prototype: when a measurement spot becomes saturated the sampling chamber opens by means of a servo motor, the stepper motor connected to the filter tape roll moves the filter to the next measurement spot and, subsequently, the chamber is again closed. Such prototype, whose block diagram is shown in figure 3.7, is able to operate without any external intervention for months taking track in real-time of the particulate concentration.

3.2 Validation of the proposed system

The proposed system was characterized by several different tests. In particular, preliminary characterizations were performed on the principal components such as the air pump, employed to sample a known volume of air, and the optical system, employed for detecting the captured particles on the filter surface. Such preliminary tests were carried out before assembling the system prototype in order to both confirm the feasibility of the proposed optical approach and calibrate pump air flux and effective camera resolution.

Two different air pumps were selected because of their small size, low power consumption and low cost. Both pumps were characterized in terms of air flux generated as function of the supply voltage. During such a measurement, each pump was mounted

Table 3.2: First-order coefficients employed to control the air flux together with maximum air flux and power consumption for both pumps #1 and #2.

Pump	a (l/minV)	b (l/min)	Max air flux (l/min)	Max Power (W)
#1	1.17	-2.22	7	0.5
#2	4	-6.37	24	1.6

together with the main components of the air sampling system: collection chamber, test filter, connection tubes, inlet and outlet, as shown in figure 3.8. In fact, such elements introduce aerodynamic loads in the air flux and, as consequence, they change the effective air flux generated by the pump. A flowmeter (BROOKS INSTRUMENTS, series: 3000) was connected at the exhausted air outlet in order to measure the actual air flow generated by the pump. The pump was connected to a power supply and the air flux was measured at several voltage steps in the range of 0 V to about 8 V.

Figure 3.9 shows the calibration curves obtained in such a test. It is possible to note how both pumps have a linear trend which make quite easy an accurate control of the air flux. Pump #1 is quite smaller having a size of about 40 mm × 30 mm × 20 mm with a maximum power consumption of 0.5 W when powered at 8 V. Such a pump is characterized by a maximum air flux of about 7 l/min. Pump #2, instead, is bigger with dimensions of about 60 mm × 30 mm × 30 mm and it is able to generate a maximum air flux of 24 l/min with a power consumption of about 1.6 W at a supply voltage of 8 V.

Pump #1 is suitable in high-polluted environments where, usually, a low air flux is required in order to avoid a quick saturation of the filter. Pump #2, instead, is more suitable in environments where there is a low concentration of atmospheric particulate matter and, therefore, a higher air flux is required in order to achieve an acceptable sensitivity. Table 3.2 reports characteristics of the two pumps and the first-order coefficients which were stored within the air flux control software (RaspberryPI) by means of the following formula:

$$\phi_a = aV_{supply} + b \tag{3.7}$$

where a and b are the first-order coefficients and V_{supply} is the supply voltage powering the pump.

Next characterization was instead performed with the digital camera (RaspberryPI Camera, Version 2.0) together with the selected macro lens. A grid, subdivided in 1 mm units, was printed on a paper sheet. Photo of such a grid were taken with the camera and analyzed in order to evaluate the effective camera resolution. Such a resolution, which includes the magnification effects of the macro lens, was evaluated by counting the number of pixels within one unit and dividing by the length of one unit. This operation was performed on several squares and it resulted an average number of 1254 pixels per unit. Therefore, the optical system is able to achieve an effective resolution on the filter

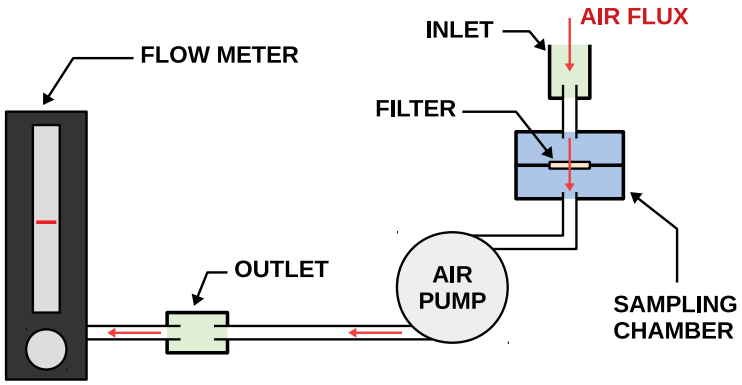

Figure 3.8: Block diagram of the measurement setup employed for characterizing the air pumps.

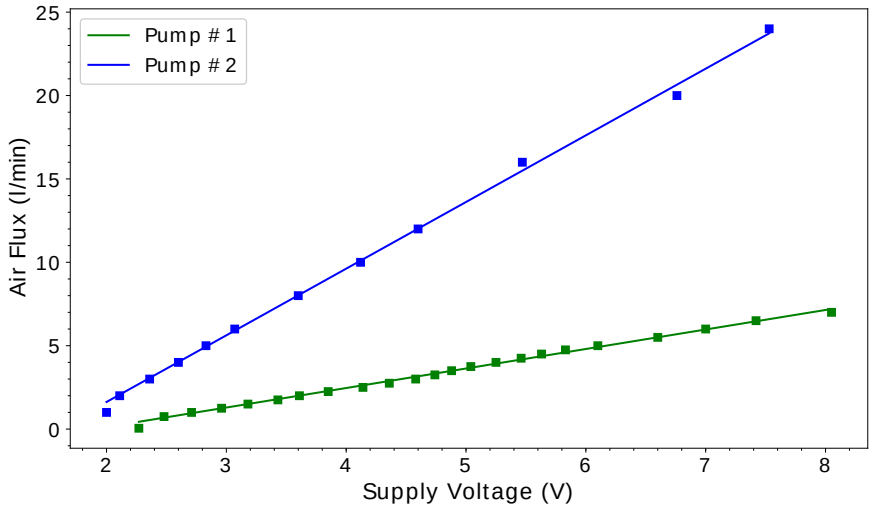

Figure 3.9: Calibration curves for the pumps employed in the monitoring system.

surface of about 1.25 pixel/µm. Such a value is expected to slightly change of about 5% because the uncertainty of the printed grid and the slightly different focal length required for the five backlighting wavelengths.

Subsequently, a simplified sampling system was assembled by using a manual filter loading system. By using this setup, several air samples were acquired in a polluted environment (city of Turin, North of Italy) with the aim of assessing the filter capability in terms of efficiency in capturing aerosol particles. As an example, figure 3.11 shows the glass fibre filter before and after an exposition of 24 h with an air flux of about 1 l/min. It is clearly visible the difference in color of the exposed surface due to the

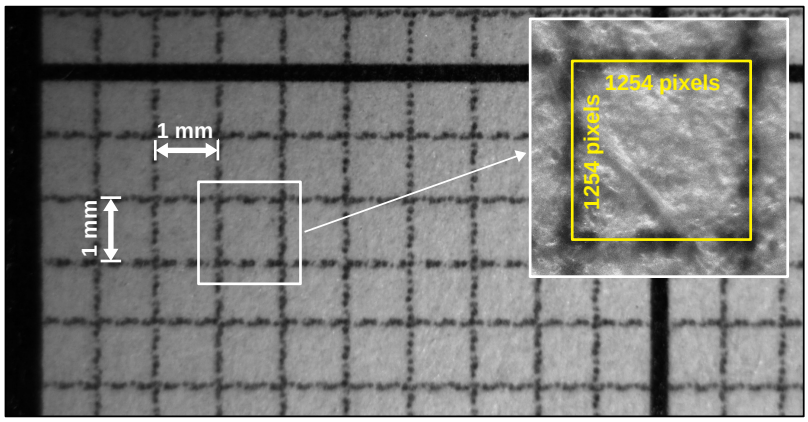

Figure 3.10: Photo of the calibration grid taken by the digital camera together the macro lens and detail of 1 mm × 1 mm square.

particles captured on the filter surface. Other similar samplings were carried out in different zones of Turin and in the small village of Spadafora (Sicily, South of Italy).

The exposed filters were subsequently analyzed by means of a field-emission electron scanning microscope (ZEISS, model: Supra 40). Such a characterization allowed one to assess the typical morphology and dimension of the captured aerosol particles. As an example, figure 3.12 shows some of them, identified by a progressive number.

Energy Dispersive X-ray Spectrometry (EDS) was caried out on selected filters with the aim to detect the main chemical elements composing the particles. Such an analysis revealed a very heterogeneous composition of the sampled particles.

In particular, first two pictures were taken on filters exposed in Spadafora, and all the others on filters exposed in Turin. Spadafora, is a small village in Sicily, South of Italy. The sampling system was placed at few hundreds meters form the sea, in proximity with an highly busy road. First picture puts in evidence a conglomerate of small particles (2) whose size is less than 1 µm. Considering the undefined shape of such a conglomerate and the dispersion of particles which result partially attached on the filter fibers, it can be thought that this conglomerate grew up on the filter surface during the sampling. This situation is not rare, and several studies highlight how atmospheric particulate matter is subjected to modification after it deposits on such a kind of filters. In the same picture there is also a salt crystal (1), due to the marine environment, which was partially included in the conglomerate. The second image shows, instead, a quite large carbonaceous particle (4) and an organic particle (3) which is probably a pollen. Both particles have size of about 20 µm.

Sampling in Turin was carried out in a street in proximity of a train station. Here,

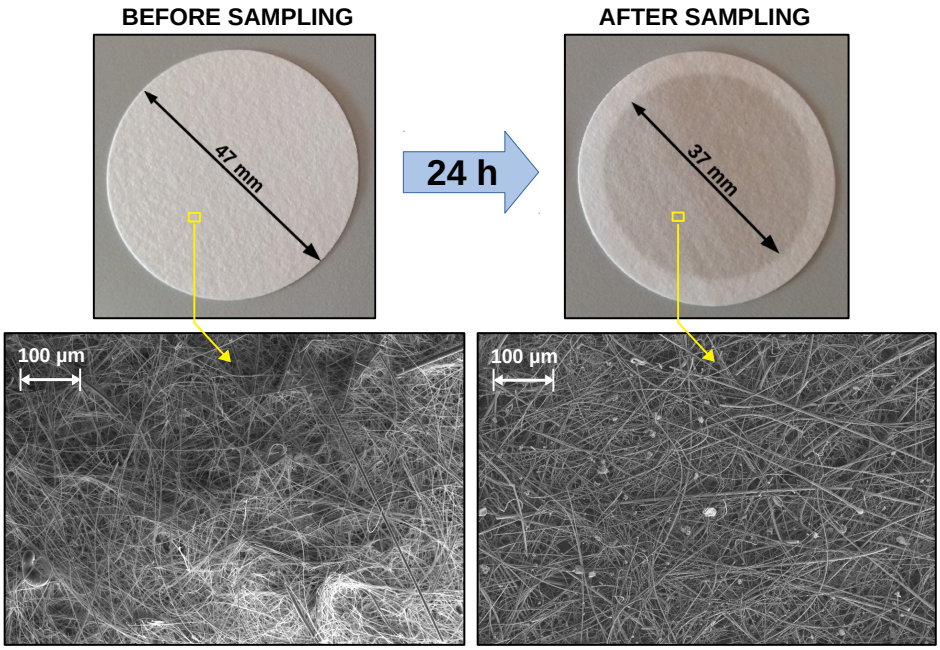

Figure 3.11: Glass fibre filter before and after an exposure of 24 h in a highly polluted environment.

several different types of particles can be identified. As an example, particle 5 contains high quantities of iron and titanium and its origin is probably the brake system of a train. Particles 6 and 9 are both carbonaceous, but they have different morphology and size. Particle 6 is quite compact with a size of about 10 µm. Instead, particle 9 is a conglomerate of about 2 µm composed by ultra-fine particles whose sizes are around 100 nm. In the same picture, hundreds of smaller particles (about 10 nm) are attached to the filter fibers. Such a kind of particles are extremely harmful for human health and are mainly produced during the combustion of fossil fuels.

Particle 7 is, instead, a silica mineral grain with size of about 10 µm. It is interesting to observe, how two small organic particles (8) are attached on the surface of particle 7. Such organic particles, whose size is approximately 2 µm are probably spores or pollen.

Eventually, last two images show a quite long particle (10) that, when closely observed, reveals a very strange structure. The central carbonaceous body is covered by smaller flat particles (11) and a strange not-well identified formation (12).

It is possible to understand how atmospheric particulate matter includes a extremely wide range of different particles types, often conglomerated together and whose characteristics and origins are not always easy to evaluate. Such a diversity makes particulate

measurement and characterization extremely challenging and, often, this turns out in quite large uncertainties.

Subsequently, a first complete prototype of the proposed system was realized and tested by sampling the air and detecting captured particles by means of the optical system described above. The acquired filter pictures were processed by using the dedicated image processing software. As an example, figure 3.13 shows four images taken by the camera on the same area of a filter. First two pictures are the original ones, as taken by the camera respectively at 625 nm (red) and 375 nm (UV). The other two images show, instead, the results of the image processing software after channel extraction, normalization and sharpening. It is possible to see how the image taken in UV light results sharper than the one taken in red light due to the shorter wavelength. Moreover, it is interesting to note how some particle, marked in the figure with yellow arrows, exhibits a different transmissivity at the two different wavelengths. Such a difference is due to the different chemical composition and morphology of such particles. By taking advantage of this, it might be possible to employ the different backlighting wavelengths in order to perform a very simple spectral analysis of the particles, and, by means of a suitable classification, retrieve additional information on the particulate type and composition. Another example of such a effect is shown in figure 3.14. Here, it is clearly evident how some particle, marked with white circles, does not exhibit any difference in transmissivity and, instead, how other particles, marked with yellow circles, are almost transparent with red light.

Eventually, a measurement campaign was carried out in the city of Caserta, in South of Italy, where it was possible to access to a commercial laser-scattering system. Taking advantage from such an opportunity, the proposed monitoring system was installed beside the laser-scattering station and a 24 h measurement was carried out by both the instruments. Such a commercial station was equipped with a quite cheap particle counter based on the laser-scattering methods (ALPHASENSE, model: OPC-N2) which was able to provide measurements of the particulate concentration at intervals of 200 s for three different size ranges: PM10, PM2.5 and PM1.

The area, where the instruments were installed, was characterized by a quite low pollution level, with typical particulate concentration between 4 $\mu g/m^3$ to 6 $\mu g/m^3$. With the aim to avoid a filter saturation during the measurement and, at the same time, to achieve a suitable sensitivity, an air flux of 0.5 l/min was selected for the measurement. Figure 3.15-A shows a filter area of about 1.6 mm × 1.6 mm taken by the camera at 625 nm and, subsequently, processed by the software. Particles captured on the filter surface were identified by employing the blob detection algorithm and a map with the identified particles and the estimated equivalent size is shown in figure 3.15-B. The correspondent histogram of the particle size distribution is shown in figure 3.16. Most of the detected particles were in the range between 6 µm and 10 µm with a peak at about 8 µm. Few particles had size larger than 20 µm and no particle was detected down to 3 µm. In fact, mesh size for the selected filter is about 3 µm and the resolution achieved by the optical system is about 1 pixel/µm. Therefore, with such a configuration it is not

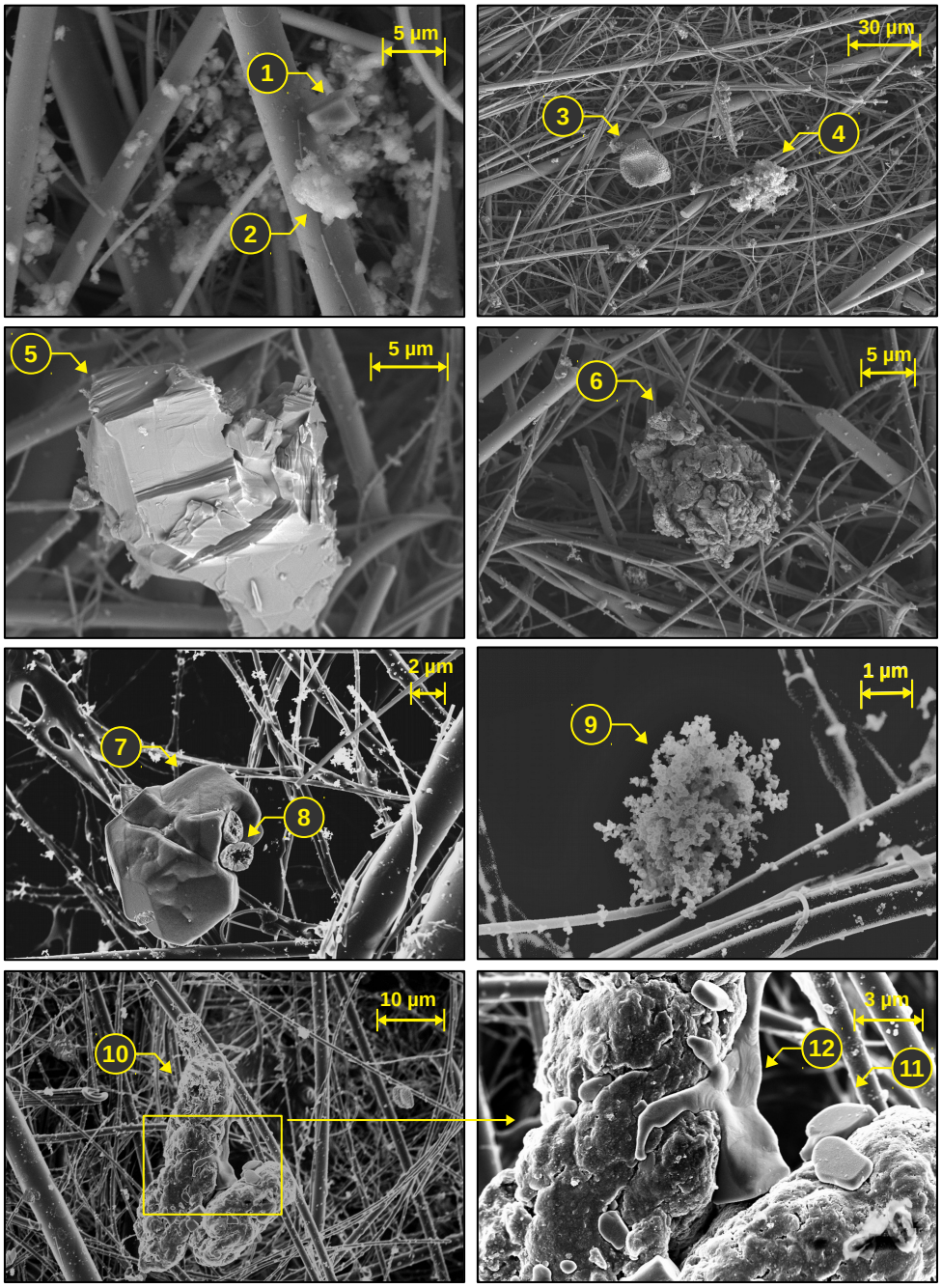

Figure 3.12: Example of several different particles captured on glass fibre filters.

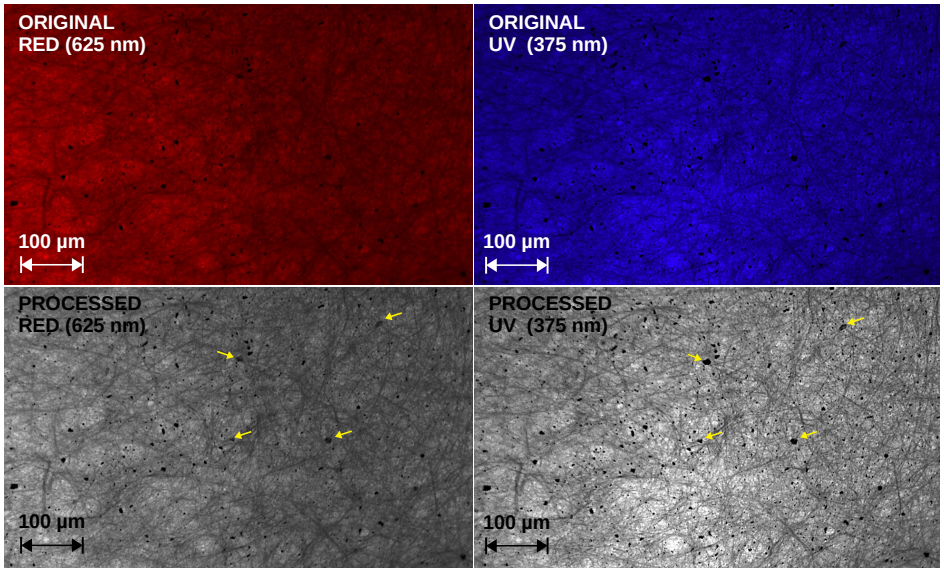

Figure 3.13: Pictures taken on a filter at 625 nm and 375 nm, before and after the image processing.

possible to detect particles smaller than about 3 µm.

The total amount of particulate was calculated by employing the formula 3.6 and considering that the total volume of sampled air was 0.72 m^3 and the filter sampling area was 2.56 mm^2. With the aim to compare the two instruments, a particle size range between 2.5 µm and 10 µm was selected. Particles whose size was out such a range were neglected and the total amount of sampled particulate during the 24 h of sampling was estimated in 0.0165 µg. Therefore, the particulate concentration estimated by the proposed system was about 0.36 $\mu g/m^3$.

The particulate concentration in the same range was calculated from the data provided by the laser-scattering station by simple difference between the PM10 and the PM2.5 concentrations. Table 3.3 reports a summary of the obtained results. Actually, the particulate concentration was around 5 $\mu g/m^3$, as expected. Unfortunately, most of the particles had a size below 1 µm (PM1) which cannot be detected by the proposed instrument. As it is visible analyzing the obtained results, the values provided by the two instruments are significantly different, even thought they are still comparable. It should be also considered that typical uncertainties of laser-scattering systems are in the order of a 20%, according to the particle type and the environmental conditions [124, 125]. Therefore, the achieved results are promising and more tests should be performed in order to better assess the performance of the proposed system.

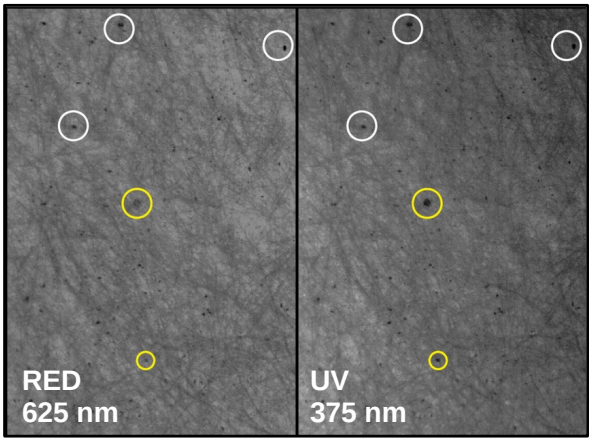

Figure 3.14: Pictures taken on a filter at 625 nm and 375 nm. Particles which do and do not exhibit difference in transmissivity are marked, respectively, with yellow and green arrows.

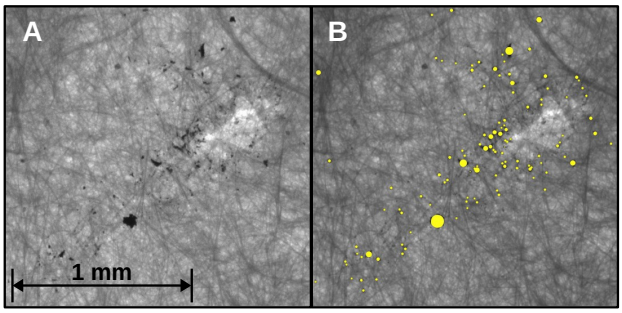

Figure 3.15: Picture of the filter exposed in the city of Caserta before (A) and after (B) the particle detection.

3.3 Conclusions and future work

Atmospheric particulate matter, as already discussed, is a serious issue because of its severe effects on climate and on human health. Its nature and properties largely change

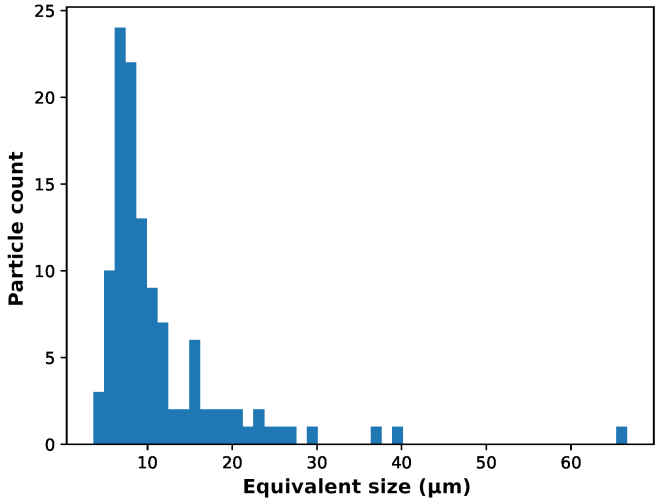

Figure 3.16: Histogram of the particle size distribution as detected by the proposed monitoring system during the measurement campaign carried out in Caserta.

Table 3.3: Summary of the results obtained during the measurement campaign carried out in Caserta. Original data measured by the laser-scattering station and of by the proposed system are compared together.

Laser-scattering Station				Prototype
PM10	PM2.5	PM1	$PM_{10-2.5}$	$PM_{10-2.5}$
4.98 $\mu g/m^3$	4.83 $\mu g/m^3$	4.25 $\mu g/m^3$	0.15 $\mu g/m^3$	0.36 $\mu g/m^3$

in space and time and strongly depends on its origin. Such a variability makes quite difficult achieve reliable measurements of its concentration and a fully characterization of its properties.

The measurement instruments commonly employed are mainly based on the gravimetric method and several different optical approaches such as the laser-scattering particle counters. Unfortunately, the quite high cost of such equipment together with the limited characterization such approaches are able to provide makes, still nowadays, extremely challenging the establishment of a capillary monitoring of particulate.

The novel optical approach discussed in this thesis tries to overcome such limitations with the aim to develop a portable monitoring system for the particulate characterized by an acceptable accuracy and a low cost. The preliminary tests performed on the realized prototypes revealed promising performance: the system is able to provide in real-time both the total amount of the particulate and its size distribution. Furthermore,

taking advantage by five wavelengths available in the backlighting system, it might be possible to implement a simple but effective spectral analysis of the captured particles which might provide additional information useful for a complete characterization of aerosol properties.

In such terms, the proposed system has several advantages in respect to the conventional approaches, such as the gravimetric one. In particular, it is able to provide real-time measurements, particle size distribution and several additional information on the aerosol type. Performed tests demonstrated the feasibility of such an approach providing results which are comparable to the laser-scattering devices, but at a lower cost. The wireless LoRa capability of the realized prototypes can be employed to arrange long-range sensor networks able to capillary monitoring in real-time the atmospheric particulate matter, application which hardly can be implemented with conventional equipment.

Additional tests and characterization have been planned in order to fully investigate the system performance and better assess its accuracy. In particular, a detailed classification of spectral response of several type of atmospheric particulate matters are required to assess the feasibility of the spectral analysis, and additional tests have to be carried out by comparing the system with commercial equipment in order to assess system accuracy and stability. Unfortunately, it has not still be possible to easily access to such instrumentation because of their high cost and the quite poor availability. Eventually, several improvements both of optical camera system and mechanical parts can be investigated in order to extend the detectable size range down to 1 μm. In this, the replacement of the camera with an auto-focus one featuring a higher resolution can be beneficial.

Therefore, even though several issues still require attention, the proposed approach opens the way to the development of new low-cost devices which might be employed in the atmospheric particulate monitoring in several possible scenarios and applications.

Chapter 4

Breath analysis

Breath analysis is a non-invasive diagnosis and monitoring method which, in the last decade, has become a feasible alternative to the traditional diagnostic approaches for several human diseases, especially those regarding lungs, metabolic disorders and gastroenteric diseases. This analytical technique is attracting great interest because of its several advantages such as non-invasiveness and safety.

Breth analysis, basically, consists in the detection of several gaseous species, called biomarkers, whose presence in the exhaled breath at a specific range of concentration is indicative of a distinct disease. Such biomarkers are present in the exhaled breath at very low concentrations and, therefore, high sensitive analytical instruments are mandatory in this field. Consequently, great research efforts have been carried out in last years in order to improve analytic techniques and, in this framework, the development of high-performance gas sensors is of crucial importance.

This and chapter 5 focus on this topic and describe the research work carried out with the aim of developing high-sensitive gas sensors for acetone, a recognized biomarker of diabetes.

In particular, this chapter deals with the breath analysis approach and provides a short summary about the state-of-art of the measuring instruments and techniques available for the detection of gaseous species in the human breath. Several different detection methods and equipment are described in section 4.2, and more details about gas sensors and about metal-oxide conductometric sensors are provided in section 4.3.

Chapter 5, instead, discusses about the research work carried out for the realization and the characterization of several prototypes of acetone sensors based on Nb_2O_5 thin films deposited by reactive plasma sputtering on small alumina substrates.

4.1 Breath analysis for human health diagnosis

In last years, breath analysis is becoming an effective a reliable diagnostic approach for assessing human health and detecting several diseases. The increasing reliability of such a method, together with a low management cost and its intrinsically safety, is making breath analysis a valid non-invasive alternative to the conventional diagnostic tests, such as blood and urine testes [37, 126]. In fact, breath analysis is able to provide information on the human health status which are similar to those obtained by conventional diagnostic approaches, but at a lower cost and with much less patient effort.

This technique was known since ancient times, where the smell of the exhaled breath was used as indication of the health condition. However, only in last decades, this approach has received attention by the scientific research, and great effort has been carried out with the aim to make this technique more reliable and to standardize the breath sampling procedure.

It is well known how exhaled breath contains hundreds of different molecules and compounds [127]. These gaseous species can have both endogenous and exogenous origin, being them in part produced internally the body and partially inhaled from the external environment. The composition of the human exhaled breath is very heterogeneous [128, 129], and it includes:

- several *inorganic gases*, such as carbon dioxide and monoxide, oxygen, nitrogen monoxide and hydrogen;
- hundreds of different *Volatile Organic Compounds* (VOC), such as acetone, ethanol, pentane and isoprene;
- several *non-volatile species*, such as isoprostanes and cytokines.

The endogenous species are the most important: they are produced inside the body, either directly in the respiratory system or they evaporate from the blood stream in the alveoli. Thus, many of these compounds can be considered as a sort of markers of the physiological processes occurring in the body. In particular, it has been found that some of these *biomarkers*, when present in the exhaled breath in a characteristic concentration range, are indicative of a specific disorder or disease [127–129]. By taking advantage of this correlation between the presence of specific biomarkers and the health status of the subject, breath analysis is able, by qualitatively and quantitatively detecting such markers in the exhaled breath, to provide quite reliable diagnosis on the presence and the status of specific diseases.

As an example, acetone is commonly considered a biomarker of diabetes. Several studies put in evidence the correlation of high acetone concentrations in the exhaled breath with the presence of diabetes in the tested subjects [65]. In fact, acetone is normally present in the human exhaled breath at concentration below 1 ppm. However, an a insufficient production of insulin by the pancreas, as in case of uncontrolled diabetes,

Table 4.1: List of the main biomarkers and the related diseases together the detection range.

Biomarker	Correlated disease	Detection level
acetone	diabetes	ppm
ammonia	renal failure; ulcers related to bacterial infections; protein metabolism	ppb ∼ ppm
carbon disulphide	schizophrenia; coronary disease	
carbonyl sulphide	liver diseases	ppb
hydrocarbons	cancer; heart transplant failure; bacterial infections	ppb
nitric oxide	asthma; inflammation of respiratory system	ppb
hydrogen cyanide	cystic fibrosis	ppb
hydrogen	bacterial infections; H. Pilori infections; carbohydrates metabolism	ppb ∼ ppm
ethane, penthane	oxidative stress	ppv
formaldehyde	breast cancer	ppb
acetaldhyde	lung cancer	ppb

turns out in a significant metabolic disorder with involves the increasing of blood glucose together with an abnormal lipolysis [130]. This metabolic disorder is responsible of a significant increasing of acetone concentration in the exhaled breath. According to such studies, a threshold of about 1.5 ppm ∼ 2 ppm is typically employed to discriminate between healthy subjects and diabetic ones [66].

Another possible application of breath analysis is the detection of oxidative stress. This disorder consists in an accelerated oxidation of cells and it can be due to several factors, among them there is food, smoking, and also many diseases (such as diabetes) have as consequence an increasing of the oxidative stress [131]. Many studies put in correlation the high concentration of alkanes (ethane and pentane) in the exhaled breath with a abnormal oxidative stress [132].

Many other markers have been identified and correlated with specific diseases: gastroenteric disorders (H_2), bacterial infections (H_2, ammonia, several hydrocarbons), cancer (hydrocarbons, alkanes, formaldehyde, acetaldehyde), asthma (NO, isoprostanes), just to cite few of them. Table 4.1 reports a list of some among the principal biomarkers and the correlated diseases, together with the typical detection ranges [37, 133].

Breath analysis has several advantages in respect of the conventional diagnostic approaches. Surely, this technique is intrinsically *non-invasive* and *safe*. In fact, no access

to any part of body and no intake of any substance is required to perform a breath analysis test; just the patient has to normally blow the exhaled breath inside an inlet for the subsequent gas sampling. This turns out in reduced effort and stress of the patient during the test, factor which is very important for elder people or subjects affected by highly debilitating diseases, especially when such tests should be performed daily or several times by day (e.g. diabetes). Moreover, the analytical procedures required for the breath analysis are usually simpler than what is required for other methods, like blood and urine analysis, and available at a lower price. Another important advantage is that, typically, results are available in real-time when, as opposite, conventional methods requires usually hours or days. The breath analysis approach can be employed in very different situations: for example, it can be performed both on conscious subjects and on mechanically ventilated ones [134].

Although, many advantages are evident, some drawback is, nowadays, limiting the employment of this diagnostic method. In particular, there is not a standard method for sampling the exhaled breath [37], and this lack turns out in quite dispersed results with often unacceptable uncertainties of the detected biomarker concentrations. Also, there is a technological limitation regarding the sensing performance of the analytical instruments and sensors. Many of such biomarkers are present in the exhaled breath only in traces, with concentrations ranging from few ppt to several ppm. Gas sensing at concentrations down the ppm level are, still nowadays, challenging and only high-sensitive equipment can be employed successfully. Otherwise, a pre-concentration of the exhaled breath is required by means of gas bags or semi-permeable materials [133], but with the increasing of the cost and the possibility of contamination. Furthermore, it should be considered that the human breath is a very complex mixture of gaseous species, many of them chemically similar, and present at very different levels of concentrations. This makes the detection of specific compounds extremely difficult with the possibility of false diagnosis due to possible interferent species. This turns out in the necessity of extremely selective analytical methods, equipment and sensors with the consequence of increasing the test cost.

Several analytical techniques are nowadays available for the detection of specific gaseous species in complex mixtures, such as the human breath. Next section provides a short description of the equipment typically employed in the breath analysis.

4.2 Gas detection methods for breath analysis

Gas detection devices have to satisfy specified constraints due to the characteristics of the exhaled breath and the typical concentration of the biomarkers. In particular, an high-sensitivity is always required in order to detect biomarkers at a ppb or ppm concentration levels. Moreover, being the breath a complex mixture of hundreds gaseous species, an excellent selectivity is mandatory.

The most employed detection methods are: gas chromatography, laser-absorption

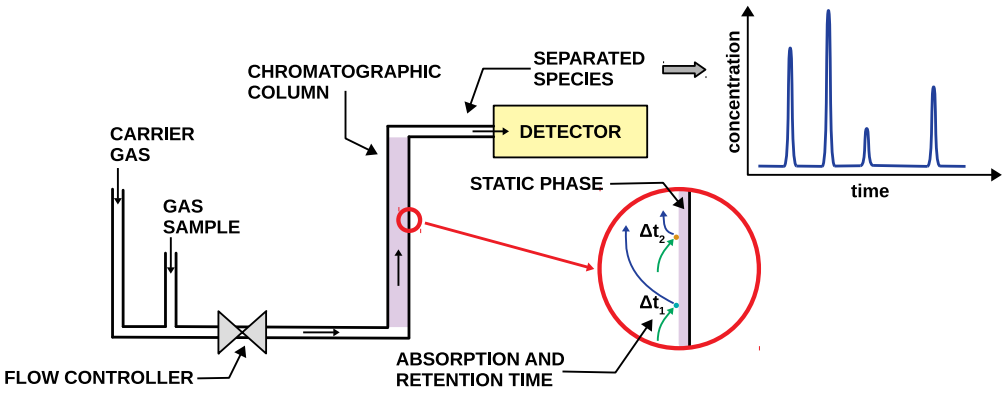

Figure 4.1: Basic scheme of a gas chromatographic system.

spectroscopy and chemical gas sensors. A brief description about these techniques is provided in this section, with the exception of chemical gas sensors which are described in more detail in section 4.3.

Gas chromatography (GC) is employed in any field where high selectivity and sensitivity are required. This technique is based on the different affinity of the gaseous species towards a stationary phase. A schematic block diagram of a CG device is shown in figure 4.1. Basically, the gas mixture sample is injected inside a *chromatographic column* and propelled by an inert carrier gas, such as helium. This column can be considered as a rigid capillary tube, whose walls are covered by a specific liquid or polymer which forms the stationary phase. The several gaseous species, while moving inside the column interact with the column walls and are adsorbed on the stationary phase. Subsequently, they are released at different times according to their affinity with the stationary phase itself. This way, the input mixture is actually separated in its constituents which are expelled from the column at different time periods. At the output of the column, a proper detector can quantify the amount of each gas. According to the specific application, several types of detectors can be employed. In the field of breath analysis, the most used are surely the Flame-Ionization Detector (FID), the Mass Spectrometer (MS) and the Ion-Mobility Spectrometer (IMS).

Flame-Ionization Detectors are mainly employed for organic compounds. The compounds are burnt in a hydrogen flame. During such a combustion, ions of the original gaseous species are generated in a concentration that is proportional to the concentration of species themselves. Two electrodes are placed close to the burning site in such a way that an electrical current, proportional to the ion concentration, flows between them. Thus, by measuring such a current it is possible to accurately measure the concentration of the sampled species. This type of detector is characterized by a high

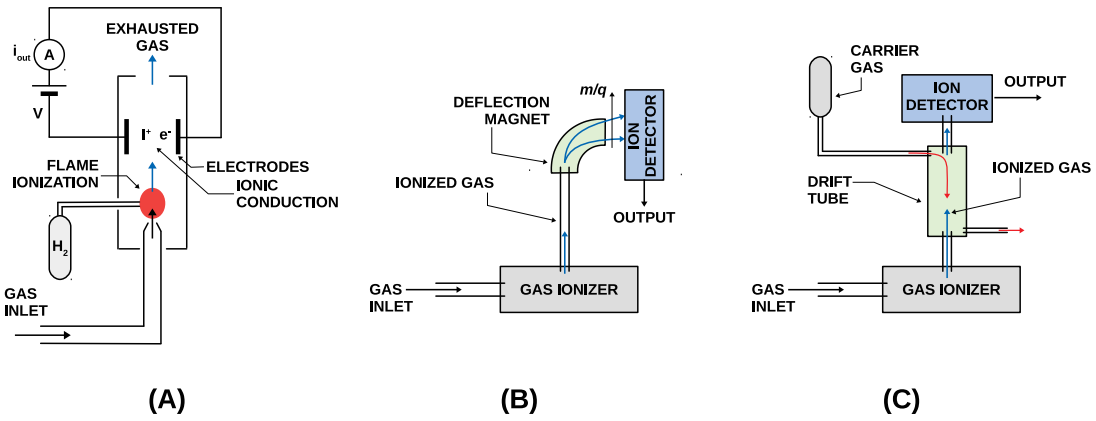

Figure 4.2: Simplified block diagrams of the most diffused detectors for gas chromatography: flame-ionization detectors (A), mass spectrometers (B) and ion-mobility spectrometers (C).

sensitivity, very good linearity and a low cost. However, its use is restricted only to species which can be ionized by combustion (mainly organic compounds). A schematic diagram of a FID is shown in figure 4.2-A.

Mass Spectrometers, instead, not only quantify the amount of specific compounds but also are able to perform a separation of the species. Thus, virtually mass spectroscopy can be employed alone to separate and detect species in a mixture. Anyway, it is usually employed together with gas chromatography for improving selectivity.

A basic MS is shown in figure 4.2-B. This method is always based on the ionization of the species, but this ionization is performed not with a flame but, for example, by means of an electron bombardment. This enables virtually any specie to be detected. Once the species have been ionized, they are accelerated and forced to move inside a strong electric or magnetic field. In such a way, the ions are deflected proportionally to their mass-to-charge ratio. The ions are finally collected and detected by dedicated detectors, such as electron multipliers and Faraday cups. The output of a MS is a spectrum showing the amount of detected ions as function of the mass-to-charge ratio. Being this ratio a sort of *fingerprint* of the species, by analyzing such a spectrum, it is possible to know which species are present in the mixture and their concentration.

Also the Ion-Mobility Spectrometers are able to separate the species and evaluate their amount, but with an approach quite different from the MS, but still based on the ionization of the species. The schematic diagram of an IMS is shown in figure 4.2-C. The ionization can be induced, for example, by electron bombardment or corona discharge. The ionized species are forced to flow inside a *drift tube*. The ions are accelerated inside the drift tube by a suitable electric field. At the same time, an inert carrier gas, such as

helium, is forced to flow inside the drift tube in a direction opposite to the ion movement. The mobility of the ions inside the carrier gas is a characteristic of the specific species and, as consequence, different ions exhibits different travel times inside the drift tube. Thus, ions characterized by an high mobility exit from the drift tube before ions featuring lower mobility. In such a way, the different species are separated and can be detected at the end of the drift tube by using proper detectors which generate an electric signal. A proper analysis of such a signal provides information about the species present in the mixture and their concentration.

A completely different approach is the one adopted by laser-absorption spectroscopy (LAS). This technique is extremely sensitive and selective, with detection limits in the order of few ppt. The basic idea is that each gaseous specie is characterized by a specific light absorption coefficient which exhibits absorption lines at specific wavelengths. Thus, it is possible to evaluate the concentration of specific gaseous species by using lasers at specified wavelengths and measuring the total light absorption thought a known volume of gas. Unfortunately, this technique requires extremely sophisticated and expensive equipment, and this actually limits its employment only to the research field.

Other gas separation and detection methods are employed in breath analysis, as well. However, even though all these approaches achieve excellent sensitivity and selectivity, they usually employ costly and bulky equipment which partially depreciate the advantages of breath analysis in respect to the conventional diagnostic methods. For these reasons, great efforts have been carried out in last years in order to develop alternative detection approaches which result in lower cost and smaller size and, at the same time, which maintain sensitivity and selectivity at an acceptable level. In this, chemical gas sensors are a very promising alternative.

4.3 Chemical gas sensors

Chemical gas sensors are, nowadays, a valid alternative to the most expensive and complex techniques described in the previous section. Actually, there are several types of gas sensors which differ for the sensing mechanism and, of course, for target gas and sensing performance. Most employed gas sensors in the breath analysis field surely are: conductometric sensors (or chemoresistors), electrochemical sensors and colorimetric sensors. Each one of them has its advantages and drawbacks according to the specific application.

Electrochemical gas sensors are quite simple devices featuring two or three electrodes and a semi-permeable hydrophobic membrane, as shown in figure 4.3-A. The electrodes are placed in contact with an electrolytic material. These electrodes are usually manufactured with precious metals and they can be functionalised by covering them with catalytic films. The gas molecules diffuse through the semi-permeabile membrane, and then through the electrolytic solution till they arrive close to the Working

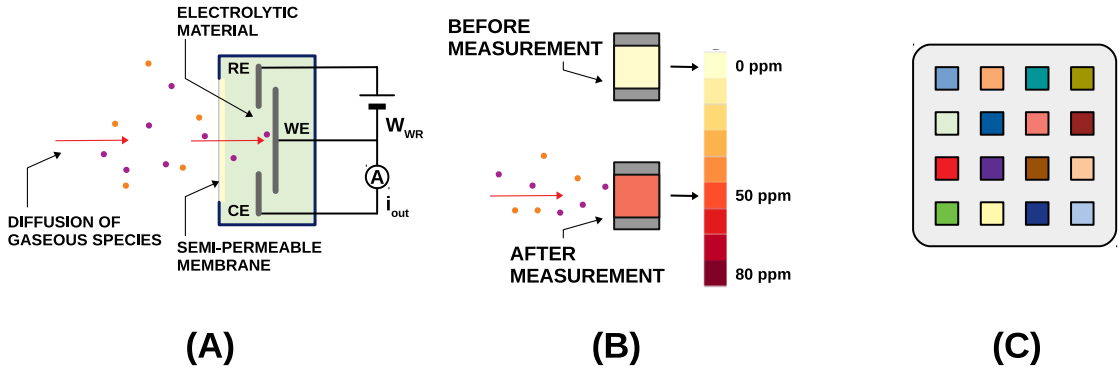

Figure 4.3: Some type of gas sensors. A) structure of an electrochemical gas sensor; B) usage of colorimetric gas sensors; C) a colorimetric sensor array.

Electrode (WE). Here, some oxidation or reduction reactions occur between the gas molecules and the WE as function of the gas, WE material and the difference of potential V_{WR} between the WE itself and the Reference Electrode (RE). As consequence of these reactions, couples of electron-ion are generated and flow through the electrolytic solution generating a current between the WE and the Counter Electrode (CE). Such a current is almost proportional to the original gas concentration. In order to establish such a reactions, a proper value of V_{WR} is required in order to reach the activation energy of the specified reaction. Taking advantage of this peculiarity, it is possible to improve the sensor selectivity by properly biasing the WE. Small size and very low power consumption, together with a good sensitivity, are the main advantages of such sensors. However, it is not always easy to tune these sensors towards any possible biomarker, and this limits their use in the breath analysis.

The branch of the colorimetric gas sensors includes a very wide range of devices which employ quite different sensing mechanisms. Anyhow, all of them share the common basic sensing idea: to correlate the gas specie and its concentration to a change in color of the sensing material, as shown in figure 4.3-B. Basically, the gaseous species reach the sensing material, where they are absorbed or react chemically with it and, as consequence of such an interaction, the sensing material changes its color in a specified way. The ph strip is a classical example of such type of sensors, where the color of the sensing material changes according to the acidity of the analyte. Colorimetric sensors are usually characterized by a very low cost and quite good sensitivity and selectivity. They can be easily combined to form a sensor array in order to detect more target gases in a single sampling. Figure 4.3-C shows an example of such an application: by analyzing the cross-correlation of the sensor responses it is possible to significantly increase the selectivity of the array towards specific gases. Moreover, the color response array

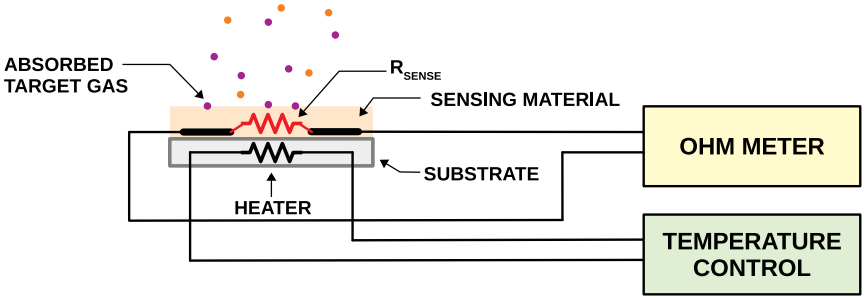

Figure 4.4: Schematic structure of a conductometric gas sensor connected to a read-out measurement setup.

can be considered as a sort of *fingerprint* of the exhaled breath.

Unfortunately, most of these sensors are single-use only: they are required to be replaced after each sampling. Another possible drawback is a relatively poor accuracy in term of concentration. In some case, they can be only used to qualitatively assess the presence of a specified gas and not for accurately quantify its concentration.

4.3.1 Conductometric Metal-Oxide Gas Sensors

Nowadays, conductometric gas sensors are one of the more extensively studied sensor type because of their very good characteristics, flexibility and low cost. They are employed in several fields, from environmental monitoring to industrial, automotive and medical applications. The basic structure of such a sensor, shown in figure 4.4, includes a substrate with two electrodes electrically connected with a sensing material. The conductivity of the sensing material changes when a specified gas is absorbed on the sensing surface. This way, it is possible to evaluate the target gas concentration by measuring the resistance between the two electrodes (R_{SENSE}). Often, the optimal sensing performance are achieved at high temperatures. In such cases, a heater is included in the substrate so that the sensor working temperature can be adjusted by means of a suitable temperature control system. It is clear how all the sensing performance of such sensors are related to the sensing material, and this explains why most of the research in this field focuses on the development of innovative materials which are tuned specifically for enhancing the sensing performance towards specific gases.

The most important type of conductometric gas sensors are the metal-oxide (MOX) sensors, even though good performance can be achieved also with polymers and other innovative materials, such as carbon nanotubes and graphene. In MOX sensors the sensing material is basically a metal oxide which, under specific circumstances, can exhibit a semiconductive behavior due to the surface vacancies.

Several characteristics are used to evaluate the performance of a MOX sensor, among these the most important for breath analysis surely are: sensitivity, selectivity, stability, response and recovery times and, of course, cost.

Sensitivity is defined as the smallest variation of the target gas concentration that can be detected by the sensor. Therefore, such a parameter measures the capability of the sensor to detect the target gas. In general, it is desirable to have sensitivity as higher as possible, especially in the breath analysis where the biomarkers have concentrations at the ppb or ppm levels. However, in specific cases an high sensitivity can be a problem. In fact, another important parameter of a gas sensor is the saturation level, defined as the maximum concentration which can be measured by the sensor. Therefore, sensitivity of a sensor should be selected accordingly to the expected target gas concentration. In a MOX sensor the sensitivity is given in terms of relative resistance variation of the sensor, defined as:

$$S = \frac{R_a}{R_g} \tag{4.1}$$

for reducing gases, and defined as:

$$S = \frac{R_a}{R_g} \tag{4.2}$$

for oxidizing gases, where R_a is the resistance of the sensor in the reference gas (typically air without the target gas) and R_g is the resistance at a specified target gas concentration.

Selectivity is another key parameter. Selectivity is defined as the capability of a gas sensor to discriminate between several gas compounds. An ideal sensor should have a high sensitivity towards the target gas and a negligible sensitivity towards all the other gas which can be present during the measurement. This is especially important in breath analysis, where the exhaled breath is a very complex mixture of gases and volatile compounds in a quite wide concentration range.

Stability is, instead, defined as the sensor capability to maintain its performance in time. In MOX sensors, stability degrades with time and repeated heating-cooling cycles. As consequence, there is an uncontrolled variation of its characteristics such as sensitivity, response time and selectivity. Stability is an important parameter because it directly affects the accuracy of the sensor and, therefore, of the concentration measurements.

Response and recovery times measure the capability of the sensor to quickly respond to variations of the target gas concentration. The response time is defined as the time required for the sensor to rise from the 10% to the 90% of the final response value in correspondence of a abrupt variation of the target gas concentration from 0 ppm to a certain value. Recovery time is defined in the same way, but in correspondence of the opposite variation of the target gas.

Finally, cost includes the costs for the raw materials and the manufacturing equipment. Of course, the characteristics of an ideal MOX sensor depend on the specific

application but, in general, it is desirable to have high sensitivity, high saturation level, excellent selectivity, fast response and low cost.

In order to select or develop a suitable MOX sensor for a specified application, it is very important to clarify the sensing mechanisms of such sensors. Two different sensing mechanisms can be identified for MOX sensors: *surface conductivity sensing* and *bulk conductivity sensing*.

Bulk conductivity sensing mechanism occurs only at a very high temperature, usually higher than 700 °C. In such a situation, all the surface bonds are broken by thermal energy and the conductivity of the sensing film is dominated by the oxygen partial pressure. In fact, at these temperatures it is required a thermodynamic equilibrium between the oxygen inside the sensing material and the oxygen present in the external environment. The presence of a target gas turns out in a variation of the oxygen partial pressure in the environment and, therefore, the amount of oxygen inside the sensing material has to change accordingly, with a consequent variation of the sensor conductivity.

However, temperatures involved in normal applications are well below 700 °C. In such a temperature range, the sensing mechanism for MOX sensors is dominated by surface effects.

Figure 4.5-A shows the schematic structure of a MOX sensing material at different levels of magnification. Normally, metal oxides are crystalline and they exhibit a grain-like microstructure composed by small grains attached one to the others. Several broken bonds and vacancies are available on the grain surface. These vacancies act as ionosorption sites for the gas molecules present in the environment. Oxygen presents in the air is easily ionosorbed in such sites and, as consequence, several electrons are subtracted from the conduction band and trapped in the ionic bonds. This process turns out in the formation of a charge depletion layer around the grain surface and the establishment of a potential barrier at the grain boundaries which actually limits the drift of the charge carriers and, therfore, the conductivity of the sensor. This way, the metal oxide behaves as a N-type semiconductor. In a similar way, some other metal oxides exhibit a P-type behavior in which holes are trapped in the ionic bonds instead of electrons. Figure 4.5-B shows such a situation for both N-type and P-type metal oxide semiconductors, highlighting the potential barriers at the grain boundaries.

The presence of a target gas modifies such an equilibrium between the environmental oxygen and the sensing material. In fact, the target gas molecules interact with the ionosorbed oxygen and/or directly with the sensing material by means of competitive ionosorption processes. This turns out in a modification of the number of electrons trapped in the ionic bonds and, as consequence, the electronic band structure bends accordingly. Such situation is shown in figure 4.5-C. In the case of N-type metal oxides, oxidizing and reducing target gases, respectively, increase and decrease the potential barrier at the grain boundaries modulating the conductivity of the sensor in function of the target gas concentration. The opposite occurs in the case of P-type metal oxides.

Therefore, it is possible to identify two separate contributes to the sensing mechanism: a *receptor function* and a *transducer function*. The first contribute is due to the

interaction, at a microscopic level, between the gases and the sensing surface by means of the ionosorption processes. The second one, instead, transforms the modification involved by the receptor function into a macroscopic variation of the sensor conductivity by means of the potential barrier across the grain boundaries.

Several factors affect the sensing performance of MOX sensors. Among these, there are the morphology and the structure of the sensing surface. Grain size is extremely important because it significantly affects the sensors sensitivity. There are three possible cases, shown in figure 4.6.

- Grain boundary control: $D \gg 2L$ – When the grain size D is much greater than the thickness of the depletion layers L, the conductivity of the material is dominated by the Schottky barriers present at the grain boundaries, whose amplitude is modulated by the target gas concentration.
- Neck control: $D \approx 2L$ – When the grain size is similar to the depletion layer thickness, the conductance of the sensing material is controlled by the necks due to the depletion layer. These necks, present between each grain, change in aperture according to the target gas concentration.
- Grain control: $D < 2L$ – When the grain size is smaller than the depletion layer thickness, the conductivity of the material is controlled by each single grain, not only their boundaries or necks.

In general, the sensor response increases with the increasing of the number of controlling elements. Therefore, grain control is the situation which provides the best sensitivity for a specified material. Thus, it is convenient to develop materials with small grain sizes, even though it should be considered that extremely small grain sizes turn out in a low structural stability. Furthermore, also the sensing film thickness affects the sensitivity. Typically, thin films exhibits a response higher than thick ones because of the interaction between material and target gas occurs only at the surface. Instead, the bulk material contribute is constant and it reduce the sensitivity. For the same reason, very porous films, typically, turn out in a sensitivity higher than compact ones. Such an effect is known as *utility factor* and it occurs because porous films have large surface-to-volume ratios and, as consequence, in such materials the surface effects strongly dominate the bulk conductivity. Unfortunately, porosity involves a drawback: an increasing of the response and recovery times. This because more time is required for the target gas to diffuse inside the pores and reach the sensing surface.

Several methods are nowadays employed in order to improve the performance of the MOX sensors. A very effective method is the addition of impurities to the metal oxide. These impurities can act in two different ways: either as dopants or as catalytic agents. In the first case, the added impurities are able to change the conductivity of the material and, as an example, they can be used to decrease the reference resistance R_a in order to improve the signal-to-noise ratio during the measurements. Instead, in the

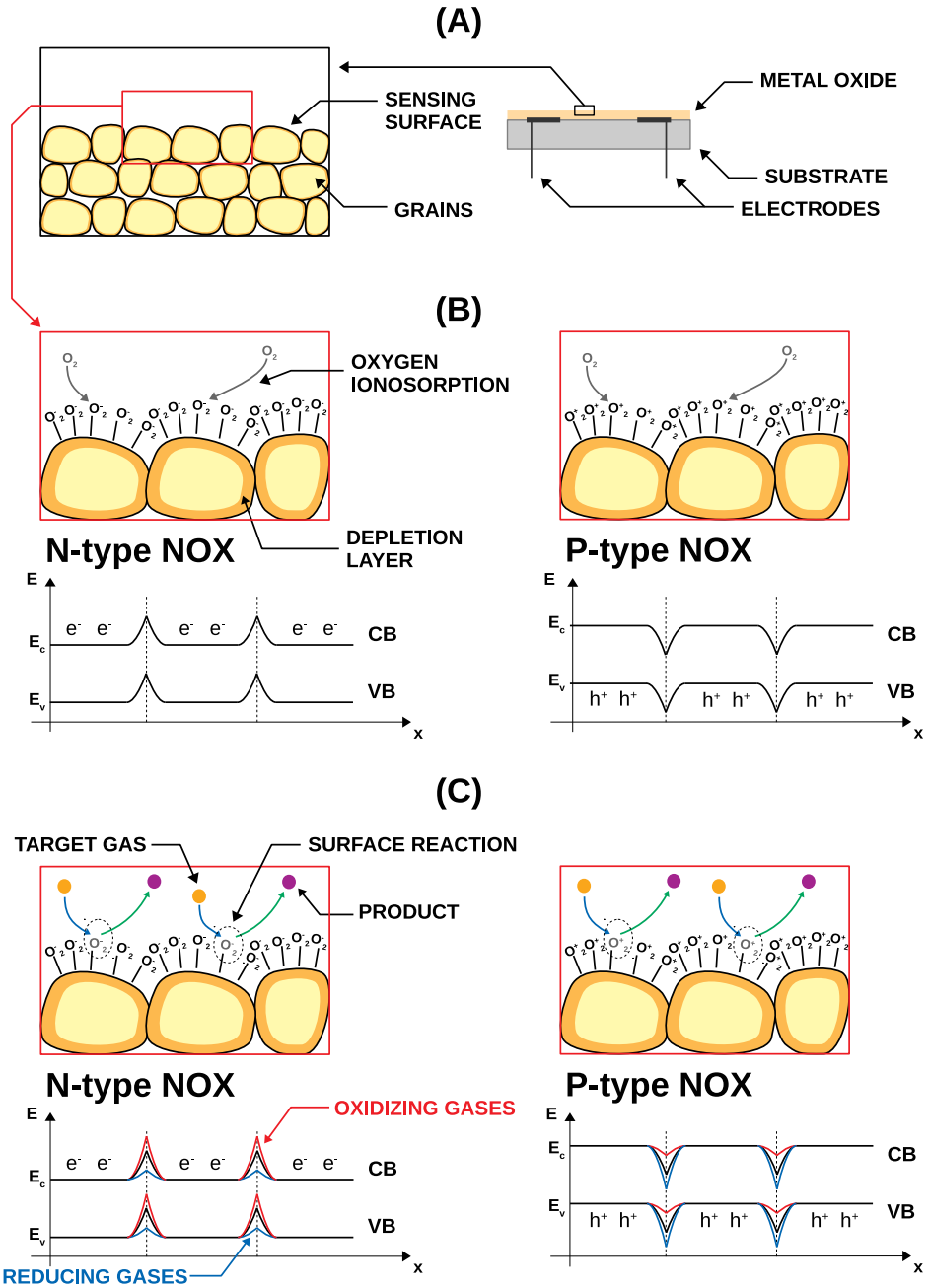

Figure 4.5: Schematic description of the surface sensing mechanism for MOX sensors. A) microstructure of a metal oxide used as sensing material in a MOX sensor. B) Ionosorption of environmental oxygen for both N and P-type metal oxides. C) Interaction with the target gas and modulation of sensor conductivity.

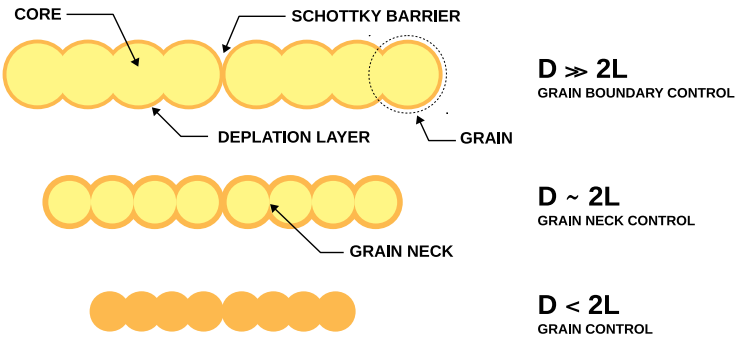

Figure 4.6: Effect of the grain size on the conductivity of the sensing material.

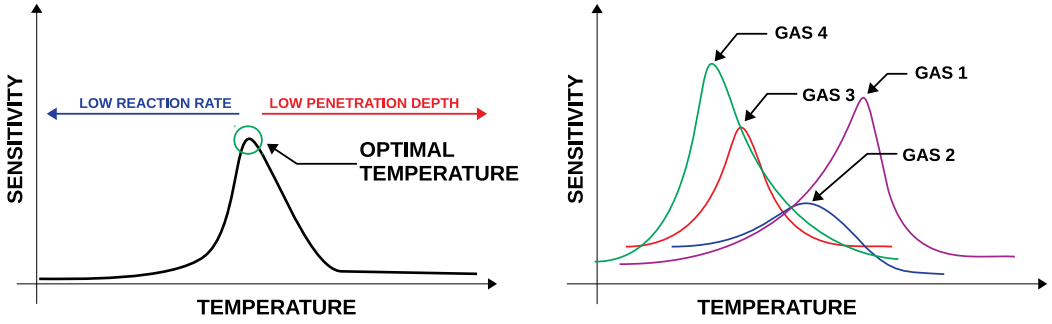

Figure 4.7: Left: typical sensitivity as function of temperature for a MOX sensor. Right: an example of sensitivity of a MOX sensor towards four different gases as function of temperature.

second case, noble metals are employed as catalytic material with the aim of improving the surface reactivity towards specific gases. As a consequence, there in an increasing of the sensor sensitivity and an enhancement of its selectivity.

Another extremely important parameter to take in consideration is the working temperature. Almost all the sensing characteristics of a MOX sensor depend by temperature. Firstly, the resistivity of a metal oxide decreases when the temperature increases. Therefore, increasing the working temperature can make easier to measure the resistance of the sensor which, otherwise, can be in the order of several TΩ. Furthermore, both chemisorption and diffusion processes, which stand at the base of the MOX sensing mechanism, depend strongly by temperature. In particular, it is well known how

reactivity of materials increases with the temperature. However, temperature also affects the ionosorption bonds which oxygen and target gas form on the sensing surface. As the working temperature increases these bonds start to broken due to the increasing thermal energy. As a consequence of this, the sensitivity of MOX sensors strongly change with the working temperature with the characteristic bell-shaped dependence shown in figure 4.7 (left): initially, the sensitivity increases with temperature because of the reactivity effect but, subsequently, it starts to decrease because bonds begin to break and the penetration depth of the gases reduces. Therefore, the best sensitivity is reached when the two effects balance one the other. Such an optimal working temperature depends from the sensing material and the target gas, so that different target gases exhibit different optimal working temperatures, as shown in figure 4.7 (right). Such an effect can be employed to improve the selectivity of the MOX sensors by modulating the working temperature.

Clearly, it is extremely difficult to optimize all the parameters involved in the operation of a MOX sensor and, usually, the development of an effective sensor requires long time and the realization of several prototypes.

Chapter 5

High-sensitive metal-oxide acetone sensors for breath analysis

This chapter partially contains materials from previously published work of the author [5]

The aim of this research work was to investigate a possible implementation of gas sensors for monitoring the acetone in the human breath. Among the several possibilities, it was decided to focus the research on conductometric gas sensors based on metal-oxide films because of the promising tradeoff among their sensing performance, power consumption and cost, and the availability of a reactive magnetron sputtering system for the deposition of the sensing film. Such a kind of sensors basically requires:

- a sensing material characterized by high sensitivity and selectivity towards acetone;
- a substrate with suitable contacts in order to electrically connect the sensing material;
- a heater in order to set the sensor working temperature.

After a preliminary investigation on suitable sensing materials, the niobium oxide was selected as candidate for the development of high sensible and selective acetone sensors. In fact, even though few works deals with this oxide employed as gas sensing material, its transport and sensing performance are quite interesting [53, 61, 62].

A commercially-available alumina substrate was selected as support for the deposition of Nb_2O_5 thin films. Such a substrate features platinum screen-printed iterdigitated electrodes on the top face, and a small platinum heater on the back side.

Subsequently, several sensor prototypes were realized by depositing thin films of Nb_2O_5 on such an alumina substrate by means of the *reactive magnetron sputtering* technique in a *capacitively-coupled parallel-plate reactor*.

This chapter describes development and characterization of such sensors providing details about their realization and the tests performed for evaluating their performance. In particular, section 5.1 provides a short introduction about the reactive magnetron sputtering technique. Section 5.2 describes in details the structure of such sensors, and the equipment and procedures employed in their realization. Eventually, sections 5.3 and 5.4 deals with the characterization of the proposed sensors, the achieved results and the possible future improvements.

5.1 Reactive magnetron sputtering

Reactive Magnetron Sputtering (RMS) is a deposition technique which developed rapidly in last decades and, nowadays, it has become a well-established process for deposition of high-performing films and coatings which can often outperform films deposited with different approaches both in the research and industrial fields [135,136].

The sputtering deposition process was firstly introduced in the 70s and progressively improved with several variants starting from the 80s. A significant performance enhancement of this process arrived with the introduction of the reactive magnetron sputtering and its different variants (balanced and unbalanced RMS, DC- and RF-driven RMS, pulsed magnetron sputtering, multi-source sputtering, variable-field magnetron).

A magnetron sputtering system is basically composed by two electrodes, a cathode and an anode connected to a proper power supply and placed in a deposition chamber. A vacuum system provides to decreases the chamber pressure to few Pa and a system of mass flow controllers is responsible to generate inside the chamber a controlled gas mixture. The cathode, or *target*, is composed by the material to deposit or by a precursor of it. The substrate to be deposited is, instead, placed on the anode. Figure 5.1 shows the basic structure of a reactive magnetron sputtering system.

The power supply drives the two electrodes with a proper voltage (which can be DC or AC) in order to generate and maintain a glow plasma discharge between the electrodes, in close proximity of the target. Thus, the target is subjected to a high-energy ion bombardment which sputters (erodes) atoms of the target that, after a transportation process, condense on the substrate surface depositing the film. Low-pressure inert gases, such as Argon, Kripton and Neon, are required inside the deposition chamber in order to create the glow plasma discharge. Typical pressure is in the order of 10^{-3} mbar. In this case, the target material deposits on the substrate without being involved in any chemical reaction. However, there is the possibility to add other gasses or precursors so that the target material can reacts with these gases creating a different material for the deposition (reactive magnetron sputtering). By using this approach, it is possible, for example, to deposit metal oxides and nitrides starting from pure metal targets. A secondary consequence of the ion bombardment of the target is the emission of secondary electrons. These secondary electrons, if properly confined, can contribute to the plasma maintenance and, as benefit, it is possible to reduce the voltage across the electrodes.

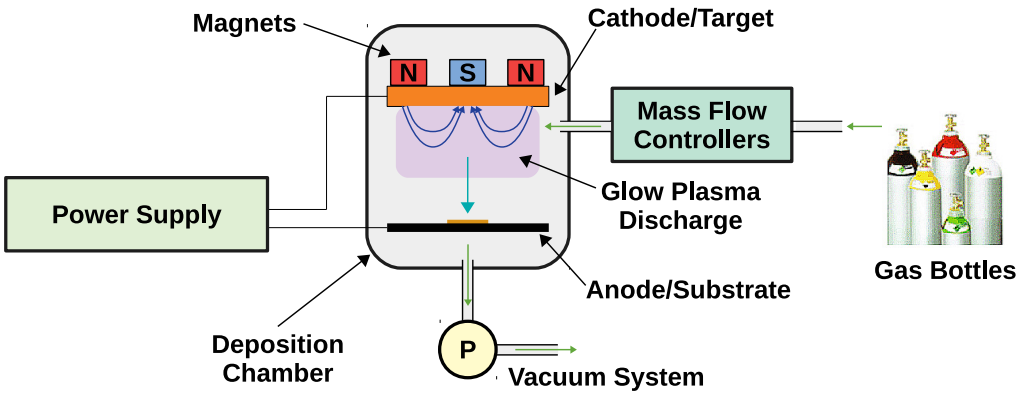

Figure 5.1: Basic scheme of a reactive magnetron sputtering system.

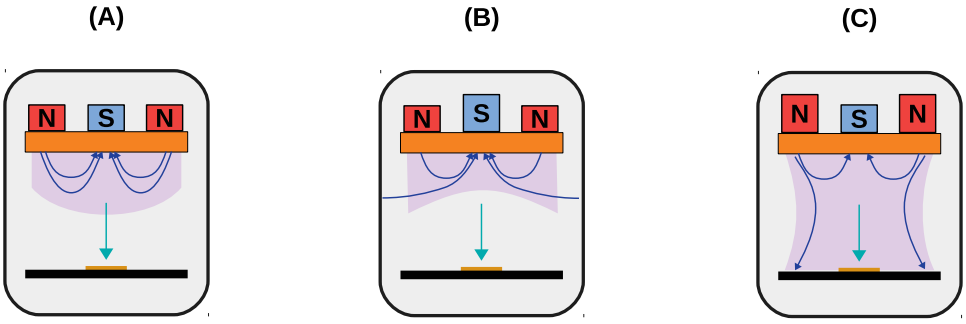

Figure 5.2: Basic magnetron configurations: balanced (A), unbalanced type 1 (B) and unbalanced type 2 (C).

Moreover, a proper confinement of the electrons increases the plasma density on the target turning out in a higher sputtering and deposition rates. At this purpose, several strong magnets are placed in the back-side of the target in such a way that one pole is in the target center, and the other one forms a ring around on the edge of the target itself. As a consequence, a strong magnetic field develops in proximity of the target forcing the secondary electrons to be confined according the field flux lines. By properly adjusting the magnet position and the strength, it is possible to modify the magnetic field and, with it, the distribution and the shape of the plasma discharge. Three basic cases can be identified.

- Balanced Magnetron Sputtering – The strength of the two magnetic poles is almost equal; all the flux lines of the magnetic fields close on the target itself and,

as consequence, the glow plasma discharge is confined within few centimeters from the target with a small plasma density on the substrate.

- Unbalanced Magnetron Sputtering, Type 1 – The central magnetic pole is stronger than the one on the target edge so that some of the flux lines of the magnetic field close on the chamber walls. This involves a modification in the plasma distribution which results in very low plasma density on the substrate.

- Unbalanced Magnetron Sputtering, Type 2 – The external ring magnetic pole is stronger than the central one; some flux line closes on the anode and the plasma distribution expands towards the substrate. As consequence the plasma density on the substrate increases significantly.

Figure 5.2 shows the three configurations and the resulting plasma distribution: balanced (A), unbalanced type 1 (B) and unbalanced type 2 (C). The magnetic field and the resulting plasma distribution strongly affect the characteristics and the morphology of the deposited film. It has been observed how increasing the ion current on the substrate turns out in more compact and defect-free deposited films which feature reduced strain stress [137–140]. Among the three described configurations, the unbalanced one (type 2) is the one providing higher ion currents on the substrate and the one typically employed today in most of applications. In contrast, it has been noted how the unbalanced type 1 configuration involves a very low ion current on the substrate and this turns out in very porous films [141]. This can be a desirable property in specific applications, such as the deposition of sensing films, catalysts and low-reflective coatings. A particular type of magnetron sputtering system is the *Variable Field Magnetron* which embeds a motion system for the magnets so that it is possible to optimize the magnetic field configuration according to the application.

Magnetron sputtering systems can differ also for the electrode biasing. As said previously, it is required a proper biasing of the two electrodes in order to generate and maintain the plasma glow discharge. The simplest case is the DC magnetron sputtering where the power supply biases the system with a DC voltage of few hundreds volts. This method has the advantage of using a relatively cheap power supply and a direct coupling between it and the electrodes. Unfortunately, a DC biasing requires conductive targets to allow a continuous current to flow between the electrodes, and this limits the target to be a metal or, in general, a conductive material. The alternative is the RF magnetron sputtering which employs a RF power supply (typical frequency is 15.36 MHz) capacitively coupled to the electrodes in order to virtually enable any material, including insulators and ceramic materials, to be employed as target. However, this turns out in a more expensive equipment and the requirement of a RF impedance matching network connected between the power supply and the electrodes that has to be properly set in order to minimize the reflected power. Nowadays, hybrid DC/RF magnetron sputtering systems are available which bias the electrodes by superimposing an RF voltage

to a DC one so that it is possible to finely tune the system to an extremely wide range of application and target materials.

The characteristics of the deposited film strongly depend from the deposition parameters such has chamber pressure, gas composition, deposition power and time, and substrate temperature. The processes involved in the depositions are quite complicated and involve: sputtering of the target, transportation, chemical reactions, condensation, clustering and film growth. Even thought several models have been developed [142–144], an empirical adjustment of the parameters is usually required in order to achieve a deposited film with specified properties and morphology.

5.2 Sensor structure e film deposition

The sensors presented in this work are arranged in a layered structure basically composed by an alumina substrate and a Nb_2O_5 thin-film deposited on. The section of the sensor is shown in figure 5.3-B. The alumina substrate is specifically designed for the implementation of gas sensors and it is commercially available at a low-cost (about 0.5$/unit) with dedicated platinum strips screen-printed on both faces. In particular, the substrate is quite small, with dimensions of 3 mm × 6 mm and a thickness of 0.5 mm. The platinum strips, whose thickness is about 5 µm, form a couple of Interdigitated Electrodes (IDEs) on the top face and a small heater on the bottom face. Figure 5.3 shows the drawings of the top (B) and bottom (A) faces of the substrate highlighting the main dimensions which are reported in Table 5.1.

The heater is a very important feature of these substrates. In fact, as explained in the introductory material in chapter 4, metal-oxide conductometric gas sensors typically requires a working temperatures in the range of 100 °C to 600 °C. Thus, a proper heating system is required in order to set and stabilize the sensor temperature during the measurements. The heater integrated on the substrate, together with a proper electronic control system, is able to accurately set the working temperature of the sensors with a maximum uncertainty of about 10 °C.

The deposited Nb_2O_5 film is extremely thin with thickness depending on the deposition parameters and, in general, ranging from 100 nm to 1 µm. As shown in figure 5.3-C the sensing film is deposited on the top face covering the inter-digitated electrodes for a total area of about 10 mm^2. However, only a small part of this area, the one confined between the two interdigitated electrodes and highlighted in yellow, is responsible of the effective sensor response. This *effective active area* is 2.06 mm^2. In fact, the film conductivity is very low and the platinum strips create short-circuits for all the remaining film area. The choice of the interdigitated electrodes contributes to decrease the effective sensor resistance by paralleling the elementary film resistance, which otherwise could reach values too high for being measured with normal instrumentation. Figure 5.3-C shows the details of a single interdigitated path. By neglecting the border

and corner effects, it can be seen how the resistance of the single path R_P has two basic contributes: R_A and R_B which are connected in parallel. By considering that this basic path is replied for five times, it results that the total effective sensor resistance can be calculated as a parallel of five R_P contributes. Anyway, it can be noted, how this approach is almost equivalent to transform the interdigitated path into a linear one, as shown in figure 5.3-D. In this case, the equivalent active area has an equivalent length L_{eq} and an equivalent width W_{eq} which can be calculated from the interdigitated dimensions:

$$\begin{aligned} W_{eq} &= e \\ L_{eq} &= 5\,(d + w) + 9\,e \\ S_{eq} &= L_{eq} \cdot t_F \\ A_{ef} &= L_{eq} \cdot W_{eq} \end{aligned} \tag{5.1}$$

where t_F, S_{eq} and A_{ef} are respectively the thickness, the equivalent section and the effective area of the sensing film. Thus, it is possible to calculate the equivalent total sensor resistance as:

$$R_S = \rho \frac{W_{eq}}{S_{eq}} = \frac{\rho}{t_F} \cdot \frac{W_{eq}}{L_{eq}} = \frac{\rho}{t_F} \cdot \frac{e}{5\,(d + w) + 9\,e} \tag{5.2}$$

and, by replacing the interdigitated dimensions, it results:

$$R_S = \frac{\rho}{51.5 \cdot t_F} \tag{5.3}$$

In contrast, considering always the linear electrode structure of figure 5.3-D, but working with equal active area and equal substrate dimensions (L and H), it results:

$$\begin{aligned} A_{ef} &= L_{eq} \cdot W_{eq} = 2.06\ \text{mm}^2 \\ L^*_{eq} &= H_F - s = 3.0\ \text{mm} \\ W^*_{eq} &= \frac{A_{ef}}{L_{eq}} \approx 690\ \text{nm} \end{aligned} \tag{5.4}$$

which results in a total effective sensor resistance of:

$$R^*_S = \rho \cdot \frac{W_{eq}}{S_{eq}} = \rho \cdot \frac{W_{eq}}{L_{eq} \cdot t_F} = \frac{\rho}{4.35 \cdot t_F} \tag{5.5}$$

Therefore, the interdigitated structure decreases the effective film resistance by a factor of about 12 in respect to a simple linear structure with great benefits in terms of costs of the measurement equipment and of noise immunity.

As visible in figure 5.4, the substrates are sold in slices of 14×7 units and, thus, it is required to individually separate each substrate before being processed. The figure

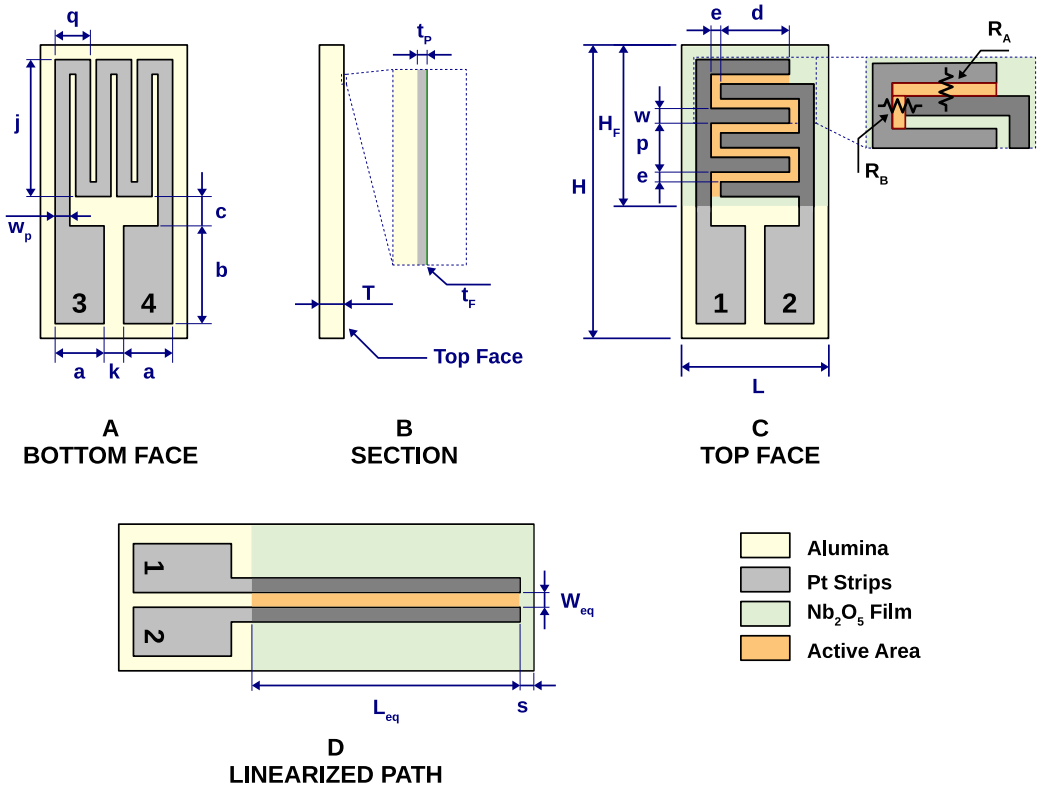

Figure 5.3: Allumina substrate employed in the sensor deposition. A) bottom face with the platinum heater; B) section; C) top face with the platinum interdigitated electrodes and the sensing film deposited on.

Table 5.1: Dimensions of the alumina substrate employed in the sensor development as labeled in figure 5.3.

Label	Dimension	Label	Dimension	Label	Dimension
H	6.0 mm	e	200 µm	a	1.0 mm
L	3.0 mm	s	300 µm	b	2.0 mm
T	0.5 mm	w	300 µm	c	0.6 mm
H_F	3.3 mm	w_p	300 µm	d	1.4 mm
p	1.0 mm	k	400 µm	t_F	0.1 ∼ 1.0 µm
j	2.8 mm	q	0.7 mm	t_P	5.0 µm

also shows an example of sensor prototype after being cut and deposited. In particular, the Nb_2O_5 film is visible on the top face of the sensor as a darker area covering the interdigitated electrodes. The film is almost transparent because of its extremely small thickness.

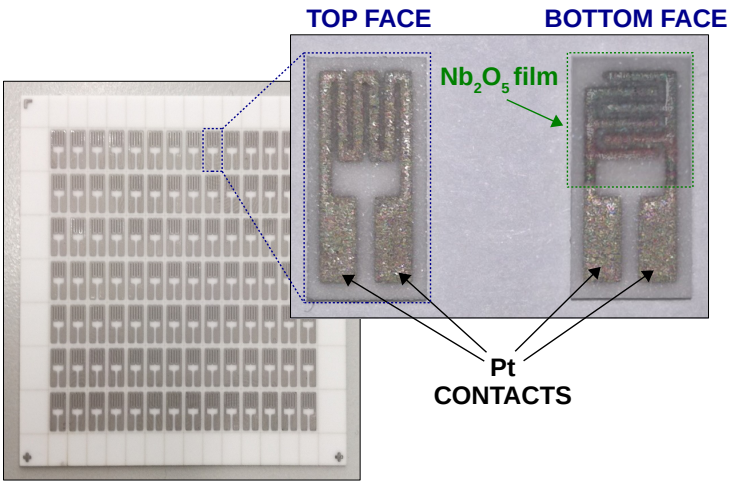

Figure 5.4: A slice of substrates, as sold by the manufacturer and an example of sensor prototype after the Nb_2O_5 film deposition.

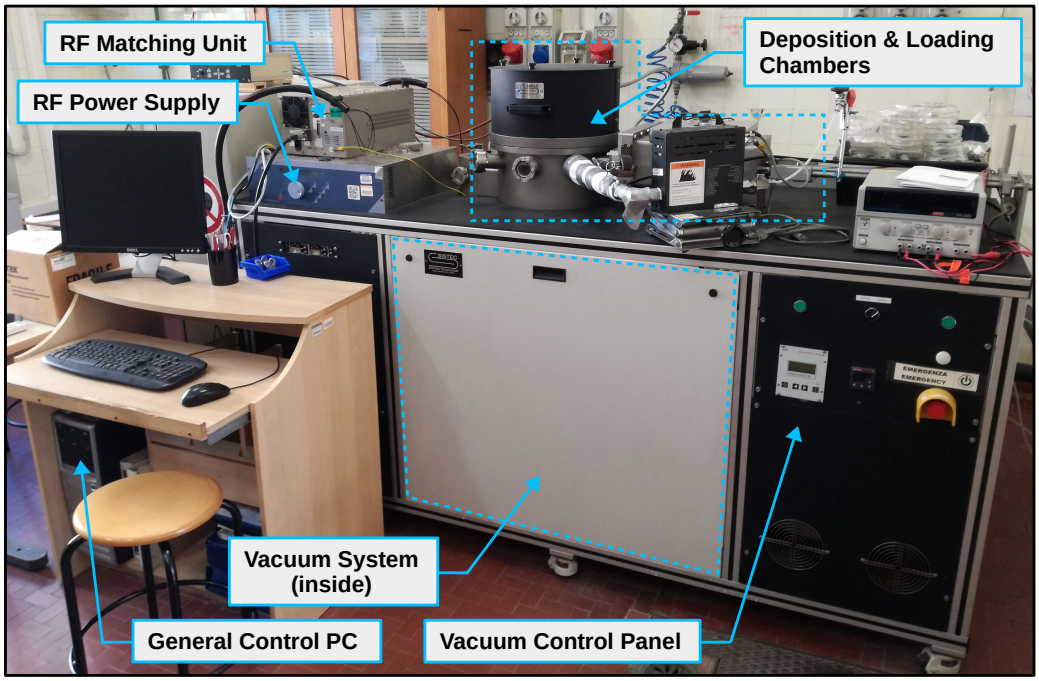

Figure 5.5: The reactive magnetron sputtering reactor employed in the sensor depositions.

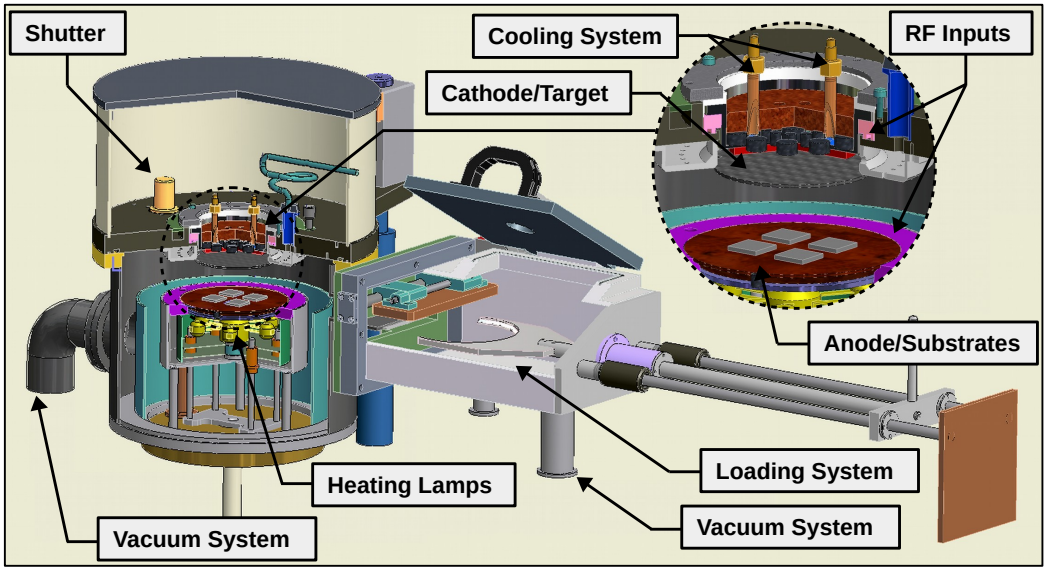

Figure 5.6: 3D detail of the reactor deposition chamber.

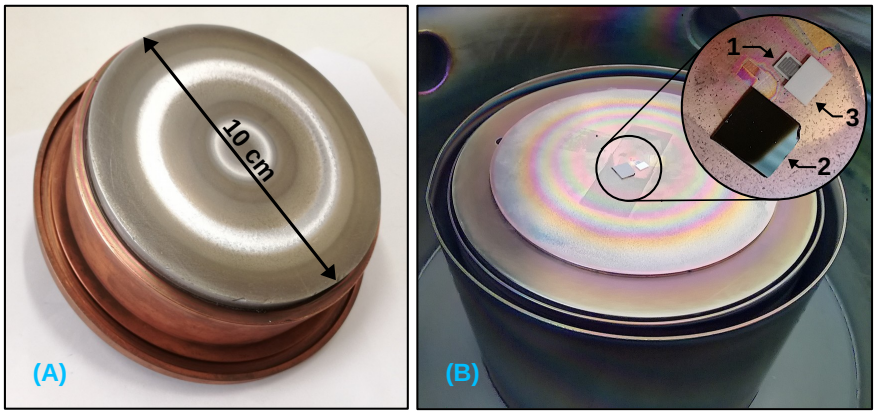

Figure 5.7: A) Niobium target employed in the sensor depositions; B) alumina substrate (1), Si reference (2) and mask arrangement (3) placed on the ground electrode and ready for the deposition.

The Nb_2O_5 sensing films for all the developed prototypes have been deposited on the small alumina substrates (described in section 5.2) by reactive RF magnetron sputtering in a lab-scale capacitively-coupled parallel-plate-reactor employing an unbalanced

magnetron configuration (type 2). Figure 5.5 shows the reactor employed in the depositions carried out at the Department of Applied Science and Technology, Politecnico di Torino, Turin, Italy. The cylindrical deposition chamber allows one to deposit substrates with diameters of maximum 15 cm. The cathode electrode, fixed on the top side of the chamber, supports circular targets with a diameter of 10 cm and it features a water cooling system in order to stabilize the target temperature during the deposition (see figure 5.6). The top side of the chamber is fixed on a motion system which allows one to easily open and close the chamber itself. On the bottom side of the chamber there is the anode (ground electrode), on which the substrates to be deposited can be arranged. Directly under the ground electrode there are seven heating lamps which make possible to control the substrate temperature from room temperature to about 600 °C. A loading utility featuring a small loading chamber can be used to insert the substrates to be deposit without opening the main chamber. The reactor vacuum system features a rotary pump (PFEIFFER, model: DUO20C) and a turbo molecular pump (PFEIFFER, model: TPH261PC). A set of mass flow controllers are employed to control the deposition gas mixture and the relative fluxes. In order to bias the electrodes a RF power supply (TRUMPF, model: PFG1000RF, frequency: 13.56 MHz, maximum power: 1 kW) is connected to the electrodes by using a RF matching network (TRUMPF, model: PFM1550A). The reactor is controlled by a PC running a dedicated software which allows one to set and monitoring all the operating parameters.

A niobium target (99% purity), shown in figure 5.7-A, has been employed in all the depositions while the plasma has been fed with a mixture of Ar (99% purity) and O_2 (99% purity) at the flow rates respectively of 50 sccm and 20 sccm[1]. Total pressure inside the chamber was very low, in the order of 10 Pa with a plasma floating temperature $T_f < 60$ °C.

Depositions times were in the range of 30 min to 60 min with an RF power in the range of 150 W to 500 W at the fixed frequency of 13.56 MHz. Table 5.2 reports the four most performing samples and their principal deposition parameters.

Before each deposition, the alumina substrate was cut from the slice, pre-conditioned in oven for 4 h at a temperature of 400 °C in order to remove any possible residue due to the substrate production (electrode screen-printing). Subsequently, each substrate was cleaned in ethanol by using an ultrasonic cleaning machine, and then dried in air at room temperature.

After the pre-conditioning, each substrate was placed inside the deposition chamber centering it on the ground electrode (anode). A small silicon slice (about 1 cm^2, cut from a Si-wafer) was put beside the substrate as reference used for the film characterization. In fact, the alumina substrates are not flat because of the platinum electrodes printed

[1] sccm: "*standard cubic centimeter per minute*". 1 sccm = 1690 cm^3/s being the standard values for pressure and temperature respectively 1 atm and 273 K, and being the pressure inside the deposition chamber very low (∼ 10 Pa).

Table 5.2: Summary of the deposited Nb_2O_5 sensing films and relative deposition parameters.

Sample	Dep. Power (W)	Dep. Time (min)	Film Thickness (nm)
#1	150	60	160
#2	250	30	200
#3	500	30	500
#4	500	60	900

on its sides and, thus, it is not possible to characterize the thin-film thickness and morphology directly on the substrate. In contrast, the silicon slice is characterized by a very smooth surface (roughness lower than few nm) and, thus, it is very suitable for such a type of analysis. The substrate was put with the interdigitated electrodes facing up towards the target and a small alumina rectangular slice was put over the substrate in order to mask and protect the sensor connections. The arrangement of the substrate and the reference slice is shown in figure 5.7-B.

Subsequently, the chamber was closed and cleaned in a pure-Ar discharge with the deposition shutter closed in order to avoid any possible contamination. Subsequently, the shutter was open and after the introduction of O_2 at the proper rate, the deposition discharge was started. The matching unit was set properly to minimize the reflected power. All the parameters were maintained constant for the whole deposition time. After the deposition, each sensor was fully characterized, as explained in the following section.

5.3 Sensor characterization

After the sensing film deposition, all the realized prototypes have been preliminary tested. Subsequently, the most promising sensors, reported in Table 5.2, have been fully characterized to assess their sensing performance.

The first step was to characterize the morphology and the structure of the deposited film with a Field Emission Electron Scanning Microscope (FESEM). Then, the chemical composition of the film was assessed by using the X-ray Photo-electron Spectroscopy (XPS) analysis. Both the characterizations were performed at the Department of Applied Science and Technology, Politecnico di Torino, Turin, Italy.

Electrical and sensing characterizations were, instead, performed by means of a dedicated experimental bench specifically designed for gas measurements at the Department of Engineering at University of Messina, Messina, Italy. In particular, an individual calibration of the substrate heaters has been carried out with the aim to reduce the uncertainty of the sensor working temperature. Subsequently, the sensor response of the prototypes has been assessed towards acetone and ethanol taking into account

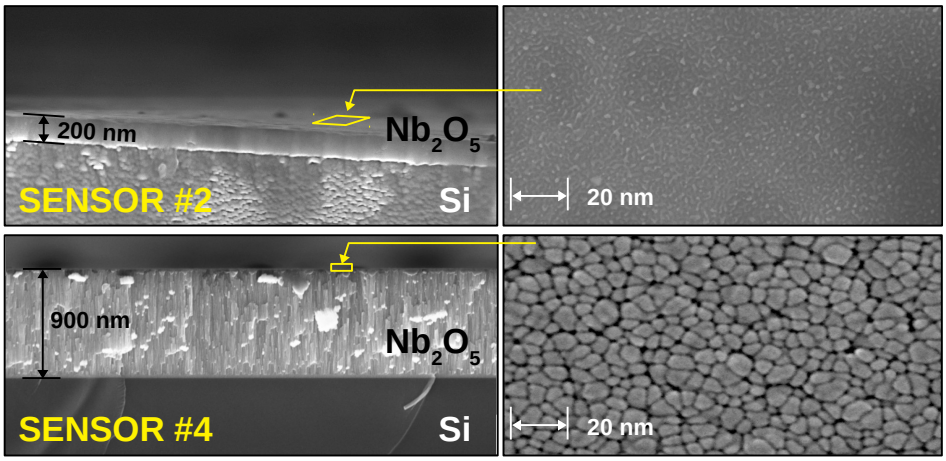

Figure 5.8: FESEM images of the Nb_2O_5 film for sensors #2 and #4.

its temperature dependence and also including several selectivity tests towards possible interferent gases. Finally, response and recovery times has been evaluated together with the sensor repeatability and stability.

5.3.1 Morphology and structure of the sensing film

The morphology and the structure of the deposited films were characterized by using the Field-Emission Electron Scanning Microscope (FESEM) Supra 40 Zeiss. Several pictures were taken by using the reference silicon substrates deposited together the sensors, as described in the section 5.2. The characterization highlighted a strong difference between the morphology of thin and thick films. Thick films, such as prototypes #3 and #4, are characterized by a quite porous structure composed by thin vertically aligned nano-rods whose diameter is in the order of 15 nm. Instead, thin films, such as prototypes #1 and #2, have a compact structure with a smooth surface and no visible porosity. From the characterization performed on the different samples, it seems that the threshold between the two different structures is around a thickness of 500 nm. Moreover, the deposition power seems to have an effect on the morphology as well. Films deposited with an high power looks more porous and less smooth than films deposited with low powers ($P < 250W$). As an example, figure 5.8 shows the structure and the morphology for prototypes #2 and #4. In the figure it is evident the different structure between the two prototypes: sensor #2 has a thickness of about 200 nm with a compact structure and a smooth surface with almost no porosity. Instead, prototypes #4 has a thickness of about 900 nm and the strusture is very porous.

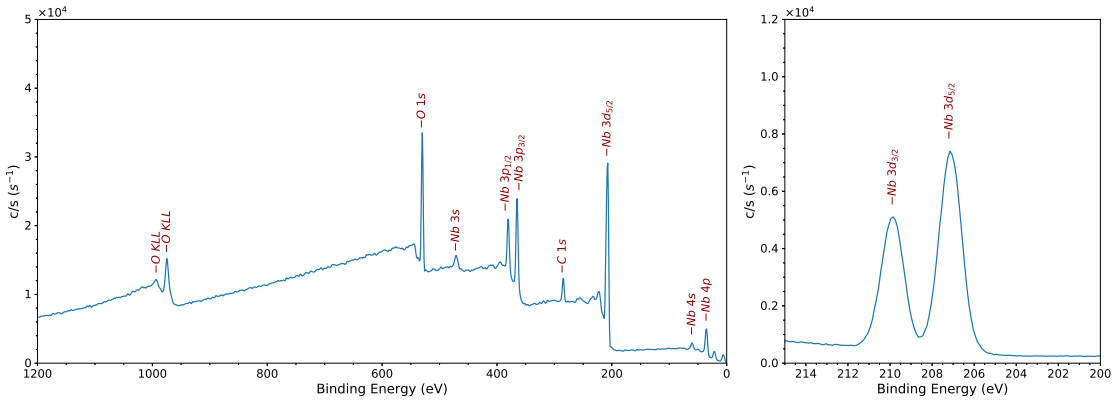

Figure 5.9: XPS spectrum acquired on the prototype #3 and the high-resolution scanning of the Nb 3d peaks.

5.3.2 Chemical characterization of the sensing film

A chemical characterization of the deposited film has been carried out with the aim to verify that the deposited film was mainly composed by Nb_2O_5. Thus, a XPS analysis has been performed on all the deposited prototypes by means of a PHI model 5000 electron spectrometer which was equipped with a monochromatic aluminum source (1486 eV). All the measurements were performed employing a power of 25 W, and an operating pressure below 5×10^{-6} Pa. A pass-energy of 11.75 eV was set for performing each high-resolution scanning. High-resolution spectra of the C 1s, O 1s and Nb 3d peaks were acquired for each prototype.

The acquired spectra were corrected by using the C 1s line as energy reference. Thus, all the binding energies were shifted so as to center the C peak on an energy of 284.6 eV. In fact, such carbon line, which is mainly due to environmental contamination, is known to be characterized by such a binding energy.

The spectra acquired on all the prototypes, regardless of the deposition parameters, revealed the same chemical composition with negligible difference among their spectra. As an example, figure 5.9 shows the XPS spectrum acquired on the prototype #3 along with the high-resolution scanning of the Nb 3d peaks. As it is visible from the graph, C, O and Nb are the only elements detected by the analysis. Moreover, it is clearly visible the doublet composed by the lines Nb $3d_{3/2}$ and Nb $3d_{5/2}$, respectively centered at binding energies of 209.8 eV and 207.1 eV. These peaks, characteristic of the Nb 5+ state, confirm, as expected, that the film composition is niobium(V) pentoxide, Nb_2O_5.

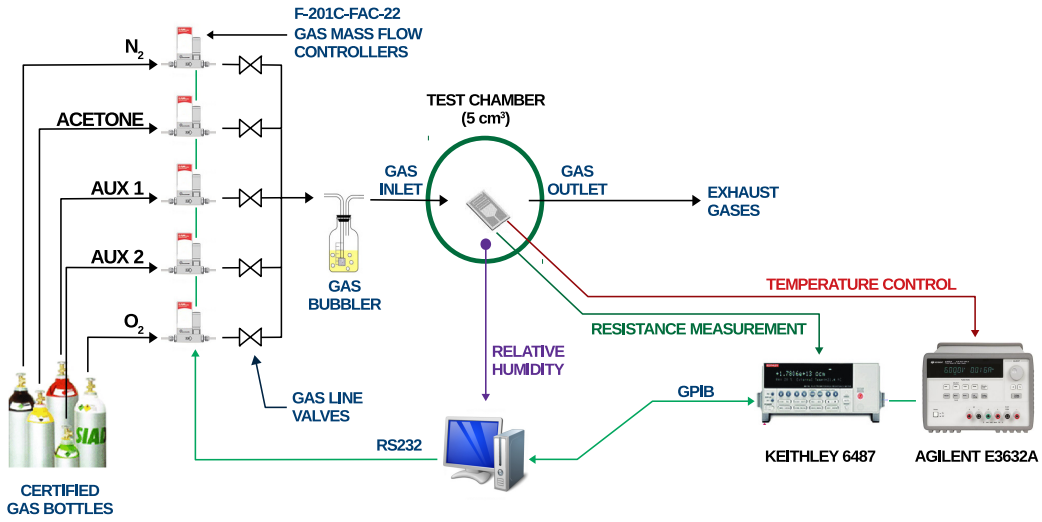

Figure 5.10: Block diagram of the measurement bench employed for the characterization of the sensing properties of the prototypes.

5.3.3 Experimental characterization equipment

Subsequently, the electrical and sensing performance of the prototypes were assessed by using a dedicated measurement bench specifically designed for the characterization of gas sensors. The bench, whose block diagram is shown in figure 5.10, is available at the Department of Engineering, University of Messina, Messina, Italy. The bench features a small sampling chamber with an internal volume of about 5 cm^3. The small volume of the chamber turns out in a quick response to variations of the gas composition even at very low flow rates. The sensor under test (SUT) is fixed on the side with the sensing area facing upwards. Finally, an inlet and outlet allow the gas to properly flow inside the chamber. The gas mixture is obtained by using a set of certified gas bottles as source and mixing the gases in the proper ratio by using a set of five mass flow controllers (BRONKHORST, model: F-201C-FAC-22). These mass flow controllers can be controlled by a computer and are able to set the gas flow rate with a typical uncertainty of 2%. For each mass flow controller a valve was added to open or close abruptly the relative gas flow. The use of these valves, instead acting directly on the mass flow controllers, turns out in a very quick control of the gas flow because no stabilization delay time is added. This, of course, results in a more accurate estimation of the sensor response time. Furthermore, a gas bubbler is connected to the inlet gas line. This way, by employing a humidity probe inside the chamber it is possible to accurately change the relative humidity of the gas mixture. A digital power supply (AGILENT, model: E3632A), connected to the sensor heater (contacts 3–4 in figure 5.3),

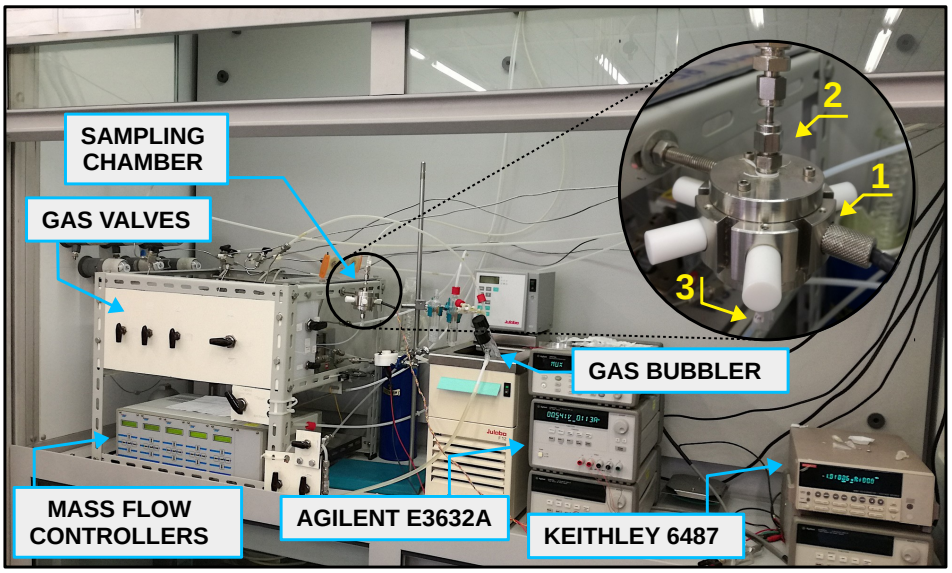

Figure 5.11: The measurement bench employed in the prototype characterization with detail of the sampling chamber: sensor under test (1), gas inlet (2) and gas outlet (3).

is employed to control in a closed-loop the sensor working temperature. In particular, the substrate heater is used both as actuator and temperature probe:

- the power supply, connected to the computer by means of a GPIB Interface, drives the heater with a specified output voltage and at the same time read-out the output current;
- a software on the computer calculates the heater resistance as $R_H = V_O / I_O$ and, from it, the substrate temperature by using the heater characteristic curve *resistance vs temperature*;
- a closed-loop proportional-integral-derivative control (PID), implemented in the software, stabilizes the sensor working temperature by properly adjusting the output voltage.

Finally, a picoammeter/voltage source (KEITHLEY, model: 6487) is connected to the SUT contacts 1 and 2 (see figure 5.3). The instrument, connected always by means of the GPIB Interface, measures accurately the resistance of the sensing film (sensor response) by forcing a known voltage and reading out the flowing current. By using this setup, it is possible to measure the sensing film resistance with a typical uncertainty

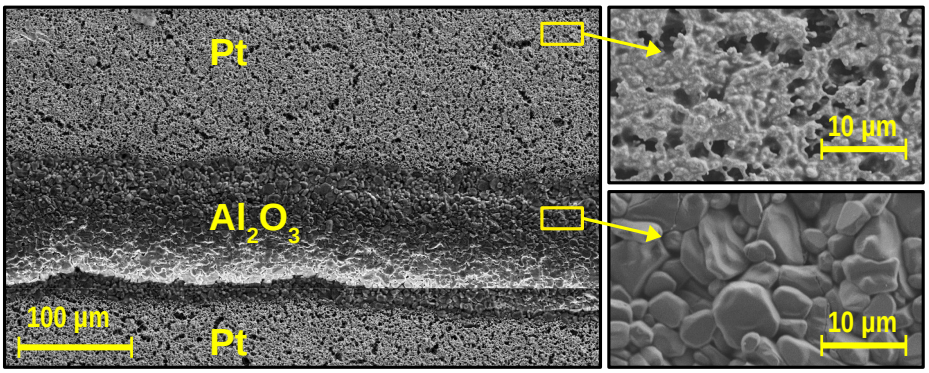

Figure 5.12: Micrography with high-magnification details of the sensor substrate taken over the interdigitated area. In the image are visible two platinum strips separated by alumina and the different microstructure of the two materials.

of about 0.2% which can be neglected in respect to the other uncertainty sources. An acquisition software running the the computer acquires the data visualizing them in real-time graphs, and at the same time, it stores them in *csv* files for being subsequently processed. Additionally, the described measurement bench allows one to program the measurement steps (for example a sequence of different gas concentrations or temperature steps) and automatize the measurement process. This is a very useful feature because measurements on gas sensor can require time in excess of several hours. A photo of the measurement bench with a detail of the sampling chamber is shown in figure 5.11.

A conditioning of each prototype at 400 °C for 4 h was carried out before any further characterization in order to chemically stabilize the sensing film and get rid of any possible contaminants.

5.3.4 Heater characterization

The platinum heater, shown in figure 5.3-A, has a total length of about 20 mm, a width of 300 µm and a thickness of about 5 µm. It is characterized by a very porous structure (see figure 5.12) due to the screen-printing manufacturing process and the subsequent thermal treatment. The room-temperature heater resistance R_r is about 4 Ω with a dispersion of about 0.5 Ω among the different substrates. Also the temperature coefficient α has a quite large dispersion in the range of 10×10^{-3} ΩK^{-1} to 20×10^{-3} ΩK^{-1}.

Table 5.3: Room-temperature heater resistance and temperature coefficient of three different substrates evaluated with a linear fitting of the experimental data.

Substrate	R_r (Ω)	α (ΩK^{-1})
A	4.61	17.36×10^{-3}
B	3.92	12.03×10^{-3}
C	4.23	11.70×10^{-3}

As explained in the previous section, the heater is used both to control and measure the sensor temperature by employing a close-loop PID control. By inverting the following relation:

$$R = R_r + \alpha (T - T_r) \tag{5.6}$$

it results:

$$T = T_r + \frac{1}{\alpha}(R - R_r) \tag{5.7}$$

which can be used to evaluate the sensor temperature from the measurement of the heater resistance. Unfortunately, the uncertainty of the set temperature is not acceptable with such a large dispersion of the parameters R_r and α.

With the aim to get rid of this uncertainty, which indirectly strongly affects the accuracy of the sensor working temperature, a calibration of each single substrate was carried out by acquiring the heater resistance at several temperatures in the range of 30 °C to 400 °C. A power supply (AGILENT, model: E3632A) has been connected to the heater contacts and employed to supply the heater with increasing power steps. The substrate temperature has been measured by a thermocouple fixed to the substrate with a thermal paste. After the substrate temperature stabilized, the heater resistance has been measured with the power supply itself. This way, each substrate heater was characterized and the relative calibration curve (heater resistance vs temperature) was employed to estimate, by a linear fitting of the experimental data, the parameters R_r and α for each individual substrate. These parameters were stored within the PID control software (see previous section) in order to properly control the sensor working temperature with an uncertainty as less as possible with the employed equipment. This uncertainty can be estimated in about 10 °C by considering that the power supply is able to measure the heater resistance with an uncertainty of less than 2%. Figure 5.13 shows, as an example, the calibration curves acquired for three different substrates. The relative parameters are reported in Table 5.3.

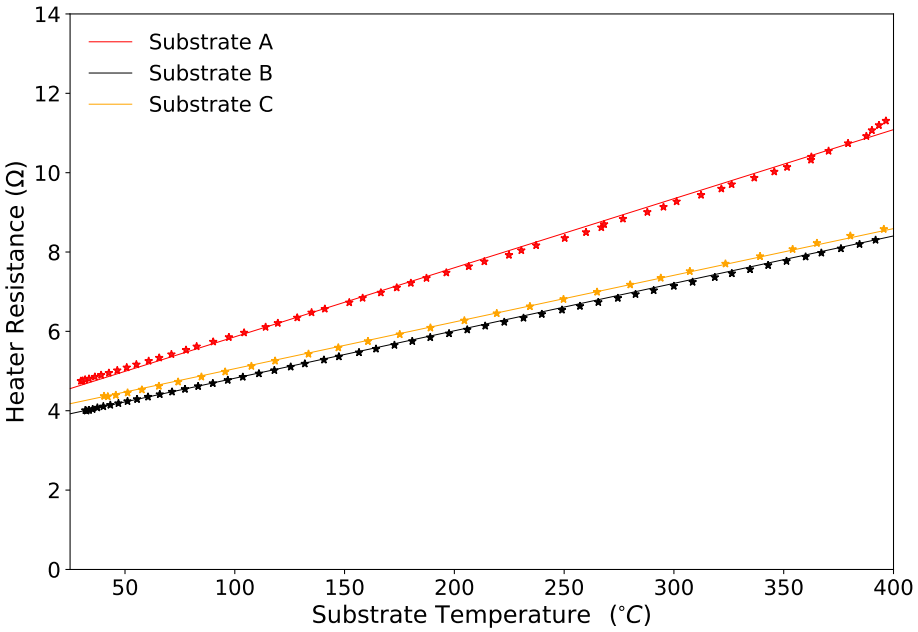

Figure 5.13: Calibration curves for three different heaters obtained by linear fitting of the experimental data.

5.3.5 Temperature dependence of the sensor response

A very important parameter affecting the sensing response of a conductometric metal-oxide gas sensor is surely the working temperature. As explained in the introductory material in chapter 4, sensitivity, selectivity and response times are all strongly affected by the working temperature. In fact, the sensing mechanism of conductometric gas sensors is based on chemi-sorption/chemi-desorption and diffusion processes acting on the sensing film surface, and all of them strongly depends on temperature. Thus, a characterization of the prototype responses to acetone at different working temperature was carried out with the aim to identify the best working conditions for each one of the selected sensors.

Dry synthetic air was employed as carrier gas by setting two mass flow controllers so as to have a mixture of oxygen at 20% and nitrogen at 80%. Additionally, a third mass flow controller was set in order to have an equal acetone concentration of 5 ppm along all the measurements and the different prototypes. By employing the closed-loop PID controller described in section 5.3.3 and properly adjusting the heating power, the working temperature was changed in the range of 200 °C to 400 °C in five steps. After the temperature stabilized, the acetone was added to the carrier gas (synthetic dry air) at the fixed concentration of 5 ppm by opening the relative valve, and the sensor response was acquired in terms of resistance variation.

Figure 5.14 shows the results obtained on three different sensor prototypes: #1, #2

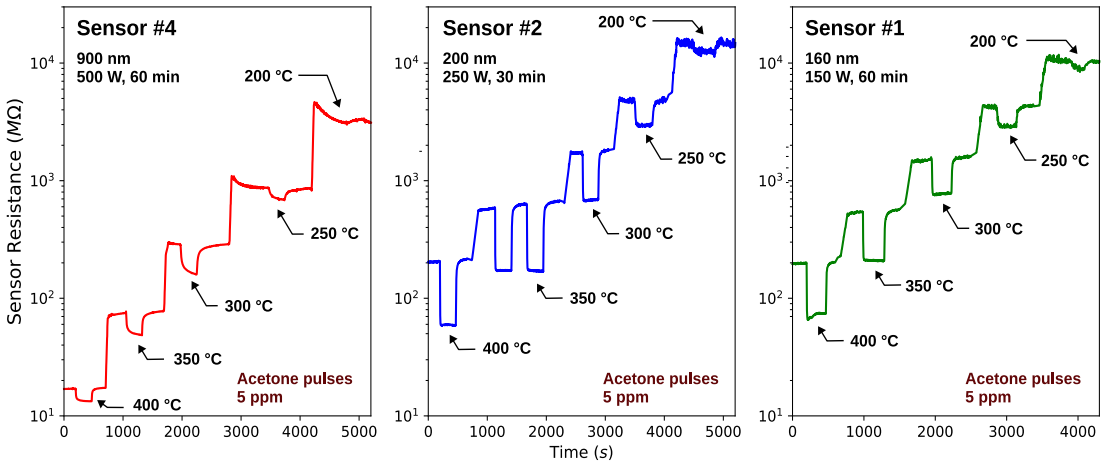

Figure 5.14: Response to 5 ppm of acetone at different temperatures for three of the selected prototypes.

and #4. As expected, the sensor resistance decreases when temperature increases, being the sensing material an oxide. In particular, all the sensors have a extremely limited response at 200 °C with a resistance in the order of 10 GΩ. The response increases significantly with the increasing of the temperature reaching its maximum between 300 °C and 400 °C with a resistance in the order of 100 MΩ. It is immediately possible to note how the two sensor #1 and #2 outperform largely sensor #4 in terms of relative response.

The prototypes relative responses as function of the working temperature has been calculated from the experimental data. It is visible how all the sensors are characterized by the typical bell-shaped temperature characteristic which is due to the balance the gas chemi-sorption/desorption and diffusion processes occurring on the sensing film surface. The responses with associated the relative deposition parameters are shown in figure 5.15, which allows one to directly compare the sensor performance. Here, it is visible how thinner films, especially the sensor #2, are characterized by a response significantly larger than the thick one (#1). This can be explained by taking in consideration the sensing mechanism of this type of sensors. The resistance variation of the sensing film occurs as consequence of the establishment of a depletion layer (or an accumulation layer for P-type semiconductors) due to the chemisorption of the air oxygen and the partial removal of these bonds because of the reaction involving the target gas (acetone) and the chemi-sorbed oxygen itself. This is a surface process due to surface bonds and it does not involve the bulk material. In the case of a thin film, the ratio between the thickness of the depletion layer and the thickness of the film can easily reach values close to the unity, being most of the film depleted (figure 4.5). In contrast, this ratio remains small in the case of a thick film. This means that in thick films the bulk conduction is the predominant effect and, as consequence, they exhibit

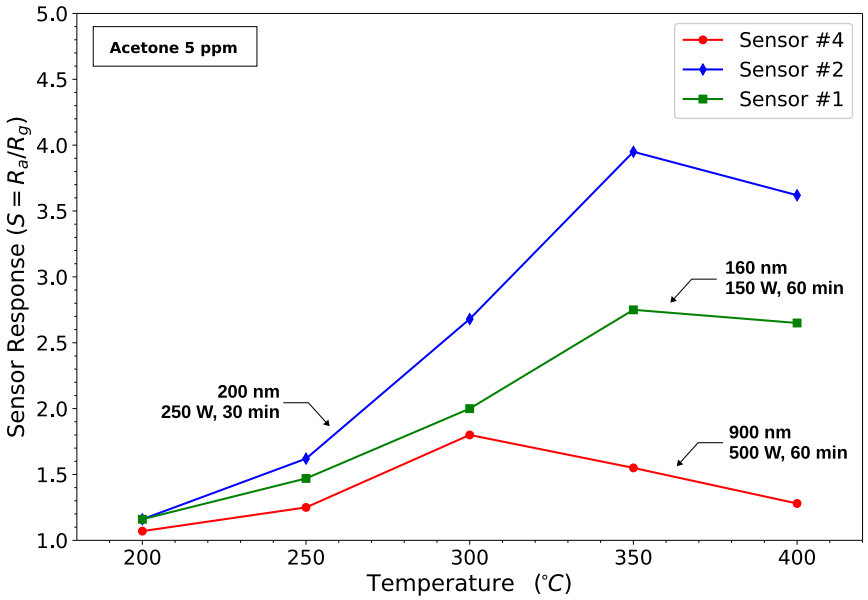

Figure 5.15: Temperature dependence of the prototype responses to 5 ppm of acetone in the temperature range of 200 °C to 400 °C.

a smaller relative response when compared with thin films, where surface effects and depletion layer modulation due to the gas chemisorption predominate. Nevertheless, it is very interesting to note how sensor #1 and sensor #2 have a quite different response event though their thickness is quite similar, and it is also interesting that #2 have a better response than sensor #1 event thought it is thicker than the latter. This can be explained only by taking into consideration the deposition parameters which turned out in a slight different film morphology and sensing performance. Thus, it seems there exists some optimal combination between thickness and deposition parameters, such as deposition power, which results in a enhanced sensitivity of sensor #2.

It is also possible to note how thinner sensors reach the maximum sensitivity at 350 °C and, instead, the sensor #1 has the best performance at a temperature of 300 °C.

Finally, the resistance in pure air, R_a has been evaluated for each prototype in the same temperature range, and the resulting data are showed in figure 5.16. It can be seen how resistance decreases with the increasing of the temperature following a quasi-exponential trend. It is interesting to note how the two thin prototypes exhibit an almost equal trend, but film #1 has a resistance slightly lower than sensor #2, event though the former is thinner than the latter (#1: 160 nm; #2: 200 nm). This can be explained taking in consideration the deposition parameters of the two films. In fact, the film #1 has been deposited with a lower power than the film #2 (#1: 150 W; #2: 250 W). This turns out in a deposition rate that is smaller in the sample #1. As consequence, there is the

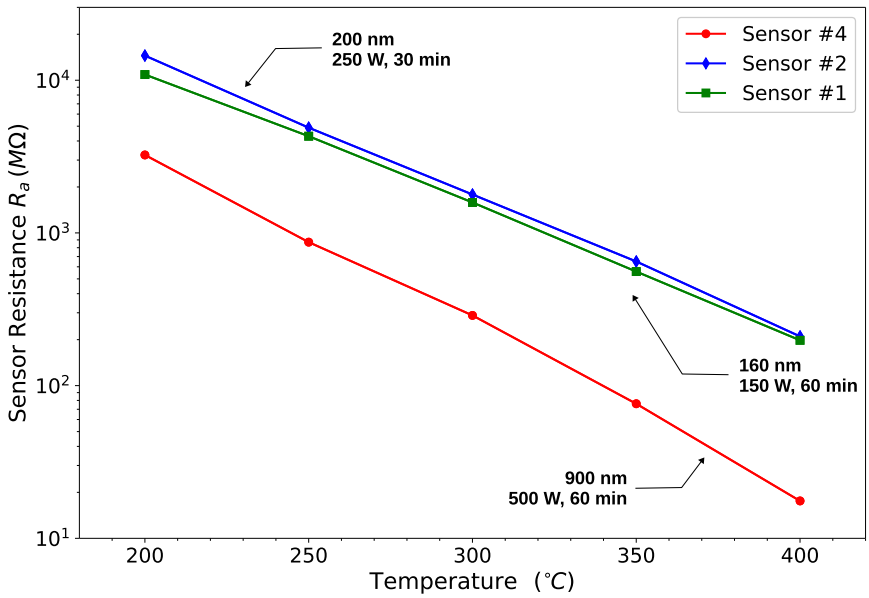

Figure 5.16: Temperature dependence of the sensor resistance in pure air in the temperature range of 200 °C to 400 °C.

deposition of a more compact and stress-free film which is characterized by a slightly higher conductivity in respect of film #2. Finally, prototype #4 has of course a much lower resistance being it much more thick than the other two sensors.

In conclusion, this characterization in temperature showed how thin sensors perform much better than thick ones in terms of response to acetone within all the tested temperature range, but achieving the best performance between 300 °C and 350 °C. In particular, sensor #2 exhibit a response larger than sensor #4 by a factor greater than 2.

5.3.6 Response and recovery times

Subsequently, the prototypes have been characterized in term of response time. Response time of a gas sensor can be an important factor in several applications such as the breath analysis. In fact, having a fast-responding sensor means to decrease the breath sampling time with significant benefits, such as increasing the measurement accuracy (being the measurement less affected by the natural variability of the breath) and, at the same time, reducing patient stress.

The same carrier gas mixture (O_2: 20% and N_2: 80%) has been employed during the measurement with periodical addictions of acetone in a concentration so as to obtain several 5 ppm pulses. The acetone flow has been controlled by opening and closing the relative valve in order to keep rise and fall times as low as possible. The responses to

steps of acetone from 0 ppm to 5 ppm and back from 5 ppm to 0 ppm for the three prototypes (#1, #2 and #4) have been acquired at four different temperature in the range of 250 °C to 400 °C, with the aim of determining respectively the response and recovery times, and how these depend from the working temperature. In order to make the transients comparable, they have been shifted in time and normalized in amplitude so as to obtain all the transitions overlapping one on the others with a normalized amplitude between 0 and 10. This way, it is possible to have an immediate evaluation of the sensor performance. Figure 5.17 shows the normalized transients for sensors #2 and #4 for both positive (left) and negative (right) steps of acetone. Data acquired on sensor #1 have not been reported here for clarity of the graphs, being them almost equal to that of sensor #2.

The dramatically difference between the two sensors is clearly evident: sensor #2 responds to the variation of acetone concentration much quicker than sensor #4. Same behavior is visible for the sensor recovery. Moreover, it can be noted as both response and recovery times decreases with the increasing of the temperature, even though temperature dependence is almost negligible for the sensor #2.

Response and recovery times have been calculated by evaluating the time elapsed between 10% and 90% of the transition. Figure 5.18 shows the temperature dependence of response and recovery times for both the sensors #2 and #4.

The response of sensor #2 is extremely fast with a response time of about 5 s almost constant in the tested temperature range. Best performance have been recorded at a temperature of 350 °C at which the response time is only 3.6 s. This is a very excellent result also considering that sensor achieves both best response time and best sensitivity at the same temperature. Sensor recovery is also quite quick with a recovery time in the order of 50 s which slightly decreases with the increasing of temperature and reaching the best performance of 40 s at 400 °C.

Sensor #4 features, instead, a quite different behavior. Response to the same acetone concentration is much slower and largely dependent from the working temperature. The response time goes from about 130 s at 250 °C to about 45 s at 400 °C. The recovery time follows a similar trend going from about 140 s at 250 °C to 65 s at 400 °C.

This large difference in response and recovery times between the two prototypes, even thought they are characterized by the same chemical composition (Nb_2O_5), can be explained taking in consideration the different morphology and the thickness of the two sensing films. As described in section 5.3.1, the film deposited on the sensor #4 is very porous and has a thickness of about 900 nm. This turns out in a quite long time required by the target gas molecules (acetone, in this case) to completely diffuse in and out the microstructure and interact with the sensing film surface. Instead, sensor #2 is characterized by a thin, compact and flat sensing film with almost no porosity, and this turns out in a immediate interaction with the sensing surface and virtually no time is required for the diffusion process. This also explains the different temperature dependence. Diffusion processes strongly depend on temperature and, in general, diffusion speed increases with temperature. As explained above, response times of sensor #4 are

Table 5.4: Summary of the response and recovery times obtained by the sensors #2 and #4. Column four highlights the performance achieved at the best-sensitivity temperature.

Sensor	max time (s)	min time (s)	best-sensitivity time (s)
#2 (response time)	5.7 (250 °C)	3.6 (350 °C)	3.6 (350 °C)
#2 (recovery time)	52 (250 °C)	40.9 (400 °C)	48.8 (350 °C)
#4 (response time)	129 (250 °C)	46.1 (400 °C)	116.5 (300 °C)
#4 (recovery time)	140.9 (250 °C)	63.8 (400 °C)	125.8 (300 °C)

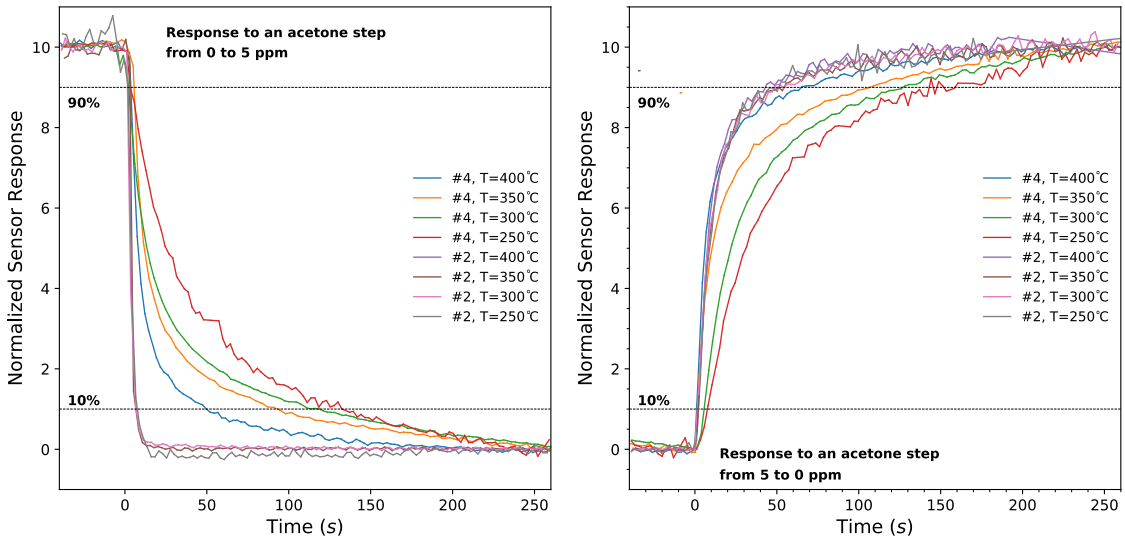

Figure 5.17: Response to 5 ppm steps of acetone for prototypes #2 and #4 at four different temperatures in the range of 250 °C to 400 °C.

dominated by the diffusion processes inside the porous film and they largely decrease with the temperature because of the increasing of the diffusion speed. In contrast, no diffusion occurs in the chemisorption of the sensing film #2 and this turns out in a negligible temperature dependence of the response times.

Table 5.4 reports a summary of the response times for both the prototypes. By considering the best-sensitivity temperature, it results that sensor #2 responds about 32 times quicker than sensor #4, and it recovers in less than half the time required by sensor #4.

In conclusion, this characterization highlighted the extremely fast response of the prototype #2 with a response time of about 3.6 s at 350 °C, temperature at which the sensor also exhibits the best sensitivity. A much slower response has been, instead, recorded for the sensor #4 with times exceeding two minutes. This makes prototype #2

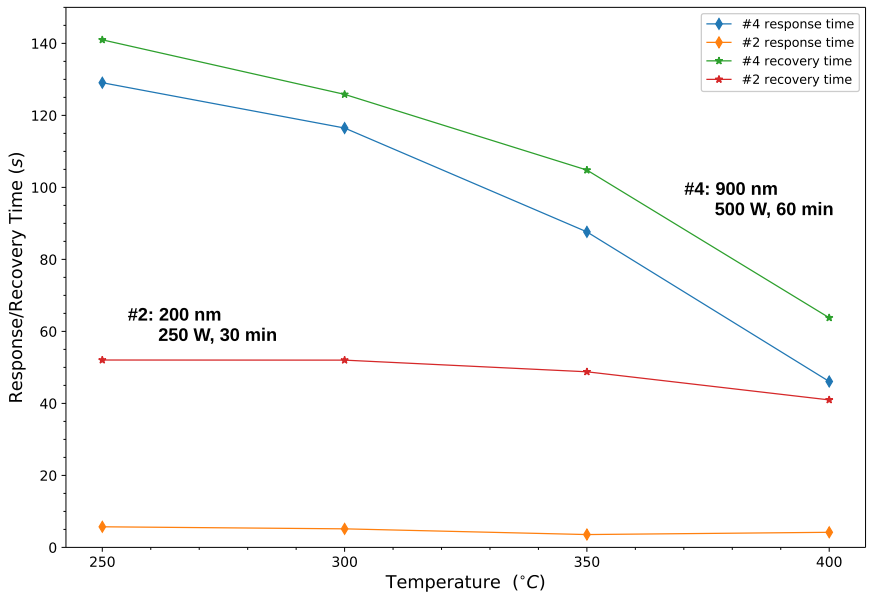

Figure 5.18: Temperature dependence of response and recovery times for the two sensors in the temperature range of 250 °C to 400 °C.

very suitable for the breath analysis because it is able to reach a stable measurement within few breaths with the benefit of increasing accuracy and reducing patient stress.

5.3.7 Sensor sensitivity and selectivity towards acetone

The described characterizations of sensitivity and response times, and their dependence from temperature, allowed one to determine the optimal working temperature for the tested prototypes. In particular, sensor #2 and sensor #4 reach the best performance at temperatures respectively of 350 °C and 300 °C. Furthermore, the same characterizations put in evidence how sensors #1 and #2 have similar behaviors, but the latter outperforming the former by a factor of about 1.6 in terms of sensitivity. Therefore, it was decided to focus the remaining characterizations only on sensors #2 and #4, making them operate at their optimal working temperature.

Thus, sensitivity of the two sensors was fully characterized at several acetone concentrations with the same measurement setup. A proper amount of acetone was added in several steps to the carrier gas mixture (O_2: 20%, N_2: 80%) in order to generate pulses with specified acetone concentration. The responses for sensors #2 and #4 were acquired and are shown respectively in figures 5.19 and 5.20 (graph on the left). The response increases with the increasing of the acetone concentration and, as expected, sensor #2

outperforms #4 in terms of sensitivity. It is interesting to observe how, for both the sensors, the resistance perfectly recovers to its reference value R_a after the removal of the acetone.

The relative response S was calculated for both the sensors from the experimental data by employing the relation:

$$S = \frac{R_a}{R_g} \tag{5.8}$$

and the obtained sensitivity curve is shown in figures 5.19 and 5.20 (graph on the right).

In particular, the relative response of sensor #2 increases almost linearly but, as soon as, the acetone concentration reaches about 3 ppm a saturation affect starts to be visible. The saturation becomes more significant for concentrations higher than 7 ppm, and already at a concentration of 12 ppm the sensor can be considered saturated.

A similar situation is visible for sensor #4, but at much higher concentrations. In fact, the sensor response remains almost linear up to 10 ppm. Saturation starts to be significant only for concentrations above 40 ppm.

Saturation, the progressive reduction of the sensor response when the target concentration increases, is a common effect with this kind of sensors. It is mainly due to the limited the number of chemisorption centers available on the sensing film surface. As soon as the target gas increases, the number of free centers decreases. Thus, saturation is related to the equivalent sensing surface of the film. This explains the reason why the thick sensor saturates at concentrations much higher than the thin one.

First-order and second-order fittings of the experimental data were carried out in order to determine approximated empirical relations able to express the relative response as function of the acetone concentration:

$$\begin{aligned} S &= bX + c \\ S &= aX^2 + bX + c \end{aligned} \tag{5.9}$$

where X is the acetone concentration expressed in ppm. Table 5.5 reports the fitting coefficients for both the relations and both the sensors, together with the maximum allowed concentration, X_{max}. In fact, linear relation can model the response of sensor #2 and #4 with good accuracy only below 3 ppm and 10 ppm, respectively. By inverting these relations and replacing the numerical values of the coefficients it is possible to model the response of the two sensors and to determine the gas concentration by measuring the relative variation of the sensor resistance. Thus, one obtains:

$$\begin{aligned} X &= 4.16 \cdot (S - 1) \quad (\mathrm{X} \leqslant 3\,\mathrm{ppm}) \\ X &= 13.1 - \sqrt{206 - 35.1 \cdot S} \quad (\mathrm{X} \leqslant 12\,\mathrm{ppm}) \end{aligned} \tag{5.10}$$

for sensor #2, and:

Table 5.5: Fitting coefficients obtained from the sensitivity curves of sensors #2 and #4 together the correspondent maximum allowed concentration, X_{max}.

Coefficient	#2 - 1^{st} order	#2 - 2^{nd} order	#4 - 1^{st} order	#2 - 2^{nd} order
a	-	-0.0285	-	-0.0013
b (ppm^{-1})	0.6664	0.7465	0.2389	0.2473
c (ppm^{-2})	1.0014	0.9851	1.0145	1.0156
X_{max} (ppm)	3	12	10	50

$$\begin{aligned} X &= 1.5 \cdot (S-1) \quad (\mathrm{X} \leqslant 10\,\mathrm{ppm}) \\ X &= 122 - \sqrt{15900 - 1000 \cdot S} \quad (\mathrm{X} \leqslant 50\,\mathrm{ppm}) \end{aligned} \tag{5.11}$$

for sensor #4.

Another very important feature of a gas sensor is selectivity, defined as the capability of the sensor to have a high sensitivity towards the target gas and, at the same time, to have a low response to other possible gases which can be present during the measurement (interferent gases). This characteristic is very important in several applications. Breath analysis is one of these. In fact, human breath is a very complex mixture of different gases and volatile organic compounds which can be present in a range of concentrations from few parts-per-billion (ppb) to hundreds part-per-million (ppm). Each one of them can be interferent in such a type of measurement. A sensor intended to be employed in breath analysis must, therefore, features an excellent selectivity in order to reduce the probability to obtain false-positive diagnosis.

In order to assess the selectivity of the proposed sensors, sensitivity towards several possible interferent gases was assessed with the same measurement setup employed in the case of acetone, testing some of these gases at different concentrations. Tested gases, such as ammonia, carbon monoxide and dioxide, hydrogen, oxygen, methane, ethanol and nitrogen dioxide, were added to the carrier gas mixture (O_2: 20% and N_2: 80%) so as to have concentration of several ppm. The results of such testes are presented in figure 5.21 in terms of relative response towards the tested gas normalized by the tested gas concentration, so as to provide a concentration-independent quality factor of the sensor selectivity. It is evident how sensor #4 is characterized by a very excellent selectivity towards all the tested gases with normalized responses typically close to the detection limit (such as in the case of carbon dioxide, methane and oxygen), or in the worst cases (such as carbon monoxide, hydrogen and ammonia) always lower than the 5% of the acetone response. Selectivity of sensor #2 is still excellent, even thought a significant response was recorded with some of the tested gases, such as hydrogen and ethanol with responses being respectively about the 13% (10 ppm) and the 27% (5 ppm) of the acetone response.

In conclusion, the tests carried out put in evidence the good sensitivity to acetone of

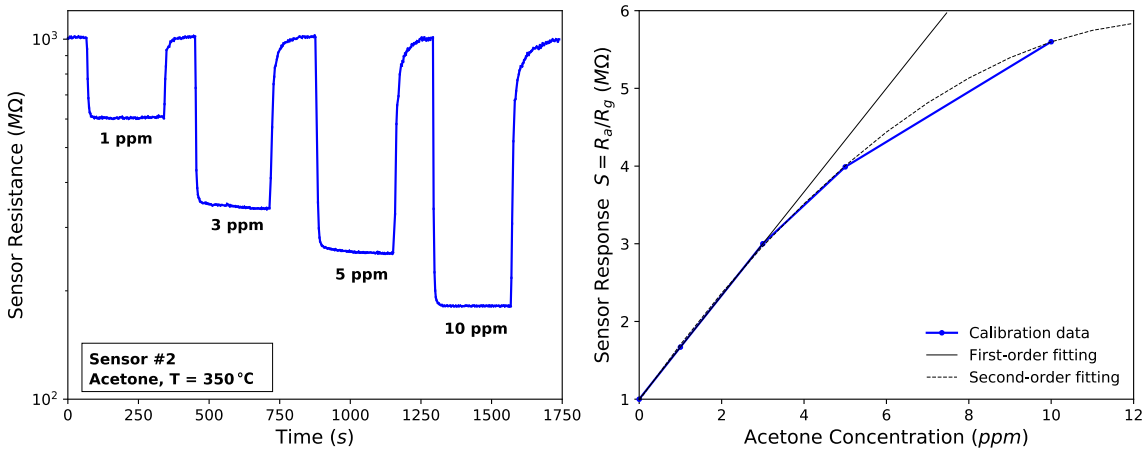

Figure 5.19: Response of the sensor #2 to acetone in the range of 1 ppm to 10 ppm at a working temperature of 350 °C.

both the prototypes. In particular, sensor #2 is characterized by a very high sensitivity, but with a low saturation limit of about 12 ppm. In contrast, sensor #4 exhibits a lower sensitivity but with a much higher saturation limit. Thus, both sensors can be successfully applied in acetone monitoring, with sensor #2 preferred in application requiring high sensitivity at a low concentration, and sensor #4 being more suitable for applications characterized by much higher concentrations. Both sensors, especially sensor #4, are characterized by a very good selectivity towards several common interferent gases, with the exception of ethanol, whose response is not negligible. Anyhow, both sensors are suitable for being employed in the breath analysis of acetone. In fact, typical acetone concentration in human breath is in the order of few ppm, therefore no one of the sensors is expected to saturate or to be under the detection limit. Moreover, ethanol is present in the human breath only after a significant intake of alcohol. Thus the possible interference of ethanol can be easily deleted by avoiding any assumption of alcohol few hours before the acetone test.

5.3.8 Sensor stability

Subsequently, all the described characterizations and tests, the stability of the two sensors was assessed. Stability can be considered as the capability of the sensor to maintain its performance for a long time, after repeated measurements, and even after the exposure to aggressive gases which could modify sensing surface and sensing characteristics.

Thus, the sensitivity test to acetone of both sensors was repeated so as to put in evidence any possible modification of the sensing performance. With this aim, the sensor response to several acetone pulses with a concentration of 5 ppm was evaluated. As an

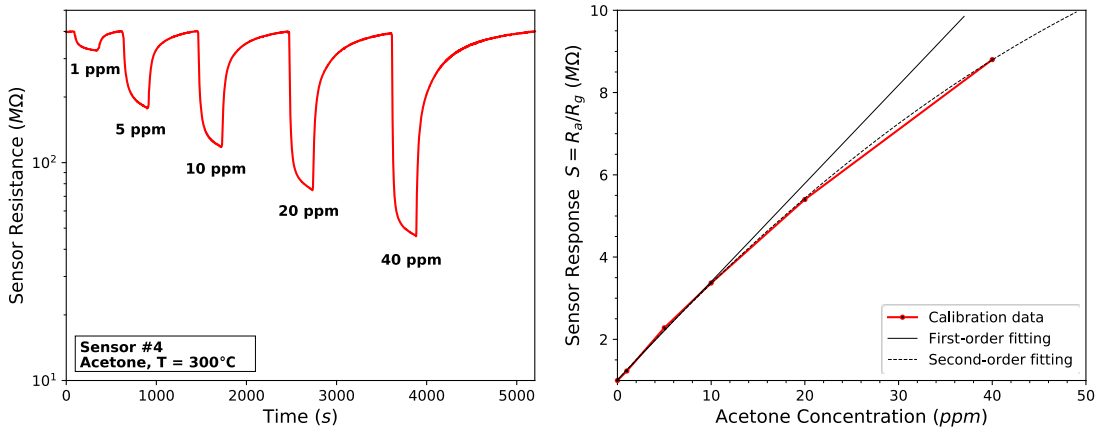

Figure 5.20: Response of the sensor #4 to acetone in the range of 1 ppm to 40 ppm at a working temperature of 300 °C.

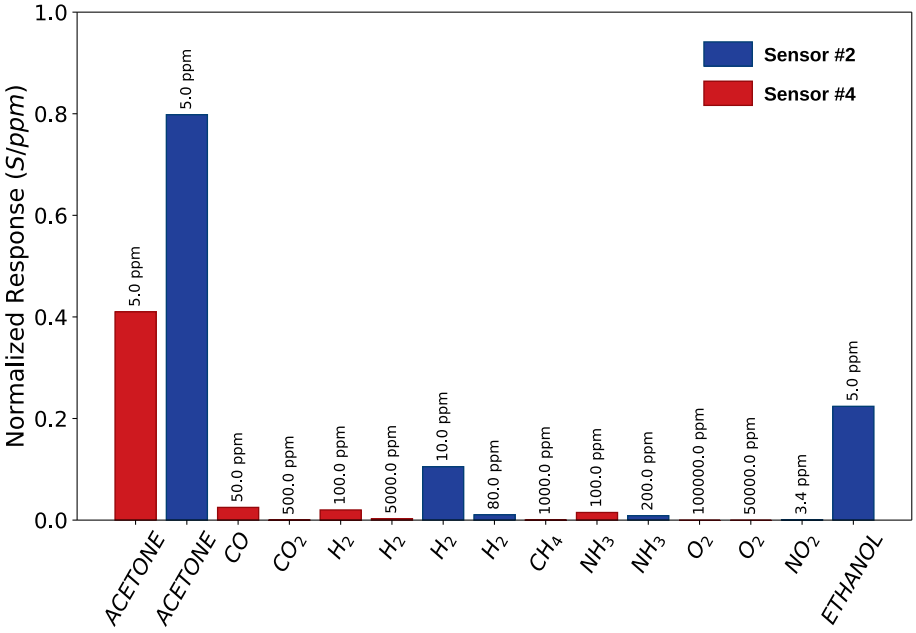

Figure 5.21: Normalized responses of the sensors #2 and #4 to several possible interferent gases, together with the tested concentration.

example, figure 5.22 shows five repeated acetone pulses for sensor #2 (graph on the left) and sensor #4 (graph on the right).

It is clearly visible how there is no significant offset of the reference resistance R_a

Table 5.6: Statistical parameters extracted by the stability test performed on both sensors.

	Sensor #2			**Sensor #4**		
	R_a	R_g	S	R_a	R_g	S
μ (MΩ)	944.6	255.8	3.66	390.4	182.7	2.13
σ (MΩ)	14	1.1	0.07	1.1	2.18	0.03
ε	1.5%	0.4%	1.9%	0.3%	1.2%	1.4%

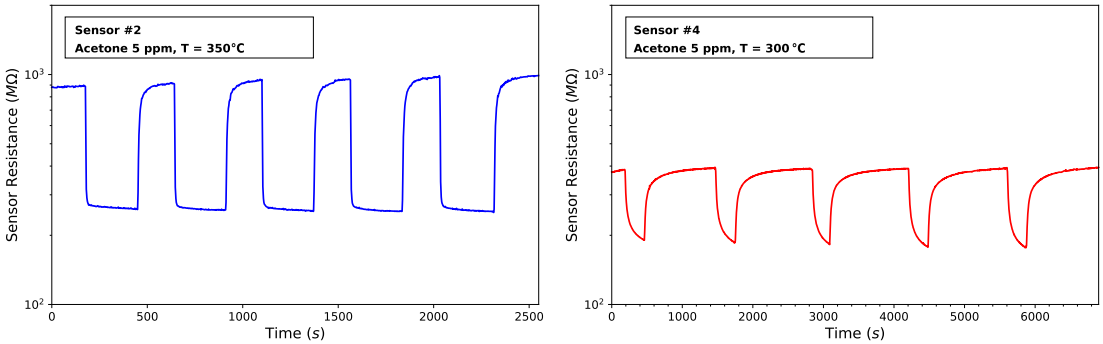

Figure 5.22: Responses to repeated acetone pulses at 5 ppm for sensors #2 (left) and #4 (right).

after repeated measurements, and how the sensor response features a good repeatability without significant drift and hysteresis. Table 5.6 reports the statistical data derived from the stability measurements on both the sensors. In particular, the relative error on repeated sensitivity measurements is quite low and it is in the order of 1.9% and 1.4% , respectively, for sensor #2 and #4.

It is also interesting to note how the relative response changed because of the repeated measurements with the interferent gases performed during the selectivity testes. Sensitivity of sensor #2 changed from 3.98 to 3.66 exhibiting a variation of about 8%. Instead, the sensitivity of sensor #4 changed from 2.28 to 2.13 with a variation of about 6.5%. Even thought this variation is surely not negligible, however, it should be considered that several measurements were performed in presence of highly aggressive gases (such as N_2O), even at very high concentrations. Thus, the obtained results confirm good stability and repeatability of the proposed sensors.

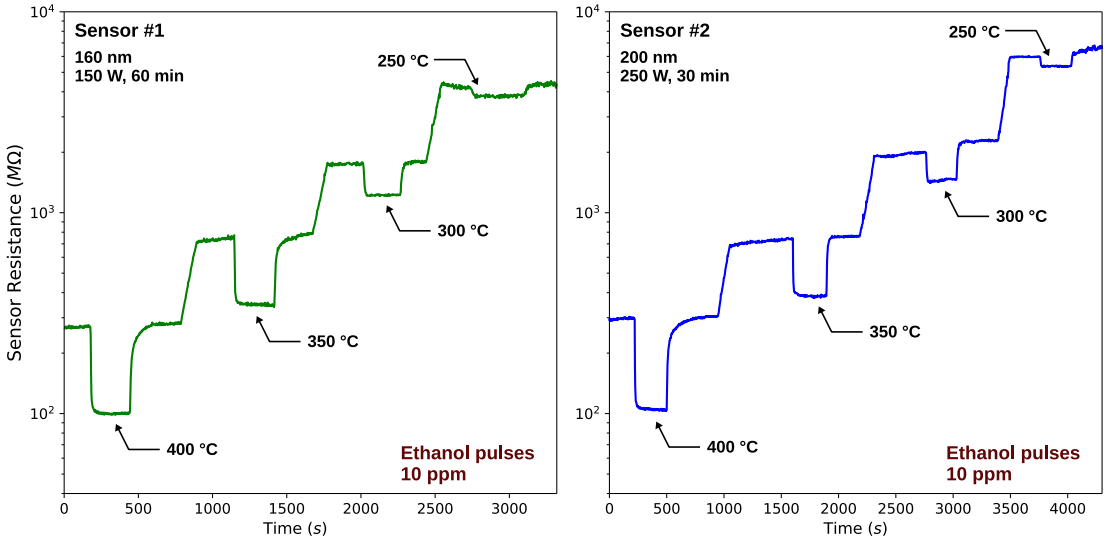

Figure 5.23: Response of sensors #1 and #2 towards 10 ppm of ethanol in the temperature range of 250 °C to 400 °C.

5.3.9 Sensor sensitivity towards ethanol

The selectivity tests put in evidence a noteworthy response of sensor #2 to ethanol at a concentration of 5 ppm. Thus, further characterizations were carried out to better assess the performance of this prototype towards ethanol and to investigate the possibility to employ such a sensor for ethanol as well.

Firstly, the sensitivity dependence from temperature has been evaluated for both the sensors #1 and #2 in a temperature range of 250 °C to 400 °C by employing the same setup described in section 5.3.5, but employing an ethanol concentration of 10 ppm. Results are shown in figure 5.23. It is possible to observe the response of the sensors at four different temperatures. Both sensors have a behavior similar to the one obtained with the acetone: sensitivity increases with the increasing of working temperature.

By employing these data, the relative response of the sensors was evaluated and it is shown in figure 5.24. It can be observed how sensitivity goes from about 1.1 at 250 °C to about 2.7 at 400 °C with only a minimal differences between the two sensors. Thus, it seems that the optimal working temperature is higher than 400 °C for both sensors. Unfortunately, the actual temperature range of the measurement setup goes from room temperature to maximum 400 °C and, thus, it is not possible, at the moment, to better investigate this characteristic.

Subsequently, the response times were assessed by measuring, for both the sensors, the response to a step of ethanol from 0 ppm to 10 ppm and back to 0 ppm. Figure 5.25 shows the responses to the positive step on the left, and of the negative one on the right.

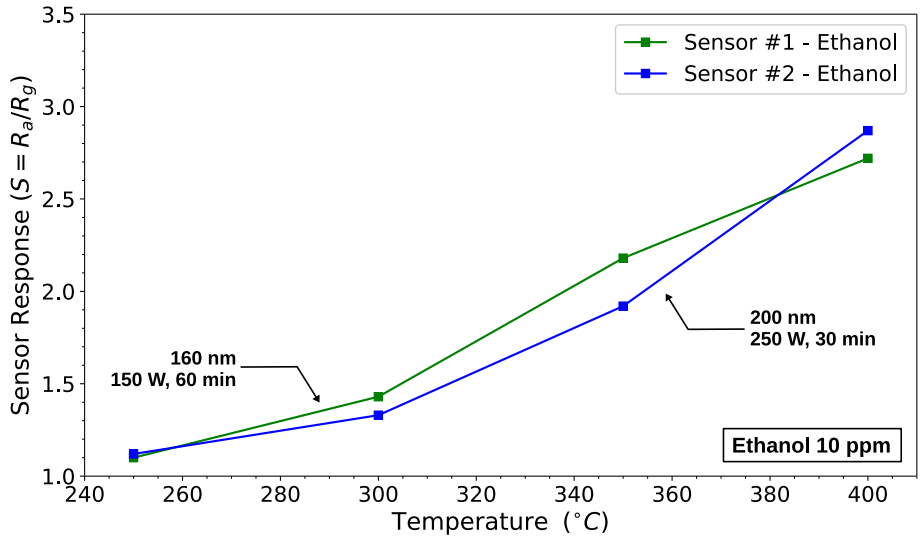

Figure 5.24: Temperature dependence of the sensors responses towards 10 ppm of ethanol in the temperature range of 250 °C to 400 °C.

In the same graphs there are also included the step responses (in dashed lines) of sensor #2 to acetone pulses at 5 ppm as a way to compare the response times towards acetone and ethanol. It is possible to see how response times are comparable between the two sensors and between ethanol and acetone. Figure 5.26 shows the response and the recovery times with the aim of highlighting the dependence of the response times from temperature. As before, dashed lines refer to the acetone test performed on sensor #2. Response times to ethanol for both sensors are comparable to times obtained with acetone, and all are in the order of few seconds. Some difference between sensor #1 and #2 in presence of ethanol can be observed only at temperatures below 300 °C: sensor #1 is slower than #2 of about 20 s at a temperature of 250 °C.

Instead, a very different behavior of recovery times was recorded between ethanol and acetone. It can be observed how recovery time of sensor #2 in presence of acetone slightly decreases with the increasing of the temperature, as described and explained in section 5.3.6. Instead, recovery time of the same sensor in presence of ethanol exhibits a completely different trend: it starts from about 60 s at 250 °C, then decreases with the temperature down to about 25 s (between 250 °C and 350 °C) but after this, suddenly, increases with the temperature, reaching about 73 s at 400 °C. A similar trend has been found also for sensor #1 exposed to ethanol, but it seems shifted at lower temperatures by about 50 °C. Such behavior cannot be easily explained and it is not typical found in such a kind of sensors. Further investigations are required in order to better investigate such an effect.

As conclusion, although more investigations are required, the preliminary characterizations already performed revealed the suitability of the proposed Nb_2O_5 prototypes

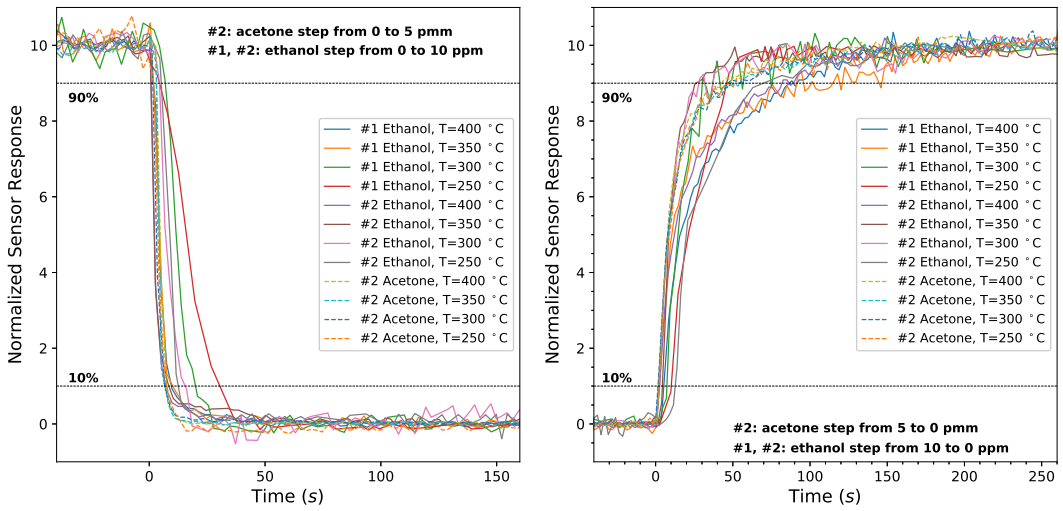

Figure 5.25: Response to 10 ppm steps of ethanol for prototypes #2 and #4 at four different temperatures in the range of 250 °C to 400 °C, and comparison with the response of sensor #2 to acetone steps at 5 ppm.

to be employed as ethanol sensors.

5.4 Conclusions and future work

Chapter 5 describes the research activities carried out during the development and the characterization of high-sensitive acetone sensors based on Nb_2O_5 thin films. Several prototypes were deposited on small alumina substrates and individually characterized in terms of film structure and composition. All the deposited prototypes revealed a sensing film composed mainly by Nb_2O_5 with thickness ranging between 100 nm to 1 µm. Thin films, deposited with a low deposition rates, are characterized by a compact non-porous structure. In contract, thick film deposited with a higher power, exhibit a porous structure composed by tiny vertical nano-rods. The sensing performance of the prototypes were assessed by employing a dedicated measurement setup. Preliminary tests were carried out to characterize the heater of each deposited prototype in order to increase accuracy of the sensor working temperature. The subsequent tests revealed an optimal working temperature in the range of 300 °C to 350 °C, according to the specific prototype. The achieved sensitivities allow one to detect acetone down to the ppm level and, therefore, both sensors are suitable for the breath analysis of acetone for the assessment of diabetes. In particular, sensor #2 revealed very high sensitivity in the sub-ppm level, but with a saturation point of about 12 ppm. Instead, sensor #4 features a much higher saturation point, but with a lower sensitivity. Moreover, sensor

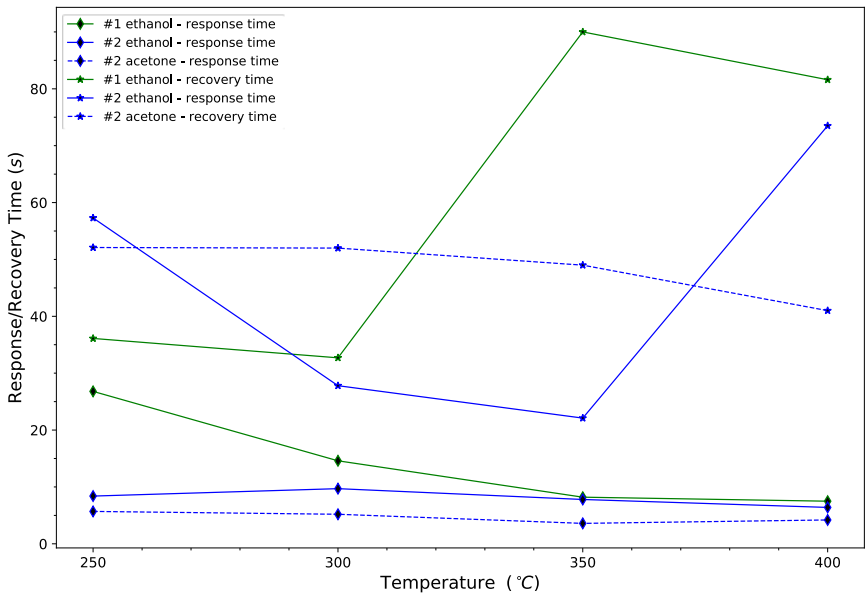

Figure 5.26: Sensitivity dependence from temperature of sensors #1 and #2, towards ethanol (10 ppm), and of sensor #2 towards acetone (5 ppm).

#2 revealed a very fast response with a typical time of about 5 s, almost independent by the working temperature. This is very useful in the breath analysis field: having a fast response allows one to reduce the breath sampling time with the consequent reduction of patient effort and stress during the test. Both sensors are characterized by an excellent selectivity towards acetone, with all the tested interferent gases having negligible responses. The only detected interferent gas was ethanol for sensor #2. Anyway, this does not represent a severe issue for the employment of the sensor in the acetone monitoring. Ethanol in exhaled breath is exclusively due to the intake of alcohol. Avoiding alcohol assumption before the acetone test can easily revolve such an issue. All the tested prototypes demonstrated very good stability with negligible variation of their response after several repeated test with acetone and other different gases.

Further measurements have been planned in order to better characterize the sensing performance of sensor #2 towards ethanol with the aim of developing an ethanol sensor, as well. Furthermore, new deposition parameters will be tested in order to improve the sensing performance. Mixed depositions of Nb_2O_5 together with small quantities of impurities, such as platinum and gold, will be carried out and the new prototypes will be characterized and compared with those already described in this thesis. Eventually, a thermal post-treatment (annealing) will be carried out in inert atmosphere at temperatures between 400 °C and 700 °C with the aim of assessing if such a treatment can be beneficial in terms of sensitivity, selectivity and stability of the sensors.

Chapter 6

Conclusions

Environmental monitoring, especially in terms of pollution, and health care are topics of primary importance in order to improve health status and life conditions of human beings. In this framework, the development of cost-effective and high-performing sensors in extremely important. The research work discussed in this thesis deals with such topics and in particular with the development and characterization of a novel approach for monitoring the atmospheric particulate matter, and the realization of high-performing gas sensors for breath analysis.

As discussed in chapter 2, a widespread monitoring of the particulate is mandatory, especially in high polluted areas featuring high population density, such as big cities and industrial areas. Such a monitoring can significantly help to safeguard people health and provide real-time alarms when unsafe conditions are reached. Moreover, a capillary monitoring can provide useful information for better understanding the processes involved in the production, transportation and deposition of atmospheric particulate matter.

Instruments typically employed in this field are often bulky and expensive, and this strongly limits their employment in such a kind of applications. Furthermore, such instruments usually provide only a partial characterization of the aerosol focusing the measurement only on specific properties of the particulate.

A new measurement approach is, therefore, proposed in chapter 3. Such an approach is based on the detection of the single particles captured on standard glass fibre filter by means of a cheap digital camera connected to a RaspberryPI ZeroW board. A dedicated image processing software is able to identify each particle and estimate its equivalent size.

Three different working prototypes were realized and tested in order to assess the feasibility of the proposed approach and the achieved performance. The three prototypes share the same optical camera system and differ only for the adopted filter management. The first prototype employs a manual filter management where user intervention is required to replace the filter. The second prototype, instead, features a

semi-automatic filter management which allows one to perform up to seven sequential measurements automatically. Eventually, the third prototype employs a completely automated filter management which is able to continuously perform measurements for months without any maintenance.

The characterizations carried out on the prototypes demonstrated the feasibility of the proposed method highlighting quite promising results. In particular, the system is able to detect particles down to about 3 μm, limited by the filter mesh size and the optical system resolution. Measurements of the total particulate amount in $\mu g/m^3$ and the particulate size distribution are provided in real-time. The long-range LoRa connectivity permits an easy arrangement of a wide-range wireless sensor networks for a capillary monitoring of atmospheric particulate matter. Furthermore, tests performed at different backlighting wavelengths put in evidence the possibility to implement a simple spectral analysis of the captured particles which might be able to provide additional information about the aerosol type and composition. Eventually, the comparison carried out towards a commercial laser-scattering station revealed a quite good agreement of the two instruments with comparable results.

Even thought additional characterization are surely required to fully assess the system performance, it seems that such proposed method can be a valid low-cost alternative to the commonly employed equipment in several different application fields.

The other main topic is, instead, the breath analysis. This diagnostic method, briefly discussed in chapter 4, is nowadays becoming a valid alternative to conventional approaches such as blood and urine tests. Its principal advantages are: non-invasiveness, fast response and low management costs. However, such method requires the detection of specific biomarkers in the exhaled breath and, usually, such biomarkers features concentrations of few ppm or ppb. This turns out in a increasing demand of high-sensitive and selective sensors.

Therefore, several conductometric gas sensors based on metal oxides were realized with the aim of developing high-performing sensors suitable for such a field. Such sensors, discussed in chapter 5, revealed excellent sensing performance towards acetone, a recognized biomarker of diabetes. Several sensor prototypes were realized by depositing thin films of Nb_2O_5 on small alumina substrates. The deposition was carried out by reactive plasma sputtering in a capacitively-coupled parallel-plate reactor by testing several different combination of deposition parameters.

Several characterization were carried out on the different prototypes in order to assess their physical and chemical properties, and their sensing performance. In particular, sensitivity, selectivity, stability and response times were investigated with dedicated tests and two of them (sensor #2 and #4) demonstrated excellent performance.

Sensor #2, characterized by a thin sensing film, exhibits a high sensitivity and it is suitable for detecting acetone at the sub-ppm level. Furthermore, such sensor features excellent selectivity and an extremely fast response time of about 4 s. Sensor #4, instead, has a much thicker sensing film and features a lower sensitivity. Anyhow, such sensor, thanks to its higher saturation limit, is able to measure acetone concentrations

in excess of 50 ppm. This makes it more suitable for application where a high acetone concentration is expected. Sensor #4 is characterized by a still excellent selectivity but a quite slower response. The only interferent gas detected in the selectivity tests was ethanol. Fortunately, ethanol is present in the exhaled breath only after the intake of alcohol. Therefore, limiting the assumption of alcohol before the acetone test is enough in order to avoid such an issue. Eventually, stability tests demonstrated the absence of significant offset and hysteresis in the sensor response also after repeated exposures to several aggressive gases. Both sensors are suitable for being employed in the breath analysis of diabetes, even thought sensor #2 can significantly reduce the measurement time due to its extremely fast response.

In conclusion, an innovative detection approach for the monitoring of atmospheric particulate matter was proposed and validated with experimental tests. Such method demonstrated its feasibility for being employed in a widespread monitoring of the pollution thanks to its real-time response and low cost. Sensor for monitoring of acetone in exhaled breath were realized and fully characterized. They demonstrated excellent sensing performance which make them suitable for the implementation of portable breath analyzers thanks to their small size and low power consumption. Further investigations will be carried out on both the particulate monitoring system and the sensors in order to improve their performance with the ultimate aim to develop effective devices to be employed in the environmental monitoring and breath analysis fields.

Bibliography

[1] L. Lombardo, M. Parvis, E. Angelini, N. Donato, S. Grassini, "An Optical Sensing System for Atmospheric Particulate Matter", Lecture Notes in Electrical Engineering, Vol. 539, 2019, 10.1007/978-3-030-04324-7_36.

[2] L. Lombardo, M. Parvis, E. Angelini, S. Grassini, "An Optical Sampling System for Distributed Atmospheric Particulate Matter", IEEE Transactions on Instrumentation and Measurement, Vol. 68, Is. 7, 2019, Pages 2396-2403, 10.1109/TIM.2019.2890885.

[3] L. Lombardo, M. Parvis, E. Angelini, S. Grassini, "Optical solution for particulate distribution estimation", 2018 IEEE International Instrumentation and Measurement Technology Conference (I2MTC), 2018, Pages 1-6, 10.1109/I2MTC.2018.8409749.

[4] L. Lombardo, M. Parvis, F. Vitiello, E. Angelini, S. Grassini, "A Sensor Network for Particulate Distribution Estimation", 2018 IEEE International Symposium on Medical Measurements and Applications (MeMeA), 2018, Pages 1-6, 10.1109/MeMeA.2018.8438701.

[5] L. Lombardo, N. Donato, S. Grassini, A. Gullino, K. Moulaee, G. Neri, M. Parvis, "Nb_2O_5 thin film-based conductometric sensor for acetone monitoring", 2019 IEEE International Symposium on Medical Measurements and Applications (MeMeA), 2019, Pages 1-5, 10.1109/MeMeA.2019.8802126.

[6] "Particulate Matter (PM) Pollution", Environmental Protection Agency (EPA), available at: https://www.epa.gov/pm-pollution, last checked on August, 17 2019.

[7] M. C. Jacobson, H. C. Hansson, K. J. Noone, R. J. Charlson, "Organic atmospheric aerosols: Review and state of the science", Reviews of Geophysics, Vol. 38, Is. 2, 2000, Pages 267-294, 10.1029/1998RG000045.

[8] A. Petzold, J. A. Ogren, M. Fiebig, P. Laj, S. M. Li, U. Baltensperger, T. Holzer-Popp, S. Kinne, G. Pappalardo, N. Sugimoto, C. Wehrli, A. Wiedensohler, X. Y. Zhang, "Recommendations for reporting "black carbon" measurements", Atmospheric Chemistry and Physics, Vol. 13, Is. 16, 2013, Pages 8365-8379, 10.5194/acp-13-8365-2013.

[9] H. Moosmüller, R. K. Chakrabarty, W. P. Arnott, "Aerosol light absorption and its measurement: A review", Journal of Quantitative Spectroscopy and Radiative Transfer, Vol. 110, Is. 11, 2009, Pages 844-878, 10.1016/j.jqsrt.2009.02.035.

[10] S. Solomon, Q. D. Manning, K. M. Averyt, M. Marquis, "Climate change 2007 – The physical science basis: Working group I, contribution to the fourth assessment report of the IPCC", Vol. 4, 2007, Cambridge University Press.

[11] P. Stier, J. H. Seinfeld, S. Kinne, O. Boucher, "Aerosol absorption and radiative forcing", Atmospheric Chemistry and Physics, Vol. 7, Is. 197, 2007, Pages 5237-5261, 10.5194/acp-7-5237-2007.

[12] P. Chylek, J. Wong, "Effect of absorbing aerosols on global radiation budget", Geophysical Research Letters, Vol. 22, Is. 8, 1995, Pages 929-931, 10.1029/95GL00800.

[13] S. K. Satheesh, K. K. Moorthy, "Radiative effects of natural aerosols: A review", Atmospheric Environment, Vol. 39, Is. 11, 2005, Pages 2089-2110, 10.1016/j.atmosenv.2004.12.029.

[14] C. I. Davidson , R. F. Phalen, P. A. Solomon, "Airborne Particulate Matter and Human Health: A Review", Aerosol Science and Technology, Vol. 39, 2005, Pages 737–749, 10.1080/02786820500191348.

[15] S. G. Warren, "Optical properties of snow", Reviews of Geophysics, Vol. 20, Is. 1, 1982, Pages 67-89, 10.1029/RG020i001p00067.

[16] S. G. Warren, "Optical properties of ice and snow", Philosophical Transactions of the Royal Society A: Mathematical, Physical and Engineering Sciences, Is. 377, 2019.

[17] J. Hansen, L. Nazarenko, "Soot climate forcing via snow and ice albedos", Proceedings of the National Academy of Sciences, Vol. 101, Is. 2, 2004, Pages 423-428, 10.1073/pnas.2237157100.

[18] M. G. Flanner, C. S. Zender, J. T. Randerson, P. J. Rasch, "Present-day climate forcing and response from black carbon in snow", Journal of Geophysical Research: Atmospheres, Vol. 112, Is. D11, 2007, 10.1029/2006JD008003.

[19] S. J. Déry, R. D. Brown, "Recent Northern Hemisphere snow cover extent trends and implications for the snow-albedo feedback", Geophysical Research Letters, Vol. 34, Is. 22, 2007, 10.1029/2007GL031474.

[20] D. W. Dockery, J. Cunningham, A. I. Damokosh, L. M. Neas, J. D. Spengler, P. Koutrakis, J. H. Ware, M. Raizenne, F. E. Speizer, "Health effects of acid aerosols on North American children: respiratory symptoms", Environmental Health Perspectives, Vol. 104, Is. 5, 1996, 10.1289/ehp.96104500.

[21] J. S. Lighty, J. M. Veranth, A. F. Sarofim, "Combustion Aerosols: Factors Governing Their Size and Composition and Implications to Human Health", Journal of the Air & Waste Management Association, Vol. 50, Is. 9, 2000, Pages 1565-1618, 10.1080/10473289.2000.10464197.

[22] D. W. Dockery, C. A. Pope, "Acute Respiratory Effects of Particulate Air Pollution", Annual Review of Public Health, Vol. 15, Is. 1, 1994, Pages 107-132, 10.1146/annurev.pu.15.050194.000543.

[23] C. A. Pope III, R. T. Burnett, M. J. Thun, E. E. Calle, D. Krewski, K. Ito, G. D. Thurston, "Lung Cancer, Cardiopulmonary Mortality, and Long-term Exposure to Fine Particulate Air Pollution", Journal of American Medical Association, Vol.

287, Is. 9, 2002, Pages 1132-1141, 10.1001/jama.287.9.1132.

[24] H. Schulz, V. Harder, A. Ibald-Mulli, A. Khandoga, W. Koenig, F. Krombach, R. Radykewicz, A. Stampfl, B. Thorand, A. Peters, "Cardiovascular Effects of Fine and Ultrafine Particles", Journal of Aerosol Medicine, Vol. 18, Is. 1, 2005, Pages 1-22, 10.1089/jam.2005.18.1.

[25] World Health Organization, "Health Effects of Particulate Matter", 2013, available at http://www.euro.who.int/data/assets/pdf_file/0006/189051/ Health-effects-of-particulate-matter-final-Eng.pdf, last checked on August, 21 2019.

[26] World Health Organization, "Quantifying environmental health impacts", available at http://www.who.int/quantifying_ehimpacts/news_events/en/, last checked on August 22, 2019.

[27] S. S. Amaral, J. A. de Carvalho Jr, M. A. Martins Costa, C. Pinheiro, "An Overview of Particulate Matter Measurement Instruments", Atmosphere, Vol. 6, 2015, Pages 1327-1345, 10.3390/atmos6091327.

[28] US Environmental Protection Agency, List of designed reference and equivalent methods, 2001.

[29] DM 05 May 2015, Attachment 1, "Metodo di campionamento e di analisi per la misura delle concentrazioni di massa totale e per speciazione chimica del materiale particolato PM10 e PM 2.5", Gazzetta Ufficiale della Repubblica Italiana, Is. 128, June 05 2015.

[30] L. Lombardo, M. Parvis, E. Angelini, S. Grassini, "An Optical Sampling System for Distributed Atmospheric Particulate Matter", IEEE Transactions on Instrumentation and Measurement, Vol. 68, Is. 7, 2019, Pages 2396-2403, 10.1109/TIM.2019.2890885.

[31] L. Lombardo, M. Parvis, F. Vitiello, E. Angelini, S. Grassini, "A Sensor Network for Particulate Distribution Estimation", MeMeA 2018, 2018 IEEE International Symposium on Medical Measurements and Applications, 2018, 10.1109/MeMeA.2018.8438701.

[32] The OpenCV Library, available at "https://opencv.org/", last checked on October, 25 2019.

[33] X. Liu, S. Cheng, H. Liu, S. Hu, D. Zhang, H. Ning, "A Survey on Gas Sensing Technology", Sensors, Vol. 12, Is. 7, 2005, Pages 9635-9665, 10.3390/s120709635.

[34] B. Timmer, W. Olthuis, A. van den Berg, "Ammonia sensors and their applications—a review", Sensors and Actuators B: Chemical, Vol. 107, Is. 2, 2005, Pages 666-677, 10.1016/j.snb.2004.11.054.

[35] S. Corbellini, M. Parvis, S. Grassini, L. Benussi, S. Bianco, S. Colafranceschi, D. Piccolo, "Modified POF Sensor for Gaseous Hydrogen Fluoride Monitoring in the Presence of Ionizing Radiations", IEEE Transactions on Instrumentation and Measurement, Vol. 61, Is. 5, 2012, Pages 1201-1208, 10.1109/TIM.2011.2175821.

[36] O. Lawal, W. M. Ahmed, T. M. E. Nijsen, R. Goodacre, S. J. Fowler, "Exhaled breath analysis: a review for 'breath-taking' methods for off-line analysis", Metabolomics, Vol. 13, Is. 110, 2017, 10.1007/s11306-017-1241-8.

[37] K. H. Kim, S. A. Jahan, E. Kabir, "A review of breath analysis for diagnosis of human health", Trends in Analytical Chemistry, Vol. 33, 2012, Pages 1-8, 10.1016/j.trac.2011.09.013.

[38] N. Queralto, A. N. Berliner, B. Goldsmith, R. Martino, P. Rhodes, S. H. Lim, "Detecting cancer by breath volatile organic compound analysis: a review of array-based sensors", Journal of Breath Research, Vol. 8, 2014, 10.1088/1752-7155/8/2/027112.

[39] T. H. Risby, S. F. Solga, "Current status of clinical breath analysis", Applied Physics B, Vol. 85, 2006, Pages 421-426, 10.1007/s00340-006-2280-4.

[40] C. Di Natale, R. Paolesse, E. Martinelli, R. Capuano, "Solid-state gas sensors for breath analysis: A review", Analytica Chimica Acta, Vol. 824, 2014, Pages 1-17, 10.1016/j.aca.2014.03.014.

[41] J. R. Stetter, J. Li, "Amperometric Gas Sensors: A Review", Chemical Reviews, Vol. 108, Is. 2, 2008, Pages 352-366, 10.1021/cr0681039.

[42] G. Eranna, B. C. Joshi, D. P. Runthala, R. P. Gupta, "Oxide Materials for Development of Integrated Gas Sensors–A Comprehensive Review", Critical Reviews in Solid State and Materials Sciences, Vol. 29, Is. 3-4, 2004, Pages 111-188, 10.1080/10408430490888977.

[43] A. Dey, "Semiconductor metal oxide gas sensors: A review", Materials Science and Engineering: B, Vol. 229, 2018, Pages 206-217, 10.1016/j.mseb.2017.12.036.

[44] S. Das, V. Jayaraman, "SnO_2: A comprehensive review on structures and gas sensors", Progress in Materials Science, Vol. 66, 2014, Pages 112-255, 10.1016/j.pmatsci.2014.06.003.

[45] R. M. Langdon, "Resonator sensors–a review", Journal of Physics E: Scientific Instruments, Vol. 18, Is. 2, 1985, Pages 103-115, 10.1088/0022-3735/18/2/002.

[46] S. Grassini, M. Ishtaiwi, M. Parvis, L. Benussi, S. Bianco, S. Colafranceschi, D. Piccolo, "Gas monitoring in RPC by means of non-invasive plasma coated POF sensors", Journal of Instrumentation, Vol. 7, Is. 12, 2012, Pages 12006-12006, 10.1088/1748-0221/7/12/p12006.

[47] E. Angelini, S. Grassini, D. Mombello, A. Neri, M. Parvis, G. Perrone, "Plasma modified POF sensors for in situ environmental monitoring of museum indoor environments", Applied Physics A, Vol. 100, Is. 3, 2010, Pages 975-980, 10.1007/s00339-010-5691-3.

[48] K. Arshak, E. Moore, G. Lyons, J. Harris, S. Clifford, "A review of gas sensors employed in electronic nose applications", Sensor Review, Vol. 24; Is. 2, 2004, Pages 181-198, 10.1108/02602280410525977.

[49] P. T. Moseley, "Solid state gas sensors", Measurement Science and Technology, Vol. 8, Is. 3, 1997, Pages 223-237, 10.1088/0957-0233/8/3/003.

[50] N. Barsan, U. Weimar, "Conduction Model of Metal Oxide Gas Sensors", Journal of Electroceramics, Vol. 7, Is. 3, 2001, Pages 143-167, 10.1023/A:1014405811371.

[51] N. Barsan, U. Weimar, "Understanding the fundamental principles of metal oxide based gas sensors: the example of CO sensing with SnO_2 sensors in the presence

of humidity", Vol. 15, Is. 20, 2003, Pages R813-R839, 10.1088/0953-8984/15/20/201.

[52] N. Barsan, C. Simion, T. Heine, S. Pokhrel, U. Weimar, "Modeling of sensing and transduction for p-type semiconducting metal oxide based gas sensors", Journal of Electroceramics, Vol. 25, Is. 1, 2010, Pages 11-19, 10.1007/s10832-009-9583-x.

[53] C. Wang, L. Yin, L. Zhang, D. Xiang, R. Gao, "Metal Oxide Gas Sensors: Sensitivity and Influencing Factors", Sensors, Vol. 10, Is. 3, 2010, Pages 2088-2106, 10.3390/s100302088.

[54] M. A. Andio, P. Browning, P. A. Morris, S. A. Akbar, "Comparison of gas sensor performance of SnO_2 nano-structures on micro hot-plate platforms", Sensors and Actuators B: Chemical, Vol. 165, 2012, Pages 13-18, 10.1016/j.snb.2011.12.045.

[55] T. Hemalatha, S. Akilandeswari, T. Krishnakumar, S. G. Leonardi, G. Neri, N. Donato, "Comparison of Electrical and Sensing Properties of Pure, Sn- and Zn-Doped CuO Gas Sensors", IEEE Transactions on Instrumentation and Measurement, Vol. 68, Is. 3, 2019, Pages 903-912.

[56] K. J. Choi, H. W. Jang, "One-Dimensional Oxide Nanostructures as Gas-Sensing Materials: Review and Issues", Sensors, Vol. 10, Is. 4, 2010, Pages 4083-4099, 10.3390/s100404083.

[57] Y. Li, Y. Xiaofeng, Y. Qunbao, "Fabrication of TiO_2 Nanotube Thin Films and Their Gas Sensing Properties", Journal of Sensors, 2009, 10.1155/2009/402174.

[58] A. Vergara, E. Llobet, J. Brezmes, P. Ivanov, C. Cané, I. Gràcia, X. Vilanova, X. Correig, "Quantitative gas mixture analysis using temperature-modulated micro-hotplate gas sensors: Selection and validation of the optimal modulating frequencies", Sensors and Actuators B: Chemical, Vol. 123, Is. 2, 2007, Pages 1002-1016, 10.1016/j.snb.2006.11.010.

[59] J. Lee, S. Mubeen, C. M. Hangarter, A. Mulchandani, W. Chen, N. V. Myung, "Selective and Rapid Room Temperature Detection of H_2S Using Gold Nanoparticle Chain Arrays", Electroanalysis, Vol. 23, Is. 11, Pages 2623-2628, 10.1002/elan.201100295.

[60] J. Zhang, L. Xianghong, G. Neri, N. Pinna, "Nanostructured Materials for Room-Temperature Gas Sensors", Advanced Materials, Vol. 28, 2016, Pages 795-831, 10.1002/adma.201503825.

[61] D. Rosenfeld, P. E. Schmid, S. Széles, F. Lévy, V. Demarne, A. Grisel, "Electrical transport properties of thin-film metal-oxide-metal Nb_2O_5 oxygen sensors", Sensors and Actuators B: Chemical, Vol. 37, Is. 1–2, 1996, Pages 83-89, 10.1016/S0925-4005(96)01991-0.

[62] L. Chambon, A. Pauly, J. P. Germain, C. Maleysson, V. Demarne, A. Grisel, "A model for the responses of Nb_2O_5 sensors to CO and NH_3 gases", Sensors and Actuators B: Chemical, Vol. 43, Is. 1–3, 1997, Pages 60-64, 10.1016/S0925-4005(97)00136-6.

[63] Z. Wang, Y. Hu, W. Wang, X. Zhang, B. Wang, H. Tian, Y. Wang, J. Guan, H. Gu,

"Fast and highly-sensitive hydrogen sensing of Nb_2O_5 nanowires at room temperature", International Journal of Hydrogen Energy, Vol. 37, 2012, 10.1016/j.ijhydene.2011.12.004.

[64] L. Lombardo, N. Donato, S. Grassini, A. Gullino, K. Moulaee, G. Neri, M. Parvis, "Nb_2O_5 thin film-based conductometric sensor for acetone monitoring", IEEE International Symposium on Medical Measurements and Applications (MeMeA), 2019.

[65] Z. Wang, C. Wang, "Is breath acetone a biomarker of diabetes? A historical review on breath acetone measurements", Journal of Breath Research, Vol. 7, Is. 3, 2013, 10.1088/1752-7155/7/3/037109.

[66] C. Wang, A. Mbi, M. Shepherd, C. Jiang, "A Study on Breath Acetone in Diabetic Patients Using a Cavity Ring-down Breath Analyzer: Exploring Correlations of Breath Acetone With Blood Glucose and Glycohemoglobin A1C", Sensors Journal, IEEE, Vol. 10, 2010, Pages 54-63, 10.1109/JSEN.2009.2035730.

[67] C. Liousse, J. E. Penner, C. Chuang, J. J. Walton, H. Eddleman, H. Cachier, "A global three-dimensional model study of carbonaceous aerosols", Journal of Geophysical Research: Atmospheres, Vol. 101, Is. D14, 1996, Pages 19411-19432, 10.1029/95JD03426.

[68] S. M. Kreidenweis, K. Koehler, P. J. DeMott, A. J. Prenni, C. Carrico, B. Ervens, "Water activity and activation diameters from hygroscopicity data – Part I: Theory and application to inorganic salts", Atmos. Chem. Phys., Vol. 5, 2005, Pages 1357-1370, 1680-7324/acp/2005-5-1357.

[69] S. G. Jennings, C. D. O'Dowd, W. F. Cooke, P. J. Sheridan, H. Cachier, "Volatility of elemental carbon", Geophysical Research Letters, Vol. 21, Is. 16, 1994, Pages 1719-1722, 10.1029/94GL01423.

[70] C. Perrino, E. Marconi, L. Tofful, C. Farao, S. Materazzi, S. Canepari, "Thermal stability of inorganic and organic compounds in atmospheric particulate matter", Atmospheric Environment, Vol. 54, 2012, Pages 36-43, 10.1016/j.atmosenv.2012.02.078.

[71] N. I. Kristiansen, A. Stohl, D. J. L. Olivié, B. Croft, O. A. Søvde, H. Klein, T. Christoudias, D. Kunkel, S. J. Leadbetter, Y. H. Lee, K. Zhang, K. Tsigaridis, T. Bergman, N. Evangeliou, H. Wang, P. L. Ma, R. C. Easter, P. J. Rasch, X. Liu, G. Pitari, G. Di Genova, S. Y. Zhao, Y. Balkanski, S. E. Bauer, G. S. Faluvegi, H. Kokkola, R. V. Martin, J. R. Pierce, M. Schulz, D. Shindell, H. Tost, H. Zhang, "Evaluation of observed and modelled aerosol lifetimes using radioactive tracers of opportunity and an ensemble of 19 global models", Atmospheric Chemistry and Physics, Vol. 16, Is. 5, 2016, Pages 3525-3561, 10.5194/acp-16-3525-2016.

[72] G. J. Roelofs, "Aerosol lifetime and climate change", Atmospheric Chemistry & Physics Discussions, Is. 12, 2012, Pages 16493-16514, 10.5194/acpd-12-16493-2012.

[73] Z. Li, A. L. Williams, M. J. Rood, "Influence of Soluble Surfactant Properties on the Activation of Aerosol Particles Containing Inorganic Solute", Journal of the Atmospheric Sciences, Vol. 55, Is. 10, 1998, Pages 1859-1866,

10.1175/1520-0469(1998)055<1859:IOSSPO>2.0.CO;2.

[74] V. M. Kerminen, K. Teinilä, R. Hillamo, T. Pakkanen, "Substitution of chloride in sea-salt particles by inorganic and organic anions", Journal of Aerosol Science, Vol. 29, Is. 8, 1998, Pages 929-942, doi.org/10.1016/S0021-8502(98)00002-0.

[75] B. Nozière, P. Dziedzic, A. Córdova, "Inorganic ammonium salts and carbonate salts are efficient catalysts for aldol condensation in atmospheric aerosols", Phys. Chem. Chem. Phys., The Royal Society of Chemistry, Vol. 12, Is. 15, 2010, Pages 3864-3872, 10.1039/B924443C.

[76] I. N. Tang, "Chemical and size effects of hygroscopic aerosols on light scattering coefficients", Journal of Geophysical Research: Atmospheres, Vol. 101, Is. D14, 1996, Pages 19245-19250, 10.1029/96JD03003.

[77] S. K. Satheesh, C. B. S. Dutt, J. Srinivasan, U. R. Rao, "Atmospheric warming due to dust absorption over Afro-Asian regions", Geophysical Research Letters, Vol. 34, Is. 4, 2007, 10.1029/2006GL028623.

[78] I. N. Sokolik, O. B. Toon, "Direct radiative forcing by anthropogenic airborne mineral aerosols", Nature, Vol 381, 1996, Pages 681-683.

[79] M. Schnaiter, H. Horvath, O. Möhler, K. H. Naumann, H. Saathoff, O. W. Schöck, "UV-VIS-NIR spectral optical properties of soot and soot-containing aerosols", Journal of Aerosol Science, Vol. 34, 2003, Pages 1421–1444.

[80] T. C. Bond, R .W. Bergstrom, "Light Absorption by Carbonaceous Particles: An Investigative Review", Aerosol Science and Technology, Vol. 40, Is. 1, 2006, Pages 27-67, 10.1080/02786820500421521.

[81] T. C. Bond, D. G. Streets, K. F. Yarber, S. M. Nelson, J. H. Woo, Z. Klimont, "A technology-based global inventory of black and organic carbon emissions from combustion", Journal of Geophysical Research: Atmospheres, Vol. 109, Is. D14, 2004, 10.1029/2003JD003697.

[82] F. W. Cooke, J. N. J. Wilson, "A global black carbon aerosol model", Journal of Geophysical Research, Vol. 101, Is. D14, 1996, Pages 19395-19409.

[83] D. Koch, J. Hansen, "Distant origins of Arctic black carbon: A Goddard Institute for Space Studies ModelE experiment", Journal of Geophysical Research: Atmospheres, Vol. 110, Is. D4, 2005, 10.1029/2004JD005296.

[84] J. C. Chow, J. G. Watson, L. W. A. Chen, W. P. Arnott, H. Moosmüller, K. Fung, "Equivalence of Elemental Carbon by Thermal/Optical Reflectance and Transmittance with Different Temperature Protocols", Environmental Science & Technology, Vol. 38, Is. 16, 2004, Pages 4414-4422, 10.1021/es034936u.

[85] M. O. Andreae, A. Gelencsér, "Black carbon or brown carbon? The nature of light-absorbing carbonaceous aerosols", Atmospheric Chemistry and Physics, Vol. 6, Is. 10, 2006, Pages 3131-3148, 10.5194/acp-6-3131-2006.

[86] H. Lukács, A. Gelencsér, S. Hammer, H. Puxbaum, C. Pio, M. Legrand, A. Kasper-Giebl, M. Handler, A. Limbeck, D. Simpson, S. Preunkert, "Seasonal trends and possible sources of brown carbon based on 2-year aerosol measurements at six sites in Europe", Journal of Geophysical Research, Vol. 112, 2007,

10.1029/2006JD008151.

[87] T. L. D. Alexander, A. C. Peter, J. R. Anderson, "Brown Carbon Spheres in East Asian Outflow and Their Optical Properties", Science, Vol. 321, 2008, Pages 833-835, 10.1126/science.1155296.

[88] A. Hoffer, A. Gelencsér, P. Guyon, G. Kiss, O. Schmid, G. P. Frank, P. Artaxo, M. O. Andreae, "Optical properties of humic-like substances (HULIS) in biomass-burning aerosols", Atmos. Chem. Phys., Vol. 6, 2006, Pages 3563-3570.

[89] H. Mukai, Y. Ambe, "Characterization of a humic acid-like brown substance in airborne particulate matter and tentative identification of its origin", Atmospheric Environment, Vol. 20, Is. 5, 1986, Pages 813-819, /10.1016/0004-6981(86)90265-9.

[90] D. Grosjean, "Ozone and Other Photochemical Oxidants", Chapter 3, The National Academies Press, 1977, Pages 42-125, 10.17226/19914.

[91] B. R. T. Simoneit, R. Chester, G. Eglinton, "Biogenic lipids in particulates from the lower atmosphere over the eastern Atlantic", Nature, Vol. 267, 1977, Pages 682–685.

[92] E. J. Hoffman, R. A. Duce, "Factors influencing the organic carbon content of marine aerosols: A laboratory study", Journal of Geophysical Research, Vol. 81, Is. 21, 1976, Pages 3667-3670.

[93] R. A. Duce, V. A. Mohnen, P. R. Zimmerman, D. Grosjean, W. Cautreels, R. Chatfield, R. Jaenicke, J. A. Ogren, E. D. Pellizzari, G. T. Wallace, "Organic material in the global troposphere", Reviews of Geophysics, Vol. 21, Is. 4, 1983, Pages 921-952, 10.1029/RG021i004p00921.

[94] S. Rehfeld, M. Heimann, "Three dimensional atmospheric transport simulation of the radioactive tracers 210Pb, 7Be, 10Be, and 90Sr", Journal of Geophysical Research: Atmospheres, Vol. 100, Is D12, 1995, Pages 26141-26161, 10.1029/95JD01003.

[95] A.C. Chamberlain, "Interception and retention of radioactive aerosols by vegetation", Atmospheric Environment, Vol. 4, Is. 1, 1970, Pages 57-78, 10.1016/0004-6981(70)90054-5.

[96] N. Kaneyasu, H. Ohashi, F. Suzuki, T. Okuda, F. Ikemori, "Sulfate Aerosol as a Potential Transport Medium of Radiocesium from the Fukushima Nuclear Accident", Environmental Science & Technology, Vol. 46, Is. 11, 2012, Pages 5720-5726, 10.1021/es204667h.

[97] I. A-S. Hussein, M. S.M. Mansour, "A review on polycyclic aromatic hydrocarbons: Source, environmental impact, effect on human health and remediation", Egyptian Journal of Petroleum, Vol. 25, Is. 1, 2016, Pages 107-123, 10.1016/j.ejpe.2015.03.011.

[98] S. Tanabe, H. Tanaka, R. Tatsukawa, "Polychlorobiphenyls, ΣDDT, and hexachlorocyclohexane isomers in the western North Pacific ecosystem", Archives of Environmental Contamination and Toxicology, Vol. 13, Is. 6, 1984, Pages 731-738.

[99] J. S. Stanley, K. E. Boggess, J. Onstot, T. M. Sack, J. C. Remmers, J. Breen, F. W. Kutz, J. Carra, P. Robinson, G. A. Mack, "PCDDs and PCDFs in human adipose

tissue from the EPA FY82 NHATS repository", Chemosphere, Vol. 15, Is. 9-12, 1986, Pages 1605-1612, 10.1016/0045-6535(86)90444-3.

[100] S. E. Schwartz, P. R. Buseck, "Absorbing Phenomena", Science, Is. 288, 2000, Pages 989-990.

[101] D. G. Streets, Y. Wu, M. Chin, "Two-decadal aerosol trends as a likely explanation of the global dimming/brightening transition", Geophysical Research Letters, Vol. 33, Is. 15, 2006, 10.1029/2006GL026471.

[102] I. Koren, M. J. Vanderlei, L. A. Remer, H. Afargan, "Smoke invigoration versus inhibition of clouds over the amazon", Science, Is. 321, 2008, Pages 946-949.

[103] A. S. Ackerman, O. B. Toon, D. E. Stevens, A. J. Heymsfield, V. Ramanathan, E. J. Welton, "Reduction of tropical cloudiness by soot", Science, Is. 288, 2000, Pages 1042-1047.

[104] E. K. Bigg, "Discrepancy between observation and prediction of concentrations of cloud condensation nuclei", Atmospheric Research, Vol. 20, Is. 1, 1986, Pages 81-86, 10.1016/0169-8095(86)90010-4.

[105] Q. Fu, P. Yang, W. B. Sun, "An Accurate Parameterization of the Infrared Radiative Properties of Cirrus Clouds for Climate Models", Journal of Climate, Vol. 11, Is. 9, 1998, Pages 2223-2237, 10.1175/1520-0442(1998)011<2223:AAPOTI>2.0.CO;2.

[106] H. Liao, J. H. Seinfeld, "Effect of clouds on direct aerosol radiative forcing of climate", Journal of Geophysical Research: Atmospheres, Vol. 103, Is. D4, 1998, Pages 3781-3788, 10.1029/97JD03455.

[107] S. A. Twomey, M. Piepgrass, T. L. Wolfe, "An assessment of the impact of pollution on global cloud albedo", Tellus B, Vol. 36B, Is. 5, 1984, Pages 256-366, 10.1111/j.1600-0889.1984.tb00254.x.

[108] S. Twomey, "Aerosols, clouds and radiation", Atmospheric Environment. Part A. General Topics, Vol. 25, Is. 11, 1991, Pages 2435-2442, 10.1016/0960-1686(91)90159-5.

[109] J. E. Penner, C. C. Chuang, C. Liousse, "The contribution of carbonaceous aerosols to climate change", Nucleation and Atmospheric Aerosols 1996, Pergamon, 1996, Pages 759-769, 10.1016/B978-008042030-1/50186-4.

[110] J. W. Munger, J. Collett Jr., C. D. Bruce Jr., R. H. Michael, "Carboxylic acids and carbonyl compounds in southern California clouds and fogs", Tellus B: Chemical and Physical Meteorology, Vol. 41, Is. 3, 1989, Pages 230-242, 10.3402/tellusb.v41i3.15074.

[111] H. Horvath, "Atmospheric light absorption - A review", Atmospheric Environment, Part A, General Topics, Vol. 27, Is. 3, 1993, Pages 293-317, 10.1016/0960-1686(93)90104-7.

[112] J. G. Watson, "Visibility: science and regulation", Journal of the Air & Waste Management Association, Vol. 52, Is. 6, 2002, Pages 628-713.

[113] B. R. Appel, Y. Tokiwa, J. Hsu, E. L. Kothny, E. Hahn, "Visibility as related to atmospheric aerosol constituents", Atmospheric Environment, Vol. 19, Is. 9, 1985, Pages 1525-1534, 10.1016/0004-6981(85)90290-2.

[114] S. Tiwari, S. Payra, M. Mohan, S. Verma, D. S. Bisht, "Visibility degradation during foggy period due to anthropogenic urban aerosol at Delhi, India", Atmospheric Pollution Research, Vol. 2, Is. 1, 2011, Pages 116-120, 10.5094/APR.2011.014.

[115] W.E. Wilson, J. C. Chow, C. Claiborn, W. Fusheng, J. Engelbrecht, J. G. Watson, "Monitoring of particulate matter outdoors", Chemosphere, Vol. 49, 2002, Pages 1009–1043.

[116] L. C. Kenny, R. Gussman, M. Meyer, "Development of a Sharp-Cut Cyclone for Ambient Aerosol Monitoring Applications", Aerosol Science and Technology, Vol. 32, Is. 4, 2000, Pages 338-358, 10.1080/027868200303669.

[117] G. A. Allen, J. A. Oh, P. Koutrakis, "Techniques for High-Quality Ambient Coarse Particle Mass Measurements", Journal of Air & Waste Management Association, Vol. 49, 1999, Pages 133-141.

[118] R. Hebisch, H.-H. Fricke, J.-U. Hahn, M. Lahaniatis, C.-P. Maschmeier, M. Mattenklott, Markus, "Sampling and determining aerosols and their chemical components", 2005, Pages 3-40, ISBN: 978-3527311385, 10.13140/2.1.4181.9202.

[119] H. Patashnick, E. G. Rupprecht, "Continuous PM-10 Measurements Using the Tapered Element Oscillating Microbalance", Journal of the Air & Waste Management Association, Vol. 41, Is. 8, 1991, Pages 1079-1083, 10.1080/10473289.1991.10466903.

[120] D. J. Eatough, F. Obeidi, Y. Pang, Y. Ding, N. L. Eatough, W. E. Wilson, "Integrated and real-time diffusion denuder sample for PM2.5", Atmospheric Environment, Vol. 33, Is. 17, 1999, Pages 2835-2844.

[121] D. Liang, W.-P. Shih, C.-S. Chen, C.-A. Dai, "A Miniature System for Separating Aerosol Particles and Measuring Mass Concentrations", Sensors, Vol. 10, Is. 4, 2010, Pages 3641-3654, 10.3390/s100403641.

[122] P. Babich, P.-Y. Wang, G. Allen, C. Sioutas, P. Koutrakis, "Development and Evaluation of a Continuous Ambient PM2.5 Mass Monitor", Aerosol Science and Technology, Vol. 32, Is. 4, 2000, Pages 309-324, 10.1080/027868200303641.

[123] E. S. Macias, R. B. Húsar, "Atmospheric Particulate Mass Measurement with Beta Attenuation Mass Monitor", Environmental Science & Technology, Vol. 10, Is. 9, 1976, Pages 904-907.

[124] M. R. Heal, I. J. Beverland, M. McCabe, W. Hepburn, R. M. Agius, "Intercomparison of five PM10 monitoring devices and the implications for exposure measurement in epidemiological research", Journal of Environment Monitoring, Vol.2, Is. 5, 2000.

[125] L. R. Crilley, M. Shaw, R. Pound, L. J. Kramer, R. Price, S. Young, A. C. Lewis, F. D. Pope, "Evaluation of a low-cost optical particle counter (Alphasense OPC-N2) for ambient air monitoring", Atmospheric Measurement Techniques, Vol. 11, Is. 2, 2018, Pages 709-720, 10.5194/amt-11-709-2018.

[126] R. A. Dweik, A. Amann, "Exhaled breath analysis: the new frontier in medical testing", Journal of Breath Research, Vol. 2, Is. 3, 2008, 10.1088/1752-7163/2/3/030301.

[127] T. A. Popov, "Human exhaled breath analysis", Annals of Allergy, Asthma & Immunology, Vol. 106, Is. 6, 2011, Pages 451-456, 10.1016/j.anai.2011.02.016.

[128] W. Miekisch, J. K. Schubert, G. F. E. Noeldge-Schomburg, "Diagnostic potential of breath analysis – focus on volatile organic compounds", Clinica Chimica Acta, Vol. 347, Is. 1, 2004, Pages 25-39,10.1016/j.cccn.2004.04.023.

[129] M. Phillips, J. Herrera, S. Krishnan, M. Zain, J. Greenberg, R. N. Cataneo, "Variation in volatile organic compounds in the breath of normal humans", Journal of Chromatography B: Biomedical Sciences and Applications, Vol. 729, Is. 1, 1999, Pages 75-88, 10.1016/S0378-4347(99)00127-9.

[130] M. P. Kalapos, "Possible physiological roles of acetone metabolism in humans", Medical Hypotheses, Vol. 53, Is. 3, 1999, Pages 236-242, 10.1054/mehy.1998.0752.

[131] D. J. Betteridge, "What is oxidative stress?", Metabolism, Vol. 49, Is. 2, 2000, Pages 3-8, 10.1016/S0026-0495(00)80077-3.

[132] C. M. F. Kneepkens, G. Lepage, C. C. Roytitle, "The potential of the hydrocarbon breath test as a measure of lipid peroxidation", Free Radical Biology and Medicine, Vol. 17, Is. 2, 1994, 10.1016/0891-5849(94)90110-4.

[133] A. Amann, G. Poupart, S. Telser, M. Ledochowski, A. Schmid, S. Mechtcheriakov, "Applications of breath gas analysis in medicine", International Journal of Mass Spectrometry, Vol. 239, Is. 2, 2004, Pages 227-233, 10.1016/j.ijms.2004.08.010.

[134] S. R. Baldwin, C. M. Grum, L. A. Boxer, R. H. Simon, L. H. Ketai, L. J. Devall, "Oxidant activity in expired breath of patients with adult respiratory distress syndrome"", The Lancet, Vol. 327, Is. 8471, 1986, Pages 11-14, 10.1016/S0140-6736(86)91895-7.

[135] S. Swann, "Magnetron sputtering", Physics in Technology, Vol. 19, Is. 2, 1988, Pages 67-75, 10.1088/0305-4624/19/2/304.

[136] P. J. Kelly, R. D. Arnell, "Magnetron sputtering: a review of recent developments and applications", Vacuum, Vol. 56, Is. 3, 2000, Pages 159-172, 10.1016/S0042-207X(99)00189-X.

[137] B. Window, N. Savvides, "Unbalanced dc magnetrons as sources of high ion fluxes", Journal of Vacuum Science & Technology A, Vol. 4, Is. 3, 1986, Pages 453-456, 10.1116/1.573904.

[138] N. Savvides, B. Window, "Unbalanced magnetron ion-assisted deposition and property modification of thin films", Journal of Vacuum Science & Technology A, Vol. 4, Is. 3, Pages 504-508, 1986, 10.1116/1.573869.

[139] D. G. Teer, "Technical note: A magnetron sputter ion-plating system", Surface and Coatings Technology, Vol. 39-40, 1989, Pages 565-572, 10.1016/S0257-8972(89)80017-9.

[140] W. D. Sproul, P. J. Rudnik, M. E. Graham, S. L. Rohde, "High rate reactive sputtering in an opposed cathode closed-field unbalanced magnetron sputtering system", Surface and Coatings Technology, Vol. 43-44, 1990, Pages 270-278, 10.1016/0257-8972(90)90080-V.

[141] J. O'Brien, "The production of porous and chemically reactive coatings by magnetron sputtering", PhD Thesis, University of Salford, 1998.

[142] J. A. Thornton, "Influence of apparatus geometry and deposition conditions on the structure and topography of thick sputtered coatings", Journal of Vacuum Science and Technology, Vol. 11, Is. 4, 1974, Pages 666-670, 10.1116/1.1312732.

[143] R. Messier, A. P. Giri, R. A. Roy, "Revised structure zone model for thin film physical structure", Journal of Vacuum Science & Technology A, Vol. 2, Is. 2, 1984, Pages 500-503, 10.1116/1.572604.

[144] P. J. Kelly, R. D. Arnell, "Development of a novel structure zone model relating to the closed-field unbalanced magnetron sputtering system", Journal of Vacuum Science & Technology A, Vol. 16, Is. 5, 1998, Pages 2858-2869, 10.1116/1.581432.

This Ph.D. thesis has been typeset by means of the TEX-system facilities. The typesetting engine was LuaLATEX. The document class was `toptesi`, by Claudio Beccari, with option `tipotesi =scudo`. This class is available in every up-to-date and complete TEX-system installation.